Tropical Cyclone Boundary-Layer Models

Dissertation

an der Fakultät für Physik

der Ludwig-Maximilians-Universität München

vorgelegt von

Stefanie Vogl

aus Regensburg

Mai 2009

Erstgutachter: Prof. Dr. Martin Dameris
Zweitgutachter: Prof. Dr. George Craig
Tag der Abgabe: 4. Mai 2009
Termin der mündlichen Prüfung: 24. Juni 2009

Zusammenfassung

Tropische Wirbelstürme gehören sicherlich zu den spektakulärsten Wettererscheinungen auf unserem Planeten. Die aktuelle Diskussion des Klimawandels hat solche extremen Wettererscheinungen zudem ins öffentliche Interesse gerückt.
Heutzutage werden hochkomplexe numerische Computersimulationen verwendet um zum Beispiel die Zugbahn von Wirbelstürmen vorherzusagen. Trotzdem gibt es noch viele fundamentale Fragen im Zusammenhang mit tropischen Wirbelstürmen, die unbeantwortet sind. Darunter ist die Frage, wie stark der Sturm werden kann von besonderem Interesse.
Die Grenzschicht tropischer Wirbelstürme hat auf deren Dynamik und Thermodynamik entscheidenden Einfluß. In meiner Arbeit habe ich zwei Vertreter verbreiteter Modelltypen dieser Grenzschicht entwickelt.
In Kapitel (2) habe ich ein lineares Modell der Grenzschicht hergeleitet und analytische Lösungen der Windfelder berechnet. Im Unterschied zu anderen Studien konnte ich mit Hilfe dieser Lösungen eine Bewertung der linearen Approximation durchführen. Die Ergebnisse wurden in Vogl und Smith (2009) veröffentlicht.
In Kapitel (3) habe ich ein sogenanntes Scheibenmodell untersucht. Dieses Modell ermöglicht zusätzlich eine Vorhersage von thermodynamischen Vorgängen in der Grenzschicht. Der Einfluß verschiedenster physikalischer Prozesse wurde untersucht und schließlich konnte eine umfassende Bewertung der Stärken und Schwächen des Scheibenmodells durchgeführt werden. Die Ergebnisse wurden in Smith und Vogl (2008) veröffentlicht.
Aus den Untersuchungen folgt, daß die Annahme des Gradientwind-Gleichgewichts die entscheidende Schwäche dieser beiden Grenzschichtmodelle darstellt. In Kapitel (4) zeige ich, daß genau diese Schwäche der Grenzschichtmodelle auch die Schwäche der etablierten "potential intensity" Theorie darstellt. Ich stelle schließlich ein neues, verbessertes konzeptionelles Modell des Bereiches rund um das Auge des Sturmes vor. Diese Ergebnisse wurden in Smith, Montgomery und Vogl (2008) veröffentlicht.
Insgesamt konnte ich mit meiner Arbeit einen wichtigen Beitrag zur Bewertung der Stärken und Schwächen unterschiedlicher Grenzschichtmodelle liefern und am Ende sogar einen neuen Ansatzpunkt aufzeigen, der die Entwicklung einer dringend benötigten, verbesserten Theorie für die Vorhersage der Intensität tropischer Wirbelstürme liefert.

Abstract

Hurricanes are some of the most spectacular yet deadly natural disasters. Especially in times of the widely discussed anthropogenic climate change, public interest focusses on such extreme weather events. Nowadays, highly sophisticated numerical models are used for example for track prediction, but still there are many fundamental open questions. Among these, the question how intense a tropical cyclone may become is of major interest.

In this work a study of the two most common types of models for the hurricane boundary layer is carried out. This study reveals major deficiencies of boundary layer models and finally leads to a reassessment of the established theory of potential intensity of hurricanes.

In chapter (2), a linear model for the hurricane boundary layer is derived from a detailed scale analysis of the full equations of motions. It is shown how analytic solutions for the model may be calculated and how these solutions may be used to appraise the integrity of the linear approximation. Some of the results of this chapter are published in Vogl and Smith (2009).

In chapter (3), a slab model is examined, which yields results for the main thermodynamic quantities. Depending on the chosen boundary layer depth and the imposed wind profile, two different types of solution behaviour are found and interpreted. Other aspects of the dynamics and thermodynamics of the boundary layer are studied as for example the influence of shallow convection. The limitations and strengths of the slab model are discussed at the end of chapter (3). The results are published in Smith and Vogl (2008).

The results of the detailed investigation of the linear and the slab model both point out an important deficiency of hurricane boundary layer models, namely the assumption of gradient wind balance. In chapter (4) it is shown that indeed the major deficiency of the established hurricane (P)otential (I)ntensity theory is the tacit assumption of gradient wind balance in the boundary layer. The results of chapter (4) show a fundamental problem of the established PI theory and then point to an improved conceptual model of the hurricane inner core region. Thus this work suggests a way forward to an urgently needed more consistent theory for the hurricane potential intensity. It is published in Smith, Montgomery and Vogl (2008).

Contents

Introduction

People have always been fascinated by extreme and hazardeous natural disasters and it is like that until today. Earthquakes, flooding and extreme weather demand human lifes and cause inestimable material losses. However, the damage caused annually seems to increase from year to year as for example a statistic of the Munich Re Group shows, where the losses of the last fifty years are documented.
Although there has been an aroused debate, nowadays there is a wide consensus that during the last hundred years the world experiences an anthropogenic climate change. The anthropogenic global warming has various adverse effects on the environment we are living in. The amount and the pattern of global precipitation are changing significantly and the increasing temperatures are causing a rise in the sea level. Droughts and floods and an increase in the number of extreme and severe weather events are supposed to be some of the immediate consequences of a changing climate. Among these natural disasters, tropical cyclones (which are called hurricanes in the Atlantic Ocean and typhoons in the Pacific) are together with earthquakes the most hazardous and deadly ones (Anthes 1982, Emanuel 2005b). In fact their destructiveness costs more lifes than any other nature catastrophy and, at least in the United States, hurricanes are the most expensive ones (Pielke and Landsea 1998).
Already historical records are witness of this destructiveness (e.g. Rappaport and Fernandez-Partagas 1995). One of the most devastating hurricanes was the so-called "1780-Hurricane". During the period 10 - 16 October, this storm passed over the Caribean islands of Martinique and Barbados, which were almost complete devastated. More than 22000 people died during that storm.
A recent example is hurricane "Mitch" from 1998. It destroyed the coastal region of Honduras in Central America and caused tremendous damage through extreme rainfall. 12000 people died, more than 2 million became homeless. Anyway, it is not only

Central America which is impacted repeatedly. Again and again the severe storms make landfall along the coastal regions of the United States. A prominent example is hurricane "Andrew" (1992). With an averaged wind speed of about 210 $\mathrm{km\,h^{-1}}$ and peak winds of more than 280 $\mathrm{km\,h^{-1}}$ it caused damage of more than 45 million US Dollars. One of the most spectacular landfalls happened during August 2005. Hurricane "Katrina" passed Florida and reached the Gulf of Mexico. The extreme winds with peaks of more than 340 $\mathrm{km\,h^{-1}}$ caused high waves and extraordinary strong precipitation was recorded (the strongest rainfall was measured in Lousiana with 380 mm). The storm destroyed the town of New Orleans by flooding when the protective embankments couldn't resist the water masses any longer. It lost hurricane strength just 250 km inland, leaving behind a path of destruction. The final balance was more than 81 million US Dollars loss. This means that "Katrina" was the most costly hurricane the United States ever experienced up to now.

However, tropical cyclones do not have only a negative impact. They bring urgently needed precipitation to Central America and countries such as Mexico are almost completely dependent on their water supply through that source. If it were not for these storms, severe droughts would follow, which is also a considerable economic factor.

The fact that these storms are huge rotating weather systems nowadays doesn't seem too surprising, but it was not before the early 19th century that people realized more clearly the structure of tropical cyclones. The possibilities for observations were poor and information came mostly from weather stations at the coasts, or on the islands, or from ship's navigation books. Just a small percentage of the storms were detected as there were large areas over the oceans where no information was available. It was the 20th century with its immense progress in aviation which finally stimulated and allowed deeper investigation. The structure and the life cycle of tropical cyclones were now rapidly becoming clearer. In the 1940s reconaissance flights were used systematically. The first pass through the eye of a hurricane took place in 1943 in the Gulf of Mexico and the first radar images were obtained by Wexler in 1947. These images clarified the structure of the clouds, showing the eye and the spiralling rainbands.

It was in the late 1960s when it became feasible to use satellites, which documented the global weather from space. Since then it is possible to record all storms that develop and actually estimate their intensities.

A tropical cyclone is defined as a cyclonic weather system that builds up over the tropical oceans where the sea surface has a temperature of more than 26 °C. The high sea

surface temperatures are a crucial factor as the cyclogenesis is supported by the heat transfer from the sea surface. The Saffir-Simpson scale provides an accepted framework to categorize the strength of the storms by their maximum wind speed. This maximum is determined by calculating a ten-minute average of the total wind speed at a height of 10 m, except for the United States, where a one-minute average is used. Not every rotating weather system is a tropical cyclone. If the maximum wind speed is below a threshold value of 17 ms^{-1} the system is called a *tropical depression*, if the wind speed is larger than 17 ms^{-1}, the so-called *gale force wind*, but smaller than 32 ms^{-1} it is a *tropical storm*. Only if the averaged winds exceed 33 ms^{-1} it is defined as *hurricane*. In Australia exists a different scale to classify tropical cyclones. For example the 17 ms^{-1} threshold is used to define a storm as a *tropical cyclone*, the equivalent of a hurricane there is the *severe tropical cyclone*.

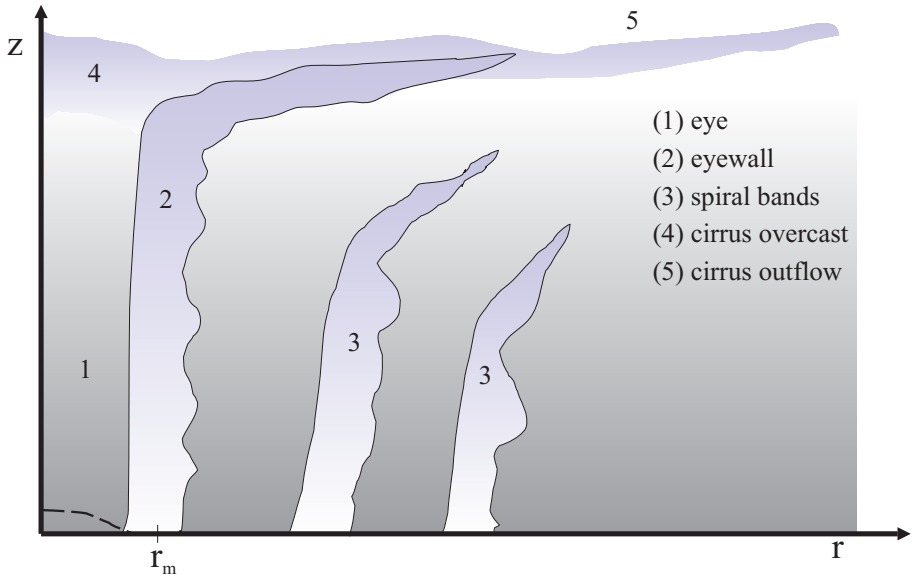

Figure 1: Idealized cloud structure of a hurricane in a cross section.

The horizontal extent of tropical cyclones, which is defined as the area where the wind speed is larger than a value of 17 ms^{-1}, is very variable. There have been reported very tight storms with a radial extent not larger than a hundred kilometers such as, for example, cyclone "Tracy" (1974). These very small storms are often referred to as *midget* storms. Tracy was the smallest storm ever recorded with gale force winds that only covered an area 48 km in radius. The variability in size may be quite large as it is examplified by "Tip" (1979). The storm was recorded in the Northwest Pacific and

reached a horizontal size with a radius of 1087 km. It may be surprising, but it seems that there is no connection between size and intensity, which is in general measured by the maximum wind speed or the central surface pressure (Emanuel 1988, Emanuel 1995b, Bister and Emanuel 1998).

Figure (1) shows the main parts of the cloud structure of a mature storm which may be idealized as an axisymmetric vortex. The most spectacular feature is the so called *eye* which is often cloud-free, has a radius of usually 10 to 60 km and where only very light winds are measured. The eye is surrounded by huge clouds which reach up to 16 km into the troposphere. The highest wind speeds in the storm are found at low levels beneath the so called *eyewall-cloud*. The whole region of the storm, except possibly the eye, is covered by dense cirrus clouds. The visualization of some of the asymmetries of the flow in the tropical cyclone are the outwards spiralling cloud bands, the so called *rainbands*. Although many models of tropical cyclones still assume rotationally symmetric storms, nowadays the asymmetries of the flow field are found to be of great importance also for cyclone dynamics as, for example, cyclone intensification (e.g. Nguyen *et al.* 2008).

Figure 2: Satellite image of Hurricane Andrew at 2020 UTC on 25th August 1992 (picture from NASA satellite/NOAA).

Figure (2) shows Hurricane Andrew at 2020 UTC on 25th August in 1992 over the

Gulf of Mexico. The image, taken from NASA satellite imagery, reveals the storm's inner structure. The Earth's surface is visible through the cloud free eye, while in the outer parts of the storm the cirrus overcast obstructs the sight onto the ground. The *spiral rainbands* are seen as white cloud tails in the satellite image. The strongest precipitation is found in these spiral rainbands and in the eye-wall. Most insights about the structure and the life-cycle of tropical cyclones are a direct result from measurements by reconaissance flights. However, high-resolution numerical model simulations are becoming more and more important. These sophisticated models use the available data to predict the track of the cyclone, of course try to answer the question how far the weather system might extend in the horizontal and how high the maximum wind speed inside the storm might be.

Track prediction and the estimation of maximum intensity are questions which are of immense public interest, especially when a storm is on the verge of landfall. To improve operational models, statistical comparison of available different model types or the question for the best way of data-assimilation, to initialize the model runs, are ongoing challenges. These very complex models, which often provide satisfactory results, could easily suggest that the physical processes in the tropical cyclone are well understood. However this is not the case. The highly complicated process of cyclogenesis, the spin-up of the storm, or for example the processes that govern the strength of the storm, are still not fully understood.

One possibility to investigate the most fundamental problems is to use highly idealized mathematical models of tropical cyclones. Those models reduce the storm to its major features and need just very few predetermined parameter specifications to obtain results for their spatial structure and their temporal development.

Figure (3) shows a highly idealized sketch of the dynamical features in a mature hurricane, when it is approximated as an axisymmetric vortex.

The flow in a mature tropical cyclone, in a simplified thought experiment, may be divided into two different circulations. First of all there is the primary circulation. It is a horizontal quasi-symmetric circulation on which is superposed a thermally-direct vertical (transverse) circulation, the secondary circulation. These terms were first used by Ooyama (1982). The combination of these two circulations results in the typical spiralling flow, which is characteristic of tropical cyclones. The question now arises where this secundary circulation is originating from, which is responsible for the characteristic observed spiral motion in the storm. If there was only the primary circulation

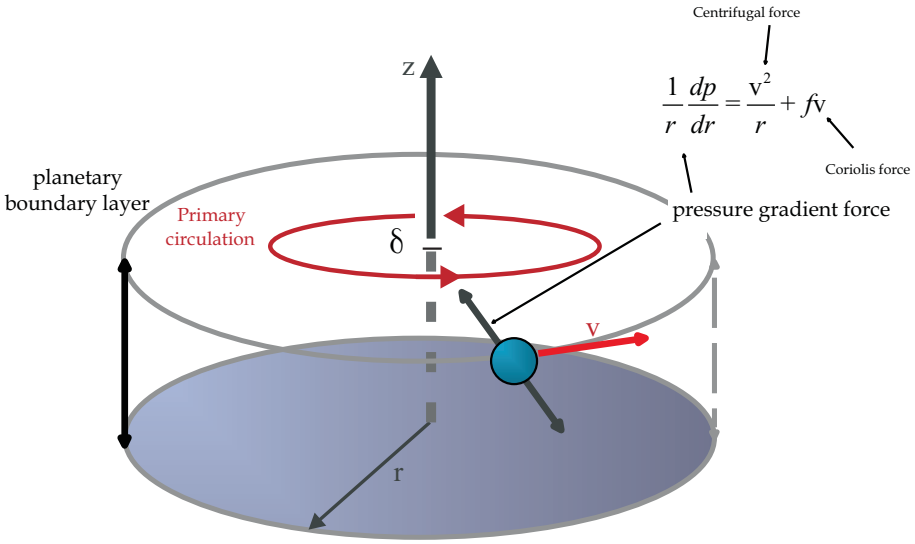

Figure 3: Schematic structure of the flow in a mature tropical cyclone in a steady state where gradient wind balance is seen.

an air parcel would just move along a circle round the axis. In the absence of friction the centrifugal force and the Coriolis force act to move the parcel outwards and balance the pressure gradient force, which is due to the pressure drop towards the storm center. This balance, which is schematically shown in Fig.(3), is also referred to as gradient wind balance.

However, there must be other physical effects which induce the secondary circulation and finally lead to the spiraling motion of air parcels. It turns out that the surface friction has a strong influence on the dynamics of the tropical cyclone. Actually this is not only true in the layer where friction acts, the so-called *boundary layer*, but also above.

One can show that the friction must reduce the tangential wind speed near the surface. Not at all obvious is the fact that the effect of friction on the pressure field in the boundary layer is just very small. A scale analysis will show (see Chapter (1.2)) that the radial pressure gradient in the boundary layer is approximately the same as that immediately above the layer so that the pressure gradient force acting on a parcel of air is almost the same through the whole depth of the layer.

The reduction of the tangential wind speed by friction leads to a reduction of the centrifugal and the Coriolis force as sketched in Fig.(4). The result is that the unchanged pressure gradient force now is larger than the sum of the two outwards pointing forces and the parcel of air is driven inwards towards the core. A strong inflow in the bound-

ary layer close to the ground at a height of about 50 to 100 m is resulting, as sketched in Figure (4). This effect is often referred to as frictionally-induced convergence. The consequences of this convergence are notable in the vertical velocity.

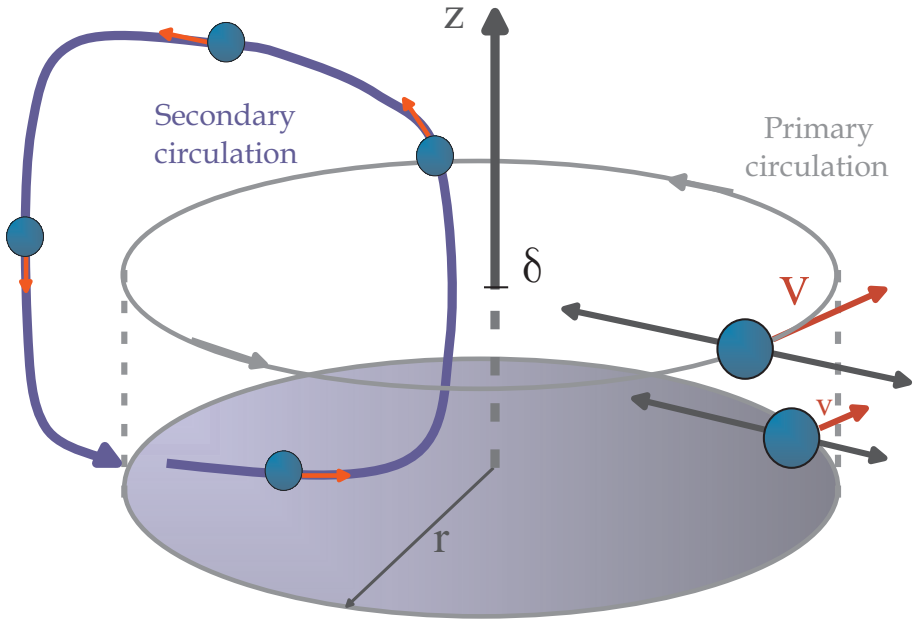

Figure 4: Schematic sketch of the frictionally-induced convergence in the tropical cyclone.

Figure (4) also highlights schematically the frictionally-induced convergence and the secondary circulation. At large distances from the hurricane core both the inflow velocity and the mass flux towards the center increase with decreasing radius. This mass flux is balanced through forced subsidence above the boundary layer at large radii. At inner radii, where the inflow and mass flux begin to become smaller, the air parcels are moved upwards from the boundary layer into the vortex above due to effects of local buoyancy. This means that the presence of the rigid boundary leads to convergence in lower levels and vertical motion in the vortex above the boundary layer, thereby inducing the secondary circulation in the vortex above. The strong upflow in the eyewall clouds transports very moist and warm air from the boundary layer up into the vortex above and the heat transfer from the sea surface is the most important energy supply of the storm. Therefore, it is the great importance of the boundary layer both for the dynamic and the thermodynamic processes why the lowest few hundreds of meters are of special interest.

Over the years the boundary layer has been the subject of numerous theoretical investigations, many of them relating to axisymmetric vortices (Rosenthal 1962, Miller 1965, Smith 1968, Leslie and Smith 1970, Carrier 1971, Eliassen 1971, Bode and Smith 1975, Eliassen and Lystadt 1977, Shapiro 1983, Montgomery et al. 2001, Smith 2003) and a few to asymmetric vortices (Shapiro 1983, Kepert 2001, Kepert and Wang 2001, Kepert 2006a, 2006b). With the exception of Smith (2003), these studies focussed exclusively on the dynamical constraints of the boundary layer. The importance of the thermodynamical constraint was recognized by Emanuel (1986) and its representation was a key feature in the simple axisymmetric model he proposed for a mature hurricane. This model was the starting point for his so-called potential intensity theory which gives an estimate for the maximum wind speed that may be obtained in a hurricane during its life-cycle.

Hurricane boundary layer models may be divided into three different types. First there are vertically-integrated models (Smith 1968, Leslie and Smith 1970, Bode and Smith 1975). For this approach, radially-varying profiles for the radial and the tangential wind need to be given, but not their scales. The so called slab models are a subset of these (Shapiro 1983, Smith 2003, Smith and Montgomery 2008). They assume vertical profiles and finally yield radial and tangential wind profiles, which are averaged through the depth of the boundary layer. The third type are the "continuous models" (Eliassen 1971, Eliassen and Lystadt 1977, Montgomery *et al.* 2001, Kepert 2001, Kepert and Wang 2001). These models enable both the radial and the vertical structure of the boundary layer flow to be determined. Although all of these models capture the general features of the hurricane boundary layer reasonably well it is clear that each type has its own strengths and also weaknesses. In this work, two types of boundary layer models are derived and compared. The first one is a symmetric "continuous model", which focusses exclusively on the dynamics of the boundary layer, while the second model, which is a slab model similiar to the one developed by Smith (2003), considers also certain thermodynamic aspects.

In one of the early studies of continuous models Eliassen (1971) developed a linear theory for the spin-down (i.e. the decrease of the intensity) of a idealized vortex due to the influence of surface friction. He used a very simplified boundary condition at the surface which supposes that both the radial and the tangential wind speed vanish at the surface, the so-called *no-slip* boundary condition. He showed that with this condition, the tangential winds above the boundary layer decrease exponentially with

time. He found also that the vertical velocity is directed upwards at the top of the layer, that it is almost constant inside the radius of maximum tangential wind and that it reaches its maximum at the center of the vortex. This result is different from what is found in turbulent boundary layers where the vertical velocity at the top of the boundary layer is zero at the vortex center and increases linearly with radius inside the radius of maximum tangential winds.

The work of Eliassen (1971) was extended by Eliassen and Lystad (1977). They incorporated differential rotation in the tangential flow and presented numerical solutions of the coupled equations for the boundary layer and the vortex above for the case with a quadratic drag law in the surface layer, the so called *slip* boundary condition. Their theory for the spindown predicts the evolution of the angular velocity, the transverse streamfunction, the boundary layer depth as well as the half-life time of the vortex (the time required to reduce the angular velocity by one half). They formulated the theory in a nonrotating coordinate system and assumed that the flow evolves close to a state of cyclostrophic balance throughout the fluid. Cyclostrophic balance means that frictional and Coriolis forces are negligible and the centripetal acceleration is exclusively balanced by the pressure gradient force.

However, they did not examine vortices of hurricane strength. The strongest vortex they examined had a maximum wind speed of only 10 m s^{-1}. This corresponds to a Rossby number of 20 at the latitude they considered. Their Rossby number was defined as $R_o = 2\omega_c/f$ where ω_c denotes the angular velocity at the vortex center and f is the Coriolis parameter. It characterizes the importance of the Coriolis acceleration for the flow. If the influence of the Coriolis force is just small, as it is required for cyclostrophic balance, the Rossby number must be sufficiently large.

Montgomery *et al.* (2001) pointed out that the neglected noncyclostrophic terms in the boundary layer may become significant at higher swirl speeds. It was argued that this might limit the applicability of the theory to hurricanes. To investigate this issue, Montgomery *et al.* (2001) carried out numerical calculations of the full nonlinear equations in the same spin-down flow configuration as Eliassen and Lystadt. They calculate solutions for weak vortices, but also for vortices of hurricane strength (i.e., with maximum tangential winds exceeding 33 m s^{-1}).

They found that the theoretically predicted algebraic temporal decay of the primary vortex is validated for tropical storm and hurricane strength vortices also. Further they noted increasing quantitative deviations from Eliassen and Lystadt's theory with

increasing fluid depth, although the theory is still qualitatively valid for hurricane-like vortices 10 and 15 km deep. They found also that, as the vortex strength increases from tropical storm to hurricane strength, the cyclostrophic balance approximation becomes only marginally valid in the boundary layer, yet remains valid in the flow interior. In addition, a temporary spinup of tangential winds and vertical vorticity in the boundary layer and a low-level outflow jet occur in the numerical simulations. These features were not predicted by the theory and it was argued that they are the primary cause for the discrepancy between the theory and the model simulations.
Kepert (2001) examined the linear equations for the steady boundary layer of an asymmetric vortex with the assumption that there is gradient wind balance at the top of the boundary layer and obtained an analytic solution to these. He showed that the solution incorporates a region of supergradient winds (that means that the tangential wind speed in the boundary layer exeeds that found at the top of the layer) near the top of the layer, just like the solution to the well known classical Ekman equations for the boundary layer flow. He showed also that just as in the Ekman solution, the degree to which the flow is supergradient is only a few percent.
In a second paper Kepert and Wang (2001) compared their linear solution with a steady state solution for the boundary layer obtained from a numerical model, which included a relatively sophisticated parameterization of the boundary layer. They showed, inter alia, that vertical advection of angular momentum plays a crucial role in strengthening the supergradient component, which may be several times stronger than predicted by the linear model. However none of these studies presented a detailed scale analysis to corroborate the linear theory. In this work the linear equations as presented by Kepert (2001), but in an axisymmetric framework, will be derived from a detailed scale analysis.

In many early hurricane models and also in many idealized models that have been used recently, the boundary layer is represented by a simple slab model. As the resulting predictions of hurricane models are sensitive to the implemented representation of the boundary layer and slab models are widely used, it is of interest to investigate their accuracy compared to linear boundary models. One disadvantage of slab boundary layer models as developed by Shapiro (1983), Smith (2003) or Smith and Montgomery (2008) is that it is not possible to determine the radial variation of the boundary layer depth. In many cases a constant boundary layer depth is assumed and the profiles are integrated over this constant depth. However, an investigation of the linear

solutions suggests that the boundary layer depth decreases towards the center and the assumption of a constant boundary layer depth is a crude simplification. It will be shown in this work that it is possible to remove this deficiency if the continous model is used to calculate a radial profile of the boundary layer depth and use this profile in the slab model.

This work will show that the assumption of gradient wind balance in the boundary layer is a major deficiency of many common theories. However, for the slab model, it is not necessary to assume that the flow which leaves the layer must be in gradient wind balance with the flow above. This fact is an advantage compared to the linear approach.

The finding that the assumption of gradient wind balance in the boundary layer is a major deficiency turns out to have important consequences.

The forecasting models for tropical cyclones do not only focus on an accurate track prediction, but are also used to estimate the energy which will be released by the storm on an eventual landfall. To find a measure for the inherent potential destructiveness and to predict a worst case scenario is, indeed, one of the most important tasks operational models have to fulfill. In 1986 Emanuel presented a steady axisymmetric model for a mature hurricane which provided the basis to develop a theory of this *potential intensity* (PI) of a tropical cyclone (Emanuel 1988, Emanuel 1995b, Bister and Emanuel 1998). The potential intensity therein is estimated by the predicted pressure fall or the predicted maximum attained wind speed.
It is very common to use the so called E(manuel)PI-theory whenever the intensity attained in numerical models is compared to theory (e.g. Frank and Ritchie 2001, Persing and Montgomery 2003). As the EPI theory predicts an increase of potential intensity with increasing sea surface temperature, the effects of global warming on the hurricane intensity have been also investigated by many researchers using this theory, as for example by Knutson and Tuleya (2004), Emanuel (2005) and Bengtson *et al.* (2007).

Despite the fact that EPI-theory provides a reasonable framework for intensity estimates, evidence suggests that this theory has some major deficiencies. Persing and Montgomery (2003), for example, have shown that high resolution numerical models may produce storms for which the intensity is significantly higher than it is predicted by the EPI-theory. It was shown also that for these so-called "superintense" storms

the intensity depended delicately on the assumed relative humidity at the radius of maximum tangential wind speed, while in EPI theory Emanuel assumed the humidity to be constant at a value of 80 %. It is not only the assumption of a constant relative humidity that is a limiting factor to the performance of EPI-theory. In the hurricane model developed by Emanuel (1986) the boundary layer is of high importance as it determines the values of absolute angular momentum per unit mass and equivalent potential temperature which are assumed to be conserved when an air parcel exits the layer. It is questionable how the representation of the boundary layer in Emanuel (1986) influences the results of EPI-theory.

As it has been pointed out in detail above, there are still a lot of fundamental open questions in the field of tropical cyclone physics. It is more and more accepted that the answers to many of those questions can not be given without considering the processes in the boundary layer of the storm. High-resolution numerical models of course are an important tool in research, but often do not provide physically substantial insights. Therefore this work focusses on two highly idealized boundary layer models. The aim of this study is to understand better the strengths and limitations of two very common representations of the boundary layer and to investigate, if there are consequences for other fields of hurricane research, such as the question of hurricane spin-up or the theory of potential intensity. In chapter (2), a linear model for the hurricane boundary layer is derived from a detailed scale analysis of the full equations of motions. It is shown how analytic solutions for the model may be calculated and how these solutions may be used to appraise the integrity of the linear approximation.
In chapter (3), a slab model is examined numerically, which additionally yields results for the main thermodynamic quantities. Different aspects of the dynamics and thermodynamics of the boundary layer are studied and the limitations and strengths of the slab model are discussed at the end of chapter (3).
Finally, chapter (4) recapitulates the main ideas of the well-established hurricane (P)otential (I)ntensity theory and investigates some of its major deficiencies in the light of the findings of chapter (2) and (3). Indeed, the results of chapter (4) show a fundamental problem of the established PI theory and point to an improved conceptual model of the hurricane inner core region.

Chapter 1

Ekman's simple boundary layer model applied to a hurricane

1.1 The planetary boundary layer

The planetary boundary layer (PBL) is defined as *"that part of the troposphere that is directly influenced by the presence of the Earth's surface, and responds to surface forcings with a timescale of about an hour or less. These forcings include frictional drag, evaporation and transpiration, heat transfer, pollutant emission, and terrain induced flow modification. The boundary layer thickness is quite variable in time and space, ranging from hundreds of meters to a few kilometers"*, (Stull 1988, pg.2).

Simply speaking, the planetary boundary layer is that part of the Earth's atmosphere that directly surrounds us and where "weather happens".

The transport processes in the PBL are mostly dominated by turbulence, a characteristic feature in contrast to the free atmosphere. The boundary layer is usually subdivided into three parts (e.g. Garratt 1992) as sketched in Fig.(1.1).

The lowest few millimeters are called the *friction layer* or *viscous sublayer* where the influence of the surface is immediate. In the viscous sublayer the vertical shears are very large and the heat and mass transfer between the surface and the air above is mainly due to molecular diffusion. This layer is often neglected although it may become important for processes which include, for example, the interaction of the atmosphere

with the sea surface.

Above the viscous sublayer lies the so called *Prandtl layer* or *inertial sublayer* which has a depth of 20 m up to about 100 m, depending on the thermal stratification. The influence of the Coriolis force is assumed to be negligible so that there is no change in the wind direction, but just an increase in the wind speed with height. The turbulent fluxes are assumed to be constant with height in this layer.

The so called *Ekman layer* covers the main part of the PBL. It is often called the *outer region*. In this context the viscous sublayer together with the Prandtl layer are referred to as the *inner region* of the PBL. In the outer region the influence of the surface is only weak, the turbulent fluxes vanish through the depth of the layer and the flow at its top is approximately laminar. The influence of the Coriolis force is no longer negligible and it causes a change in the wind direction with height - the famous Ekman-spiral.

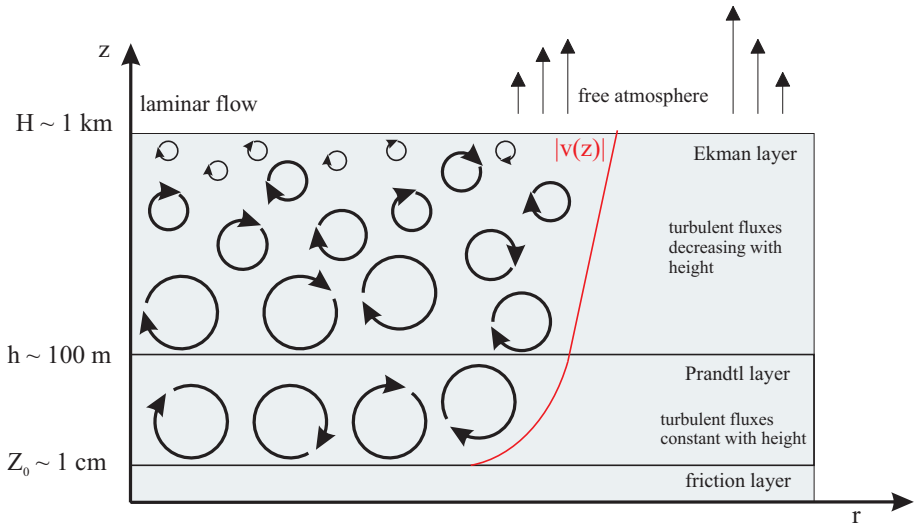

Figure 1.1: Vertical structure of the planetary boundary layer.

Especially over land the structure of the PBL is periodically changing with the so-called *diurnal cycle* (see e.g. Stull 1988). Surface heating during the daytime is followed by cooling in the nighttime. These are two completely different regimes, forming different types of turbulence. Fig.(1.2) shows the typical features of the PBL, varying during a day.

During the daytime there is strong surface heating caused by the sun. This heating results in thermal instability or convection. It is this convection that coins the name the *convective (mixed) BL*, also referred to as the *unstably stratified BL*. The stronger the

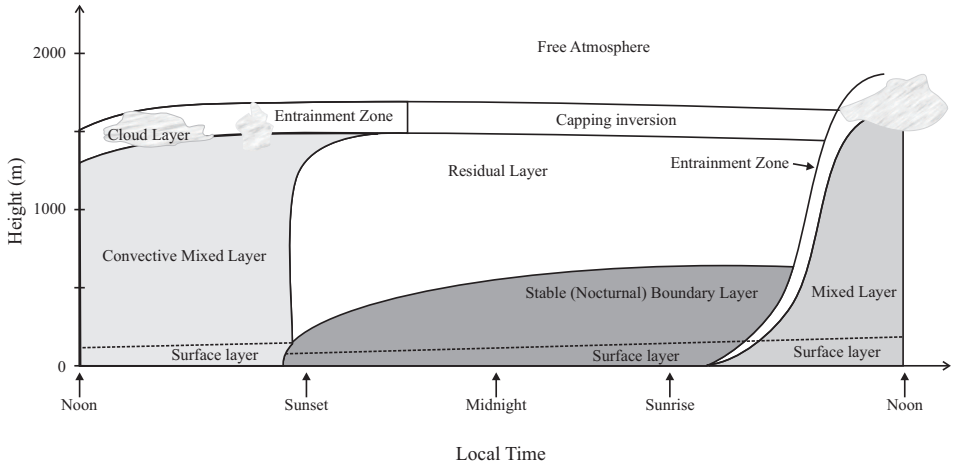

Figure 1.2: Diurnal variation of the planetary boundary layer following Stull (1988).

surface heating, the more dominant become the convective motions in the outer region which is then often called *convective mixed layer*. If there is strong convection it is easy to define the top of the boundary layer as that height in which a capping inversion is found. It is that cap that inhibits turbulent eddies to rise. At which height the stable layer occurs is very variable, but in general it is not above three kilometers. In some situations, the top of the unstably stratified BL may be defined also by a notable decrease in the aerosol concentration. In the case of very strong surface heating, such as for example over desert areas in mid summer, a boundary layer depth of 5 kilometers or even more may be observed.

During the nighttime the *stably stratified* BL is found. Surface cooling starts after sunset and a surface inversion is typical for the fully developed stable layer. It is not easy to define the top of the nighttime BL as the turbulence is much weaker. As a consequence the stable layer may just cover a few hundred meters.

Over the oceans the variability of the boundary layer within the diurnal cycle is much less than that over land. This is due to the fact that the sea surface does not heat up as fast as the land during daytime nor does it cool as fast during the nighttime. In tropical regions the structure of the PBL over the sea depends mostly on seasonal variations or special weather conditions and it's depth may be comparable to that of a PBL over land during daytime.

In any case, the boundary layer of a swirling flow with very high wind speeds such as in

the case of tropical cyclones has special characteristics as will be shown in the following section. The influence of the diurnal cycle on the hurricane boundary layer is assumed to be small and is therefore neglected in the following considerations as hurricanes are weather phenomena over the sea surface.

1.2 Ekman's simple boundary layer model

The simplest model of a planetary boundary layer under the influence of the Coriolis force is the well known model of the Ekman layer (Ekman 1905). In general the model was developed to study straight geostrophic ocean currents. Ekman assumed the flow to be *geostrophic* at the top of the boundary layer, which means that the horizontal component of the Coriolis force exactly balances the pressure gradient force.

For any system it is possible to calculate the so-called *Rossby number* which characterizes the importance of the Coriolis acceleration in proportion to the background flow:

$$R_o = \frac{V}{Rf},$$

where V and R are characteristic velocity and length scales of the flow and f is the Coriolis parameter. A small Rossby number distinguishes a system which is strongly affected by Coriolis forces from one with a large Rossby number, in which inertial and centrifugal forces dominate.
Ekman's assumption of geostrophic flow holds only if the Rossby number is sufficiently small ($R_o \ll 1$). So consequently R_o is appropriate to check the applicability of Ekman's assumption for a certain flow regime.

Taylor (1916) exerted Ekman's theory to atmospheric flow over the Earth's surface and applied a slip boundary condition at the bottom of the layer. In the slip boundary condition, the surface stress is assumed to be proportional to the absolute value of the windspeed just above the boundary.
Together with the appropriate boundary conditions, the problem of the Ekman layer is well posed and it is possible to obtain full solutions for the radial and the tangential flow inside the boundary layer. Additionally the turning of the wind vector with height and its angle to the surface may be derived.

This kind of approach is known to be relevant to a lot of problems where a boundary layer flow is found as for example in tropical cyclones. However, in the case of tropical cyclones an application of the classical Ekman theory has some limitations. First of all the theory is not posed for a circular setup.
The second problem is that, in the case of a tropical cyclone, large Rossby numbers are found. The tangential wind speed due to the rapid rotation of the storm is dominant compared to the radial component of the flow, the centrifugal force acting on an air parcel must also be taken into account. Thus the assumption that the pressure gradient force is balanced by the Coriolis force alone, is valid only in a region far from the center of the storm, where the tangential wind speed and thus the centrifugal force acting on an air parcel is small.
Even if the Ekman model was not developed for high Rossby numbers as found in tropical cyclones, it will be shown in the next section that it reproduces some characteristic features of the tropical cyclone boundary layer reasonably well. To study the Ekman equations is of interest as their simple analytic solutions allow for a substantial analysis of the influence of certain parameters such as, for example, surface drag or the representation of turbulence. In the following section it will be shown how the Ekman equations can be obtained from the general boundary layer equations by a scale analysis. Analytic solutions are derived and different boundary conditions are investigated.

1.3 The boundary layer equations

As the boundary layer of a hurricane is relatively shallow, it is a good approximation to neglect the variation of air density with height. It is assumed for the present that the turbulent momentum transfer may be represented in terms of a constant eddy diffusivity, K_M. Now the momentum equations for an axisymmetric vortex in cylindrical polar coordinates, (r, λ, z) are of the form:

$$\frac{\partial u}{\partial t} + u\frac{\partial u}{\partial r} + w\frac{\partial u}{\partial z} - \frac{v^2}{r} - fv = -\frac{1}{\rho}\frac{\partial p}{\partial r} + K_M\left(\nabla^2 u - \frac{u}{r^2}\right), \tag{1.1}$$

$$\frac{\partial v}{\partial t} + u\frac{\partial v}{\partial r} + w\frac{\partial v}{\partial z} + \frac{uv}{r} + fu = K_M\left(\nabla^2 v - \frac{v}{r^2}\right), \tag{1.2}$$

$$\frac{\partial w}{\partial t} + u\frac{\partial w}{\partial r} + w\frac{\partial w}{\partial z} = -\frac{1}{\rho}\frac{\partial p}{\partial z} + K_M \nabla^2 w, \tag{1.3}$$

where (u, v, w) is the velocity vector, p is the perturbation pressure and ρ is the density of air (see e.g. Holton 1988, Garratt 1992). The equations are completed by the continuity equation, which for a homogeneous fluid takes the form:

$$\frac{1}{r}\frac{\partial ru}{\partial r} + \frac{\partial w}{\partial z} = 0 \tag{1.4}$$

assuming that there are no density variations.

In the derivation of the equations for the boundary layer for axisymmetric flow it is normally assumed that the tangential wind component, v_{gr}, at the top of the boundary layer is a function only of radius and possibly time and that it is in gradient wind balance, i.e. it satisfies the equation:

$$\frac{v_{gr}^2}{r} + f v_{gr} = \frac{1}{\rho}\frac{\partial p}{\partial r}. \tag{1.5}$$

A scale analysis that is carried out below will show that the radial pressure gradient throughout the boundary layer may be assumed approximately equal to that at the top of the layer. Using this result it is possible to substitute for the pressure gradient in terms of v_{gr} by the use of Eq.(1.5).

1.3.1 A scale analysis

Let U, V, W be scales for u, v, w, and R, Z be length scales for r and z, respectively. Let $T = R/U$ be an advective time scale for the radial flow and Δp to be a scale for changes in the perturbation pressure, p. It is possible to define four nondimensional parameters: a *swirl parameter*, $S = U/V$; a *Rossby number* $Ro = V/fR$; a *Reynolds number*, $R_e = VZ/K_M$, which characterizes the importance of the inertial to the friction terms; and an *aspect ratio*, $A = Z/R$, which measures the ratio of the boundary-layer depth to the radial scale. As the motion is assumed to be axisymmetric, a separate advective time scale for the tangential flow, V/R, is not required.

First the continuity equation (Eq.(1.4)) is examined to derive a relation between the radial and the vertical scale. The two summands on the left-hand-side have scales

u−momentum

$$\begin{array}{ccccccccccccccc}
\frac{\partial u}{\partial t} & + & u\frac{\partial u}{\partial r} & + & w\frac{\partial u}{\partial z} & - & \frac{v^2}{r} & - & fv & = & -\frac{1}{\rho}\frac{\partial p}{\partial r} & + & K_M\left(\nabla_h^2 u - \frac{u}{r^2}\right) & + & K_M\frac{\partial^2 u}{\partial z^2} \quad (1)\\
\frac{U}{T} & & \frac{U^2}{R} & & W\frac{U}{Z} & & \frac{V^2}{R} & & fV & & \frac{\Delta p}{\rho R} & & K_M\frac{U}{R^2} & & K_M\frac{U}{Z^2} \quad (1a)\\
S^2 & & S^2 & & S^2 & & 1 & & \frac{1}{Ro} & & \frac{\Delta p}{\rho V^2} & & \frac{1}{R_e}SA & & \frac{1}{R_e}SA^{-1} \quad (1b)
\end{array}$$

v−momentum

$$\begin{array}{ccccccccccccccc}
\frac{\partial v}{\partial t} & + & u\frac{\partial v}{\partial r} & + & w\frac{\partial v}{\partial z} & + & \frac{uv}{r} & + & fu & = & & + & K_M\left(\nabla_h^2 v - \frac{v}{r^2}\right) & + & K_M\frac{\partial^2 v}{\partial z^2} \quad (2)\\
\frac{V}{T} & & U\frac{V}{R} & & W\frac{V}{Z} & & U\frac{V}{R} & & fU & & & & K_M\frac{V}{R^2} & & K_M\frac{V}{Z^2} \quad (2a)\\
S & & S & & S & & S & & \frac{S}{Ro} & & & & \frac{1}{R_e}A & & \frac{1}{R_e}A^{-1} \quad (2b)
\end{array}$$

w−momentum

$$\begin{array}{ccccccccccccc}
\frac{\partial w}{\partial t} & + & u\frac{\partial w}{\partial r} & + & w\frac{\partial w}{\partial z} & = & -\frac{1}{\rho}\frac{\partial p}{\partial z} & + & K_M\nabla_h^2 w & + & K_M\frac{\partial^2 w}{\partial z^2} \quad (3)\\
\frac{W}{T} & & \frac{UW}{R} & & \frac{W^2}{Z} & & \frac{\Delta p}{\rho Z} & & K_M\frac{W}{R^2} & & K_M\frac{W}{Z^2} \quad (3a)\\
S^2A^2 & & S^2A^2 & & S^2A^2 & & \frac{\Delta p}{\rho V^2} & & \frac{SA^3}{R_e} & & \frac{SA}{R_e} \quad (3b)
\end{array}$$

Table 1.1: Scaling of the terms in Eqs.(1.1),(1.2) and (1.3). The ratios in the first lines under each equation show the scale of the equation term above it while the second line shows the corresponding nondimensional scales. Here $A = Z/R$, $S = U/V$, $Ro = V/fR$, and $R_e = VZ/K$.

U/R and W/Z and since these sum to zero, they must have the same magnitude, i.e. $W/Z \sim U/R$. This result is used to simplify the scale analysis of the momentum equations shown in Table (1.1).

The ratios in the first lines under each equation show the scale of the equation term above it while the second line shows the corresponding nondimensional scales. These are obtained by dividing line (1a) and (2a) by V^2/R to obtain (1b) and (2b), and dividing line (3a) by V^2/Z to obtain (3b).

As the boundary layer is typically thin, which means that it has not more than 500 m to 1 km in depth, Z is small compared to the radial scale R, say $R = 50$ km and $Z = 500$ m. Hence for the aspect ratio A follows that $A = Z/R = 10^{-2}$, which is small compared with unity. A typical value for the eddy diffusivity K_M is of the order of 10 $\mathrm{m^2 s^{-1}}$ (e.g. Rosenthal 1962) and if the core region of the storm is to be taken into account it is realistic to assume $V = 50\ \mathrm{m\,s^{-1}}$. These estimates may be used to

calculate the Reynolds number: $R_e = \frac{VZ}{K_M} = \frac{50 \cdot 500}{10} = 2.5 \times 10^3$. It follows from line (3b) in Table (1.1) that

$$\Delta p/(\rho V^2) \approx 3S^2A^2 - \frac{SA}{R_e}(A^2+1).$$

As $A^2 = 10^{-4}$ it follows $(A^2+1) \approx 1$ and therefore

$$\Delta p/(\rho V^2) \approx \max(3S^2A^2, SAR_e^{-1}) = 3 \times 10^{-4} \tag{1.6}$$

if one assumes that $S \approx 1$ in the boundary layer, which means that the radial and the tangential wind speeds are of the same order of magnitude. Analyzing Eq.(1.6) it follows that the vertical variation of p across the boundary layer is only a tiny fraction of the radial variation of p above the boundary-layer. In other words, to a close approximation, the radial pressure gradient within the boundary-layer is the same as that above the boundary-layer. This result justifies the substitution for the pressure gradient in terms of v_{gr}, using the gradient wind equation Eq.(1.5). Under the additional assumption of a steady flow ($\frac{\partial}{\partial t} \equiv 0$) the boundary layer equations then take the form:

$$u\frac{\partial u}{\partial r} + w\frac{\partial u}{\partial z} + \frac{v_{gr}^2 - v^2}{r} + f(v_{gr} - v) \;=\; K_M \frac{\partial^2 u}{\partial z^2}, \tag{1.7}$$

$$u\frac{\partial v}{\partial r} + w\frac{\partial v}{\partial z} + \frac{uv}{r} + fu \;=\; K_M \frac{\partial^2 v}{\partial z^2}, \tag{1.8}$$

where $v_{gr}(r)$ is the gradient wind speed at the top of the boundary layer and we denote $v_{gr}(r_g) = v_g$ for the geostrophic radius r_g. Note that for some calculations a radial profile for $v_{gr}(r)$, the flow at the top of the boundary layer must be specified.

To derive now the well known Ekman equations from Eqs.(1.7) and (1.8), a non-dimensional form of the equations is useful.

First the scales for the quantities have to be specified. The eddy diffusivity K_M may be written as $K_M = K_M^* k$. Here K_M^* is a constant value which is appropriate to the Ekman region, i.e. far out from the core of the storm. As a first approximation K_M is assumed to be constant (k = const.) even if it would be more realistic to let the parameter vary with height and radius and hence choose $k = k(z, r)$.

The Ekman length scale is $Z_g = \sqrt{\frac{K_M^*}{f}}$ and with the velocity scale V_g, which again represents the azimuthal geostrophic flow at the top of the boundary layer at large radii, one can define

$$v = V_g V,\ u = V_g U,\ v_{gr} = V_g V_{gr},\ z = Z_g Z \quad \text{and} \quad r = R_g R.$$

The vertical velocity w can be scaled as $w = \frac{V_g Z_g}{R_g} W$ using the continuity equation, Eq.(1.4).

Note that again the capital letters now denote dimensionless values of the scaled variables. A non-dimensional form of the momentum equations may be derived easily. This form reveals the terms that scale with the Rossby number R_o.

Using $K_M^* = Z_g^2 f$, Eqs.(1.7) and (1.8) in terms of $R_o = \frac{V_g}{R_g f}$, the local Rossby number for the flow above the Ekman region, may be simplified to:

$$R_o \left(U\frac{\partial U}{\partial R} + W\frac{\partial U}{\partial Z} + \frac{V_{gr}^2 - V^2}{R} \right) + (V_{gr} - V) = k\frac{\partial^2 U}{\partial Z^2}. \tag{1.9}$$

$$R_o \left(U\frac{\partial V}{\partial R} + W\frac{\partial V}{\partial Z} + \frac{UV}{R} \right) + U = k\frac{\partial^2 V}{\partial Z^2}. \tag{1.10}$$

These non-dimensional equations will now be the basis for deriving the well known Ekman equations for a swirling flow in the boundary layer.

At regions distant from the center of the hurricane, the flow may be assumed to be geostrophic. In terms of the local Rossby number R_o this means that $R_o \ll 1$ as this assumption requires a very small V_{gr}. Of course for the case of the flow in a hurricane this is a very crude assumption which is not valid for regions closer to the core where there is no gradient wind balance and large Rossby numbers are obtained.

Figure (1.3) shows the local Rossby number $R_o = v_{gr}/(rf)$ evaluated for the profile of $v_{gr}(r)$ (vortex 3), which is realistic for a tropical cyclone. The profile is shown in Fig.(4.12) in the Appendix, where different realistic vortex profiles and their properties are discussed in detail.

The red horizontal line is drawn at the value 1. Clearly $R_o > 1$ for radii smaller than 307 km and the assumption $R_o \ll 1$ is only valid for radii far from the storm center. However, the calculation with the most simple case, the Ekman equations, gives a first idea of the flow fields for a vortex of hurricane strength.

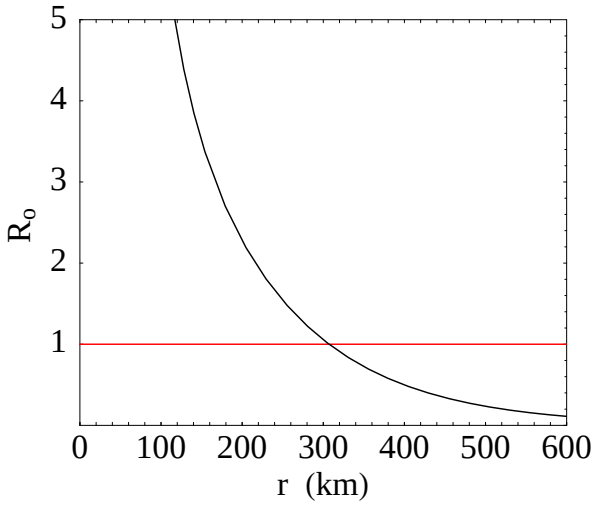

Figure 1.3: Local Rossby number R_o for vortex 3 where the red line marks unity.

The interpretation of equations (1.9) and (1.10) under the assumption of a small Rossby number, $R_o \ll 1$, shows that the inertial terms (first terms on the left hand sides of Eqs.(1.9) and (1.10)) are small compared to the terms representing Coriolis effects and the effects of friction. Hence the inertial terms may be neglected, so that finally the Ekman equations follow in their non dimensional form

$$(V_{gr} - V) = k\frac{\partial^2 U}{\partial Z^2}, \tag{1.11}$$

$$U = k\frac{\partial^2 V}{\partial Z^2}. \tag{1.12}$$

In their dimensional form the Ekman equations are:

$$f(v_{gr} - v) = K_M\frac{\partial^2 u}{\partial z^2}, \tag{1.13}$$

$$fu = K_M\frac{\partial^2 v}{\partial z^2}, \tag{1.14}$$

where v_{gr} denotes the horizontal component of the tangential wind speed at the top of the boundary layer. Note that $v_{gr}(r)$ is a function of the radius and it is assumed that $v \to v_{gr}, u \to 0$ for $z \to \infty$. These equations may easily be solved analytically.

Now solutions to the Ekman equations are derived using different boundary conditions at the lower bound. It is comfortable to complexify the system:

Let $x := v + iu$, then the Ekman equations reduce to the complex equation

$$\frac{\partial^2 x}{\partial z^2} + i\frac{f}{K_M}x = \frac{if}{K_M}v_{gr}. \tag{1.15}$$

Using a standard exponential ansatz, solutions for x are found to be of the form

$$x = v_{gr}(1 - Ae^{-(1-i)\frac{z}{\delta}}),$$

where A is a complex integration constant and $\delta := \sqrt{\frac{2K_M}{f}}$ can be interpreted as a boundary layer depth scale. The constant A is depending on the boundary condition at the surface ($z = 0$). Two different boundary conditions will be explored in the following section.

1.3.2 The no-slip boundary condition

Physically it is required that on the surface friction is acting against the flow. One possible assumption, actually the most simple one, is to assume that this makes the flow fields vanish completely at the ground ($z = 0$). This is called the *no-slip boundary condition*:

$$v(z) \to 0, \quad u(z) \to 0 \quad \text{for} \quad z \to 0.$$

With

$$u(r,z) = \mathrm{Im}(x(z)) = -v_{gr}(r)Ae^{-\frac{z}{\delta}}\sin\left(\frac{z}{\delta}\right) \quad \text{and} \tag{1.16}$$

$$v(r,z) = \mathrm{Re}(x(z)) = v_{gr}(r)\left(1 - Ae^{-\frac{z}{\delta}}\cos\left(\frac{z}{\delta}\right)\right) \tag{1.17}$$

follows for the integration constant A that $A = 1$ and

$$x = v_{gr}(1 - e^{-(1-i)\frac{z}{\delta}})$$

is a complete solution for the no-slip case. This kind of solutions were first discussed by Ekman (1905), who formulated and solved the problem for laminar ocean currents. To calculate the complete dynamical fields in Fig.(1.4), the wind profile vortex 3 shown

in Fig (4.12) in the Appendix is used. It is also necessary to specify the Coriolis parameter f and the Eddy diffusivity K_M. Here $f = 5 \times 10^{-5}$ s^{-1} and $K_M = 10$ m^{2}s^{-1} are chosen which are realistic values for that parameters (e.g. Rosenthal 1962). Panel (a) of Fig.(1.4) shows the tangential wind deficit $v'(r, z) = v(r, z) - v_{gr}(r)$.

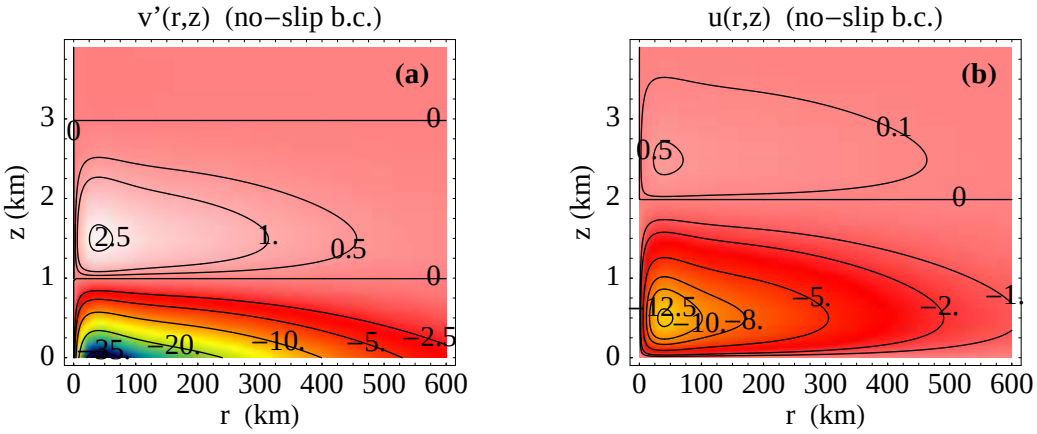

Figure 1.4: Tangential wind deficit $v'(r, z) = v(r, z) - v_{gr}(r)$ (panel (a)) and radial wind speed $u(r, z)$ (panel (b)).

Near the ground the tangential wind speed vanishes according to the no-slip boundary condition. In terms of the tangential wind deficit this means, that the difference to the given wind profile near the ground close to the radius of maximum wind speed r_m must be the maximum value of v_{gr} which is $v_m = 40$ m s^{-1}. As $v'(r, z) = -v_{gr}(r)e^{-\frac{z}{\delta}} \cos(z/\delta)$, the wind deficit is zero for

$$\frac{z}{\delta} = (2k + 1)\frac{\pi}{2}.$$

For $k = 1$ and $k = 2$ this condition is satisfied for $z_1 = 993.5$ m and for $z_2 = 2980.4$ m, respectively. The result is visualized by the zero contourlines in Fig (1.4), panel (a). If $v' > 0$ the tangential wind speed in the boundary layer is larger than that above. The fact that v' changes sign inside the boundary layer highlights the fact that there are two completely different flow regimes. In heights between z_1 and z_2 the tangential wind is *supergradient* (that is $v'(r, z) \geq 0$) below it is *subgradient*.
Fig.(1.4), panel (b) shows the radial wind field $u(r, z)$. With $A = 1$ it is $u(r, z) = -v_{gr}(r)e^{-\frac{z}{\delta}} \sin(z/\delta)$ and it follows, that $u(r, z)$ is zero for

$$\frac{z}{\delta} = k\pi.$$

For $k = 1$ and $k = 2$ this condition is satisfied for $z_1 = 1986.92$ m and for $z_2 = 3973.84$

m, respectively. This means that a layers of weak inflow ($u(r,z) \geq 0$) is capped by a layer ($z > z_1$) where weak outflow is obtained.

To determine the extreme values of the radial and tangential wind speeds $u(r,z)$ and $v'(r,z)$ the gradients of u and v' are calculated:

$$\operatorname{grad}(u(r,z)) = \begin{pmatrix} -\frac{\partial}{\partial r} v_{gr}(r) e^{-\frac{z}{\delta}} \sin\left(\frac{z}{\delta}\right) \\ -v_{gr}(r) \left(\left(-\frac{1}{\delta}\right) e^{-\frac{z}{\delta}} \sin\left(\frac{z}{\delta}\right) + \left(\frac{1}{\delta}\right) e^{-\frac{z}{\delta}} \cos\left(\frac{z}{\delta}\right) \right) \end{pmatrix} \tag{1.18}$$

and

$$\operatorname{grad}(v'(r,z)) = \begin{pmatrix} -\frac{\partial}{\partial r} v_{gr}(r) e^{-\frac{z}{\delta}} \cos\left(\frac{z}{\delta}\right) \\ -v_{gr}(r) \left(\left(-\frac{1}{\delta}\right) e^{-\frac{z}{\delta}} \cos\left(\frac{z}{\delta}\right) - \left(\frac{1}{\delta}\right) e^{-\frac{z}{\delta}} \sin\left(\frac{z}{\delta}\right) \right) \end{pmatrix}. \tag{1.19}$$

As v_{gr} has its maximum at $r_m = 40$ km, $\frac{\partial v_{gr}(r)}{\partial r} = 0$ at this radius and the corresponding z-values for the extrema of $u(r,z)$ and $v'(r,z)$ have to satisfy the conditions

$$-v_{gr}(r_m) \left(-\frac{1}{\delta}\right) e^{-\frac{z}{\delta}} \left(\sin\left(\frac{z}{\delta}\right) - \cos\left(\frac{z}{\delta}\right) \right) = 0, \tag{1.20}$$

$$-v_{gr}(r_m) \left(-\frac{1}{\delta}\right) e^{-\frac{z}{\delta}} \left(\sin\left(\frac{z}{\delta}\right) + \cos\left(\frac{z}{\delta}\right) \right) = 0. \tag{1.21}$$

As $-v_{gr}(r_m) \left(-\frac{1}{\delta}\right) e^{-\frac{z}{\delta}} \neq 0$ it follows that for $u(r,z)$ and $v'(r,z)$ the z-coordinates of the extreme points z_e are given by the equations

$$\arctan(1)\delta = z_e \quad (\text{for} \quad u(r,z)), \tag{1.22}$$

$$\arctan(-1)\delta = z_e \quad (\text{for} \quad v'(r,z)). \tag{1.23}$$

Thus the radial and tangential wind have their extreme values at the points

$$\begin{aligned} u_e(r,m) &= \left(r_m, \tfrac{(4k+1)\pi}{4}\delta\right) \\ v'_e(r,m) &= \left(r_m, \tfrac{(4k-1)\pi}{4}\delta\right) \end{aligned} \quad \text{for } k = 0, 1, 2, \ldots \tag{1.24}$$

According to the calculated extrema, the local and global maximum supergradient value $v'_e(r,z) = 2.68\ \mathrm{m\,s^{-1}}$ is obtained for $k = 1$ at r_m in a height of $z = 1.49$ km. So the tendency of supergradient wind is weaker in regions far out from the radius of maximum winds and in the inner core for $r < r_m$.
$u(r,z)$ has its local and global minimum value of u_e =- 12.9 $\mathrm{m\,s^{-1}}$ for $k = 0$ at r_m in a

height of $z = 0.5$ km. A local maximum of 0.56 m s^{-1} is found for $k = 1$ in the layer of weak outflow obtained at the radius of maximum winds r_m in a height of $z = 2.48$ km.

Another way to illustrate the results is to plot the radial and tangential flow as functions of z. Figure (1.5) shows the resulting *hodograph*, a modification of the famous Ekman spiral, for four different radii, assuming a no-slip boundary condition.

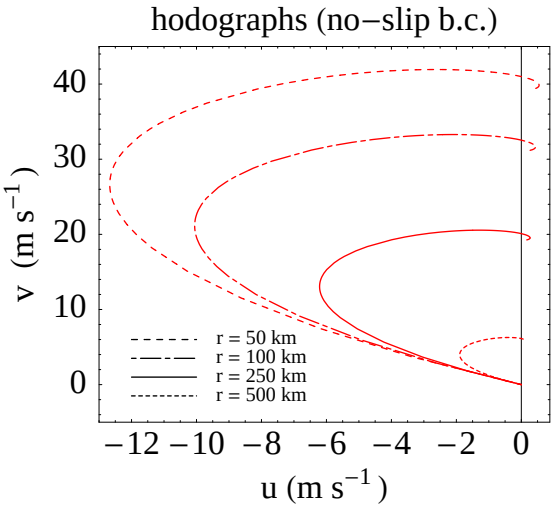

Figure 1.5: Hodographs of the radial and tangential wind speed for four different radii.

Figure (1.5) shows that the vector of the total wind is recurving with height until it reaches the value $v_{gr}(r)$. It is possible to calculate the angle α between the absolute wind vector and the vector v_{gr} at the ground. It is

$$\tan(\alpha) = \lim_{z \to 0} \frac{v(0,z)}{u(0,z)} = 1$$

by the use of L'Hospitals rule. Hence $\alpha = \pi/4$ for all radii. In general, the observed angle between the wind vector at the ground and the vector of the geostrophic wind is much smaller. Values between 12 and 25 degrees are typical. One reason for the deviation is the crude assumption of an eddy diffusivity K_M which is constant with height.

In addition to the radial and tangential flow fields it is of interest to investigate the vertical motion. In the case of the Ekman equations the vertical velocity w is obtained by integrating the continuity equation, Eq.(1.4). Using the solution obtained for $u(r,z)$

$$u(r,z) = -v_{gr}(r) e^{-\frac{z}{\delta}} \sin(z/\delta)$$

it is

$$\frac{\partial}{\partial r}(ru) = \frac{1}{r}e^{-\frac{z}{\delta}}\left(v_{gr}(r) + r\frac{\partial}{\partial r}(v_{gr}(r))\right) := f(r,z)$$

and the final result is an analytic solution for $w(r,z)$:

$$w(r,z) = -\frac{1}{r}\int_0^z f(r,z')dz'$$

$$= -\frac{\delta}{2r}e^{-\frac{z}{\delta}}\left(-e^{\frac{z}{\delta}} + \cos(z/\delta) + \sin(z/\delta)\right)\left(v_{gr}(r) + r\frac{\partial}{\partial r}v_{gr}(r)\right). \qquad (1.25)$$

Figure (1.6) shows a contour plot of the vertical velocity $w(r,z)$, calculated with vortex 3, in which can be seen that the domain is clearly divided into two regions.

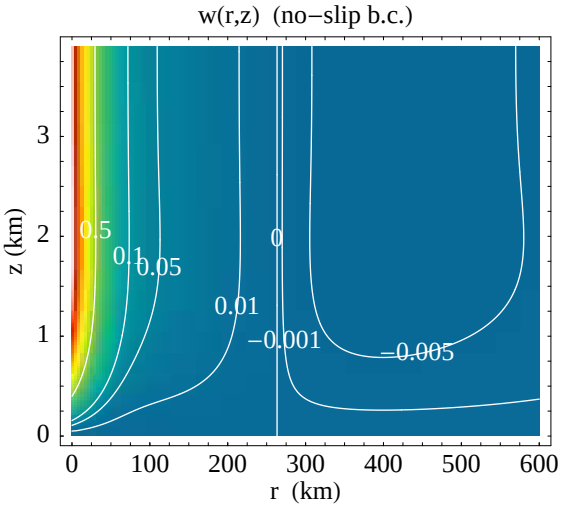

Figure 1.6: Vertical velocity $w(r,z)$ in $\mathrm{m\,s^{-1}}$ for the no-slip boundary condition.

First a region far out from the center of the vortex at radii larger than 263 km where $w(r,z)$ is negative and air parcels are transported downwards into the boundary layer. However the absolute values of $w(r,z)$ are small here. Closer to the center $w(r,z)$ is becoming positiv. This upflow is strongest in the core region of the vortex with values larger than $1\ \mathrm{m\,s^{-1}}$. As the boundary condition forces the radial wind to zero at $z = 0$, the vertical velocity is also vanishing at the ground. For heights between $0 < z < 1.5$ km, $w(r,z)$ is slightly changing until it asymptotically attains values constant in height. The radial distribution of the vertical velocity at large heights, $w_\infty(r)$, may be derived by calculating the limit $\lim_{z\to\infty} w(r,z)$. It is

$$w_\infty(r) = \frac{\delta}{2r}(v_{gr} + rv'_{gr}). \qquad (1.26)$$

This shows that $w_\infty(r)$ is only depending on the chosen profile $v_{gr}(r)$. An inspection of the zero contour in Fig.(1.6) shows that, for all heights, the vertical wind speed changes sign at the same radius, $r_{w=0}$. This fact is explained by the following analysis. In the analytic expression for $w(r,z)$ the first factor is always non-zero for all r. Thus the zero contour of the vertical velocity $w(r,z)$ is a vertical line at a radius which is determined by the condition

$$-\frac{1}{r}v_{gr}(r) = \frac{\partial}{\partial r}v_{gr}(r). \tag{1.27}$$

Note that this radius (where the vertical flow changes direction) is also only depending on the choice of the wind profile $v_{gr}(r)$. As the general character of the vertical flow is described by $r_{w=0}$ this is an important aspect.

1.3.3 The slip boundary condition

Usually a no-slip boundary condition ($u \to 0, v \to 0$ for $z \to 0$) as described before is used to close the problem at the surface although it is not very realistic. A slip boundary condition where the surface stress is parametrized by a constant drag coefficient C_D reflects the physical processes at the lower bound much better (see e.g. Holton 2004 or Garratt 1992). The boundary condition may be expressed as:

$$K\frac{\partial x}{\partial z}\bigg|_{z=0} = C_D x|x||_{z=0} \quad \text{with} \quad x = u + iv.$$

As the solutions for the Ekman equations x are of the form $x = v_{gr}(1 - Ae^{-(1-i)\frac{z}{\delta}})$, the boundary condition becomes

$$\frac{(1-i)K}{\delta v_{gr}}A = C_D|1-A|(1-A).$$

If $R_e = \frac{v_{gr}\delta}{K_M}$ and $\nu = R_e C_D$, the equation $(1-i)A = \nu|1-A|(1-A)$ has to be solved for A. It is of advantage to substitute $1 - A = Be^{i\beta}$ with the real numbers B and β. Note that B, as the absolute value of the complex number $(1-A)$, must be positive. With this substitution the boundary condition is

$$(1-i)(1-Be^{i\beta}) = \nu B^2 e^{i\beta}.$$

Separating in real and imaginary parts, a system of two equations for the real numbers B and β has to be solved:

$$\begin{aligned} (1+\nu B)\cos(\beta) + \quad & \sin(\beta) & &= \tfrac{1}{B}, \\ \cos(\beta) - \quad & (1+\nu B)\sin(\beta) & &= \tfrac{1}{B}. \end{aligned}$$

This leeds to two expressions for $\sin(\beta)$ and $\cos(\beta)$ of the form

$$\sin(\beta) = \frac{-\nu B}{B(1+(1+\nu B)^2)}, \tag{1.28}$$

$$\cos(\beta) = \frac{2+\nu B}{B(1+(1+\nu B)^2)}, \tag{1.29}$$

and with the identity $\sin^2(\beta) + \cos^2(\beta) = 1$ an algebraic equation for B is obtained

$$\nu^2 B^2 + (2+\nu B)^2 - B^2(1+(1+\nu B)^2)^2 = 0. \tag{1.30}$$

This equation can be solved analytically and with

$$w_1(\nu) := (2 + 9\nu^2 + 3\sqrt{3}\sqrt{4\nu^2 - 13\nu^4 + 32\nu^6})^{\frac{1}{3}}$$

and

$$w_2(\nu) := -1 + \frac{22^{\frac{1}{3}}(1-6\nu^2)}{w_1(\nu)} + 2^{\frac{2}{3}} w_1(\nu)$$

the real and positive B can be written as

$$B = -\frac{1}{2\nu} + \frac{1}{2\sqrt{3}\nu}\sqrt{w_2(\nu)} + \frac{1}{2\sqrt{3}\nu}\sqrt{-w_2(\nu) - 3 + \frac{2\sqrt{3}}{\nu^2\sqrt{w_2(\nu)}}}.$$

The complex integration constant A now takes the simple form

$$A(r) = a_1(r) + i a_2(r) = \frac{B\nu}{(1-i) + B\nu},$$

and the real and the imaginary part of x give the solutions for v and u:

$$v(r,z) = v_{gr}\left(1 - e^{-\frac{z}{\delta}}\left(a_1\cos\left(\frac{z}{\delta}\right) - a_2\sin\left(\frac{z}{\delta}\right)\right)\right), \tag{1.31}$$

$$u(r,z) = -v_{gr}e^{-\frac{z}{\delta}}\left(a_1\sin\left(\frac{z}{\delta}\right) + a_2\cos\left(\frac{z}{\delta}\right)\right). \tag{1.32}$$

As before in the calculation for the no-slip boundary condition the values for f and K_M are chosen as $K_M = 10\ \mathrm{m^2 s^{-1}}$ and $f = 5\times10^{-5}\ \mathrm{s^{-1}}$. Additionally it is necessary to specify the drag coefficient C_D. For simplicity it is assumed that the parameter C_D is constant. Following the literature, a realistic value is $C_D = 2\times10^{-3}$ (see e.g. Rosenthal 1962, Powell *et al.* 2003, Black *et al.* 2006). The tangential wind speed at the top of the layer is again given by vortex profile 3. Figure (1.7) shows the distribution of the tangential wind deficit $v'(r,z)$ (panel (a)) and the obtained radial wind speed $u(r,z)$ (panel (b)).

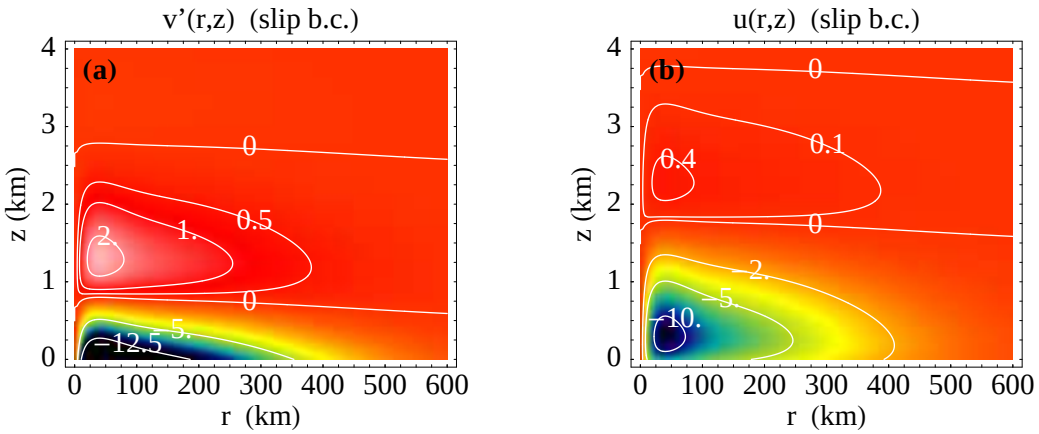

Figure 1.7: Tangential wind deficit $v'(r,z)$ (panel (a)) and radial wind speed $u(r,z)$ (panel (b)).

Again the zero contourlines of the radial wind speed $u(r,z)$ and the tangential wind deficit $v'(r,z)$ may be calculated analytically. As the integration constant is never zero it is $a_1, a_2 \neq 0$ and it follows

$$v'(r,z) = 0 \quad \Leftrightarrow \quad a_1 \cos(z/\delta) = a_2 \sin(z/\delta), \tag{1.33}$$

$$u(r,z) = 0 \quad \Leftrightarrow \quad a_1 \sin(z/\delta) = -a_2 \cos(z/\delta). \tag{1.34}$$

Therefore it is

$$z_0(r) \quad = \quad \delta(\arctan(a_1(r)/a_2(r)) - k\pi) \quad (\text{for} \quad v'(r,z)), \tag{1.35}$$

$$z_0(r) \quad = \quad \delta(\arctan(-a_2(r)/a_1(r)) - k\pi) \quad (\text{for} \quad u(r,z)) \tag{1.36}$$

for $k = 0, 1, 2, \ldots$. Note that the zero contours are now functions of the radius r. An investigation of the gradients of $v'(r,z)$ and $u(r,z)$ shows that the extreme values of both functions are always obtained at the radius of maximum winds r_m where the gradient of the function $v_{gr}(r)$ is zero. For $k = 0$ the zero contourline for $v'(r,z)$ is varying between 600 m for $r = 600$ km and the maximum of 800 m at $r = 40$ km from where it is again dropping down. Below this height the wind deficit is negative with a maximum value of about $-25\ \mathrm{m\,s^{-1}}$ near the ground at r_m.

Above the zero contour $v'(r,z)$ turns positive and hence supergradient winds are obtained. The maximum supergradient value of $2.4\ \mathrm{m\,s^{-1}}$ is obtained at r_m at a height of 1296 m.

For the radial wind speed two zero contourlines are lying in the plotted domain. One for $k = -1$ where the heights are varying between 1600 m at a radius of $r = 600$ km

and 1800 m at r_m and a second one for $k = -2$ which is lying above. For the second one the heights are varying between 3570 m at $r = 600$ km and 3800 m at r_m. In the lowest layer $u(r, z)$ is negative with a minimum value of $-11.4\ \mathrm{m\,s^{-1}}$ which is obtained at a height of 303 m. Above there is outflow which has a maximum value of $0.5\ \mathrm{m\,s^{-1}}$ at a height of 2290 m.

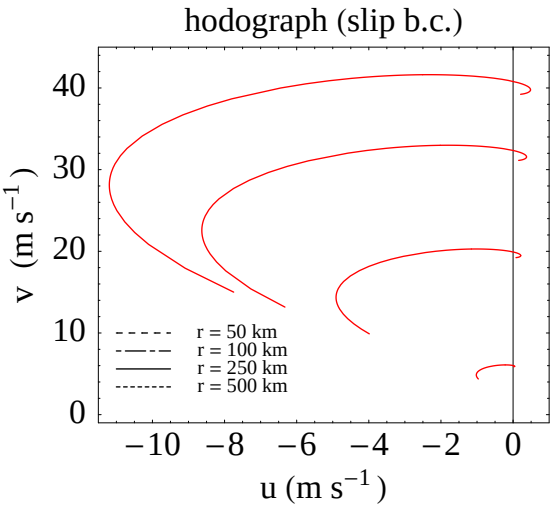

Figure 1.8: Hodographs of the radial and tangential wind speed for four different radii for the slip boundary condition.

Again the wind field can be visualized by the hodographs of the wind vectors for different radii. In Figure (1.8) the hodographs are plotted with radii varying between 50 km and 500 km, showing the turning of the wind vector with height. While for the no-slip condition both $u(r, z)$ and $v(r, z)$ were vanishing at the ground, now for all radii the wind vector has a value different from zero for $z = 0$. Also the angle α between the wind vector and $v_{gr}(r)$ at the ground is different than for the no-slip condition. It is

$$\alpha = \frac{\pi}{2} + \arctan\left(\frac{v(r,0)}{u(r,0)}\right) \tag{1.37}$$

and it follows

$$\alpha = \frac{\pi}{2} + \arctan\left(\frac{a_1(r) - 1}{a_2(r)}\right). \tag{1.38}$$

Clearly, for the slip boundary condition, α is depending on the radius. Figure (1.9) shows the radial variation of α. Far from the core α is about 10 degrees. It is increasing towards the center with a maximum value of about 28 degrees. Further inwards α is decreasing again rapidly.

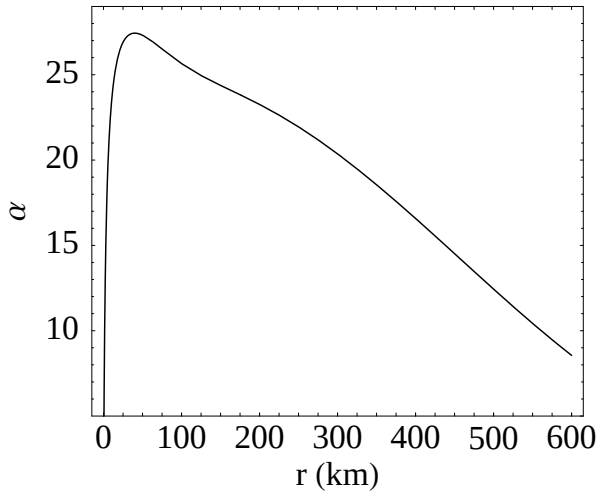

Figure 1.9: Angle α between the vector of the total wind at the ground and $v_{gr}(r)$ as function of the radius.

For the slip boundary condition the values of α are in much better agreement with the observations (e.g. Etling 2002, Holton 2004). Clearly the parametrization of the surface stress by a constant drag coefficient C_D is much more realistic than the no-slip condition.

Now the distribution of the vertical wind speed $w(r, z)$ is investigated. The solution for the radial wind speed derived before was

$$u(r,z) = -v_{gr}(r)e^{-\frac{z}{\delta}}\left(a_1(r)\sin(z/\delta) + a_2(r)\cos(z/\delta)\right)$$

Note that there are three parameters depending on the radius: the wind profile $v_{gr}(r)$ and the two integration constants $a_1(r)$ and $a_2(r)$. Then it is

$$\begin{aligned} f(r,z) &:= -\tfrac{1}{r}\tfrac{\partial}{\partial r}(ru) \\ &= \tfrac{1}{r}e^{-\frac{z}{\delta}}\left[\sin(z/\delta)(rv_{gr}a_1' + a_1(v_{gr} + rv_{gr}')) \right. \\ &\qquad \left. + \cos(z/\delta)(rv_{gr}a_2' + a_2(v_{gr} + rv_{gr}'))\right] \end{aligned} \tag{1.39}$$

and

$$w(r,z) = \int_0^z f(r,z')dz'$$

Solving this integral finally gives:

$$\begin{aligned} w(r,z) = \; & \tfrac{\delta}{2r}e^{-\frac{z}{\delta}}\left[-\cos(z/\delta)\left(v_{gr}(a_1 + a_2 + r(a_1' + a_2')) + r(a_1 + a_2)v_{gr}'\right)\right. \\ & + e^{\frac{z}{\delta}}\left(v_{gr}(a_1 + a_2 + r(a_1' + a_2')) + r(a_1 + a_2)v_{gr}'\right) \\ & \left. + \sin(z/\delta)\left(rv_{gr}(-a_1' + a_2') - a_1(v_{gr} + rv_{gr}') + a_2(v_{gr} + rv_{gr}')\right)\right]. \end{aligned} \tag{1.40}$$

Let

$$A(r) := v_{gr}(a_1 + a_2 + r(a_1' + a_2')) + r(a_1 + a_2)v_{gr}'$$

and

$$B(r) := rv_{gr}(-a_1' + a_2') - a_1(v_{gr} + rv_{gr}') + a_2(v_{gr} + rv_{gr}').$$

Then the expression for $w(r, z)$ may be written in the simple form

$$w(r,z) = \frac{\delta}{2r} e^{-\frac{z}{\delta}} \left[\left(e^{\frac{z}{\delta}} - \cos(z/\delta) \right) A(r) + \sin(z/\delta) B(r) \right]. \tag{1.41}$$

Figure (1.10) shows a contour plot of the vertical velocity $w(r, z)$.

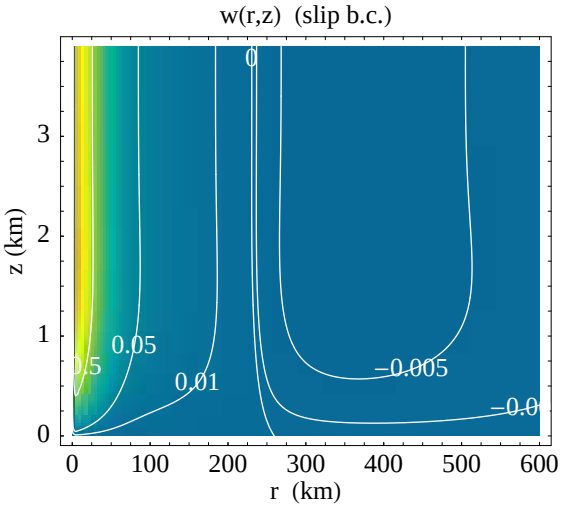

Figure 1.10: Vertical velocity $w(r, z)$ in $\mathrm{m\,s^{-1}}$ for the slip boundary condition.

Similiar to the calculation with the no-slip boundary condition there is very weak inflow at large radii. The maximum upflow is found in the core region of the vortex with values larger than 1 $\mathrm{m\,s^{-1}}$. Again the vertical velocity tends to zero close to the ground level and for heights above 1.5 km w is finally independent of the height z. Analogous to the calculations for the no-slip case a simple analytic expression for w at large z may be derived calculating the limit $z \to \infty$. From equation (1.41) follows that for $z \to \infty$

$$w(r,z) \to \frac{\delta}{2r} \left(v_{gr}(a_1 + a_2 + r(a_1' + a_2')) + r(a_1 + a_2)v_{gr}' \right).$$

This can be written in the form

$$w_\infty(r) = \frac{\delta}{2r} \left(v_{gr}(a_1 + a_2) + r \frac{\partial}{\partial r} \left(v_{gr}(a_1 + a_2) \right) \right).$$

In the case of the slip boundary condition the behaviour of the vertical velocity in the inner core is much more realistic than in the no-slip case. In difference to the calculation shown there the values for $w(r,z)$ are dropping rapidly from their maximum in the eyewall until they reach almost zero in the center of the vortex. Another difference to the no-slip case is that the zero contour line is not independent of height any longer. An analysis of the equation derived for $w(r,z)$ (Eq.(1.41)) confirms that fact. For $w(r,z)=0$ it is

$$\left(e^{\frac{z}{\delta}} - \cos(z/\delta)\right) A(r) = -\sin(z/\delta)B(r)$$

and hence the condition for $r_{w=0}$ is

$$\frac{A(r)}{B(r)} = -\frac{\sin(z/\delta)}{e^{\frac{z}{\delta}} - \cos(z/\delta)}.$$

Clearly $r_{w=0}$ is depending on the parameters A and B and hence it is depending on the height z. As an inspection of the zero contourline in Fig.(1.10) shows, the radius where $w(r,z)$ changes sign converges to the constant value $r = 230$ km for increasing z.

In analogy to the result derived for the no-slip boundary condition this can be calculated from

$$v_{gr}(a_1 + a_2) = -r\frac{\partial}{\partial r}\left(v_{gr}(a_1 + a_2)\right).$$

It is obvious that in the case of the slip boundary condition $w_\infty(r)$ is no longer only depending on the chosen profile for v_{gr}. The real and imaginary part of the integration constant a_1 and a_2 are responsible for the value of $r_{w=0}$ as well. This means that the whole range of chosen parameters as for example drag coefficient or eddy diffusivity influences the behaviour of the solution.

1.3.4 A comparison of the different boundary conditions

It is of interest to compare the results for the two boundary conditions directly, as both are used in the literature. For that purpose the tangential and the radial wind are normalized by the vortex profile v_{gr} and evaluated at a given radius. Figure (1.11) shows the resulting vertical profiles. Panel (a) shows the tangential wind v normalized by $v_{gr}(r)$. Thus for $\frac{v}{v_{gr}} \geq 1$ the obtained winds are supergradient.

The blue graph shows the results for the no-slip, the red one the results for the slip boundary condition. As the no-slip boundary condition forces $v(r,z)$ to vanish at the

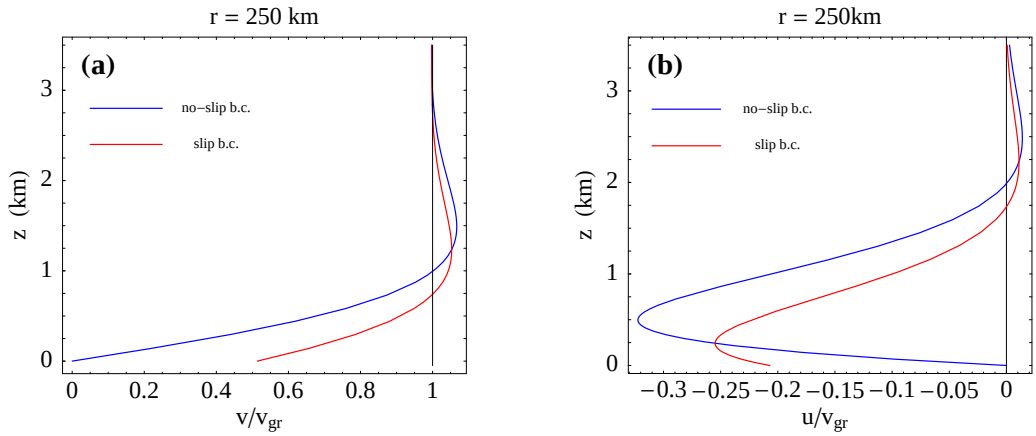

Figure 1.11: Comparison of the tangential wind (panel (a)) and the radial wind (panel (b)) normalized by v_{gr} for a radius of 250 km for the no-slip (blue) and the slip boundary condition (red).

ground while the slip boundary condition allows the tangential wind to attain a non-zero value there is a large difference between the two profiles for $z = 0$. For the slip boundary condition $\frac{v}{v_{gr}}$ attains a value of about 0.5 at $z = 0$. It is also remarkable that the slip boundary condition allows the tangential wind to become supergradient already at a height of about 700 m. This is about 300 m closer to the ground level than for the no-slip case. For both conditions the tangential wind doesn't become subgradient again for heights below about 3 km. However the obtained supergradient winds are generally slightly weaker for the slip case and the maximum is obtained closer to the ground level. In panel (b) of Fig (1.11) the quotient $\frac{u}{v_{gr}}$ is plotted for both boundary conditions. Again there is a large deviation at the ground. While the no-slip condition forces u to vanish, in the slip case $\frac{u}{v_{gr}} = -0.2$. This means that there is inflow even at the ground. In general both solutions show a layer of inflow topped by an outflow layer ($u(r, z) \geq 0$). For the slip case the maximum inflow is less and it is obtained closer to the ground. The flow turns positive already at 1700 m, although admittedly it is always slightly weaker than in the no-slip case. Here the maximum inflow is $\frac{u}{v_{gr}} = -0.3$ obtained at $z = 500$ m and the flow takes positive values at heights above 2 km. Generally, the no-slip boundary condition favoures a stronger inflow in a thicker ground layer topped by a slightly stronger outflow layer above.

Figure (1.12) shows the vertical velocity w for the two different boundary conditions at a height of 2 km. For large distances from the radius of maximum winds, air is slightly floating into the boundary layer which is indicated by small and negative values of

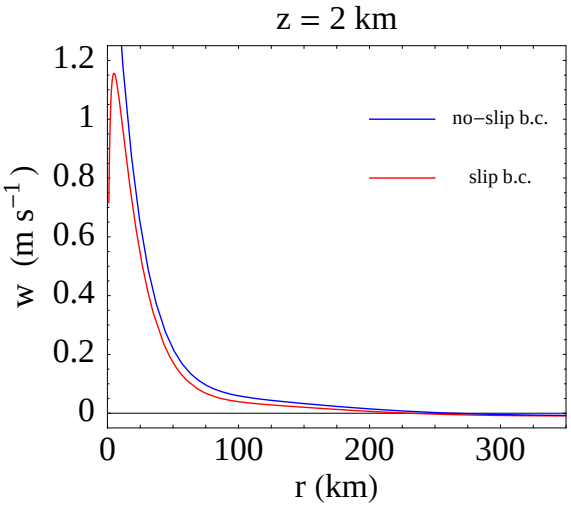

Figure 1.12: Vertical velocity w at a height of 2 km for the no-slip and the slip boundary condition.

the vertical velocity w. Closer to the center the vertical velocity turns positiv and is increasing rapidly. It is remarkable that in the case of the slip condition the vertical velocity is dropping down to almost zero again after reaching its maximum slightly inside r_m while in the case of the no-slip condition this drop isn't found.
With the analytic solutions for the Ekman boundary layer equations one can also easily assess the accuracy of the approximation in the following way:
One can interpret the solutions of the Ekman equations as approximated solutions of the full boundary layer equations and then it is possible to calculate the values of the neglected terms. This will give an approximation of the error resulting from the assumption of a small Rossby number $R_o \ll 1$. A comparison of neglected and retained terms will give further insight into the character of the Ekman approximation.

An inspection of the full set of differential equations Eq.(1.7) and Eq.(1.8) shows that the neglected terms are

$$t_{n1} = u\frac{\partial u}{\partial r} + w\frac{\partial u}{\partial z} + \frac{v_{gr}^2 - v^2}{r}, \tag{1.42}$$

$$t_{n2} = u\frac{\partial v}{\partial r} + w\frac{\partial v}{\partial z} + \frac{uv}{r}, \tag{1.43}$$

while the retained terms are

$$t_{r1} = f(v_{gr} - v), \tag{1.44}$$

$$t_{r2} = fu. \tag{1.45}$$

Using the solutions obtained for the two boundary conditions, these terms can be calculated approximately. The result of the calculation for the no-slip case is shown in Figure (1.13).

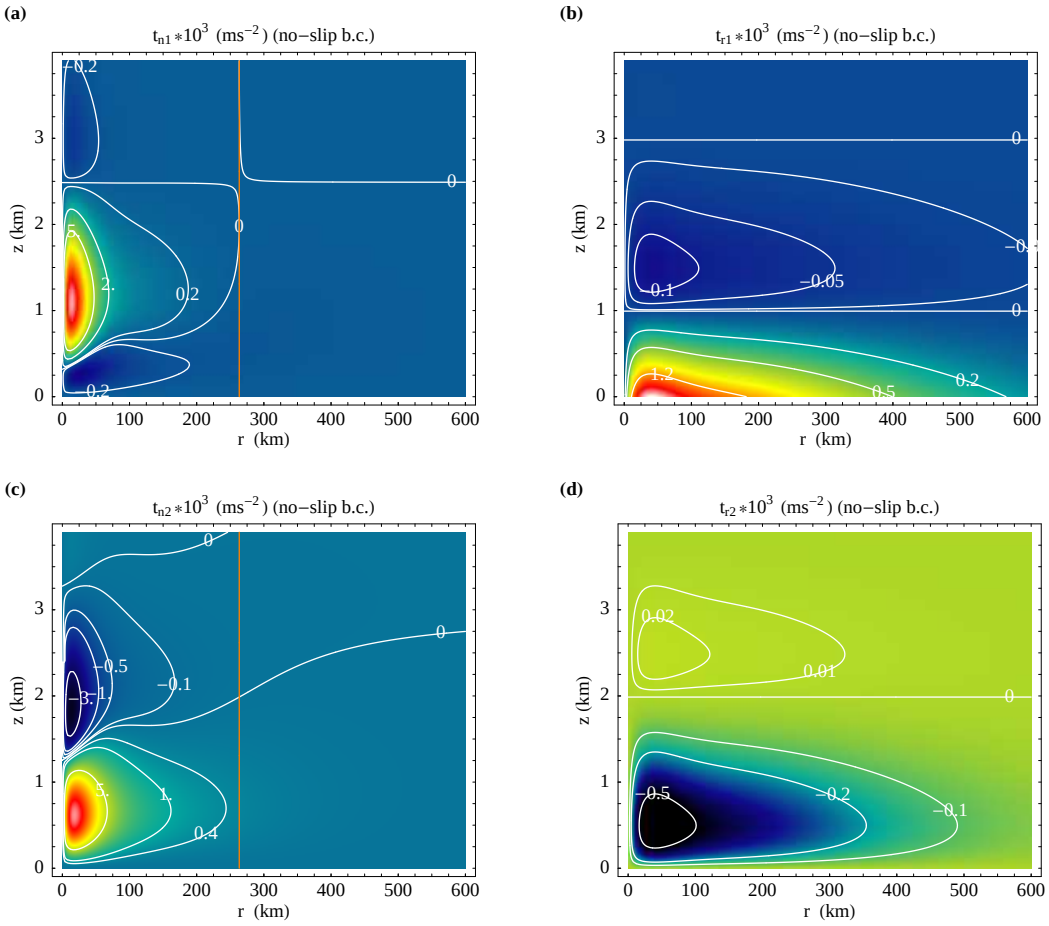

Figure 1.13: Comparison of neglected and retained terms (t_{n1} and t_{r1}) of the full differential equation of the u-momentum (panel (a) and (b)) and the v-momentum (t_{n2} and t_{r2}) in panel (c) and panel (d) for the no-slip boundary condition. The orange vertical line in panel (a) and (d) marks the radius where $w(r, z) = 0$.

As shown in Fig.(1.13) the neglected terms t_{n1} and t_{n2} and the retained terms t_{r1} and t_{r2} are of the same order of magnitude over the entire domain. However the absolute values of t_{n1} and t_{n2} attain their maxima for radii $r < r_m$ and even exceed the maximum values of t_{r1} and t_{r2} by an order of magnitude. This finding emphasizes the fact that the approximation is very crude for a vortex of cyclone strength, especially in the core region. The orange vertical lines in panel (a) and (d) mark the loci where the vertical velocity $w(r, z)$ is changing sign and the flow characteristic is changing from inflow to

upflow ($r_{w=0}$). For radii smaller than $r_{w=0}$, the absolute values of the neglected terms are very small compared to their maxima. Thus one may argue that the assumptions made to derive the Ekman equations are well posed for regions far from the center where v_{gr} is small and $R_o \ll 1$, corresponding to a region where inflow into the boundary layer is found.

For comparison Figure (1.14) shows the same calculation as discussed before for the slip boundary condition.

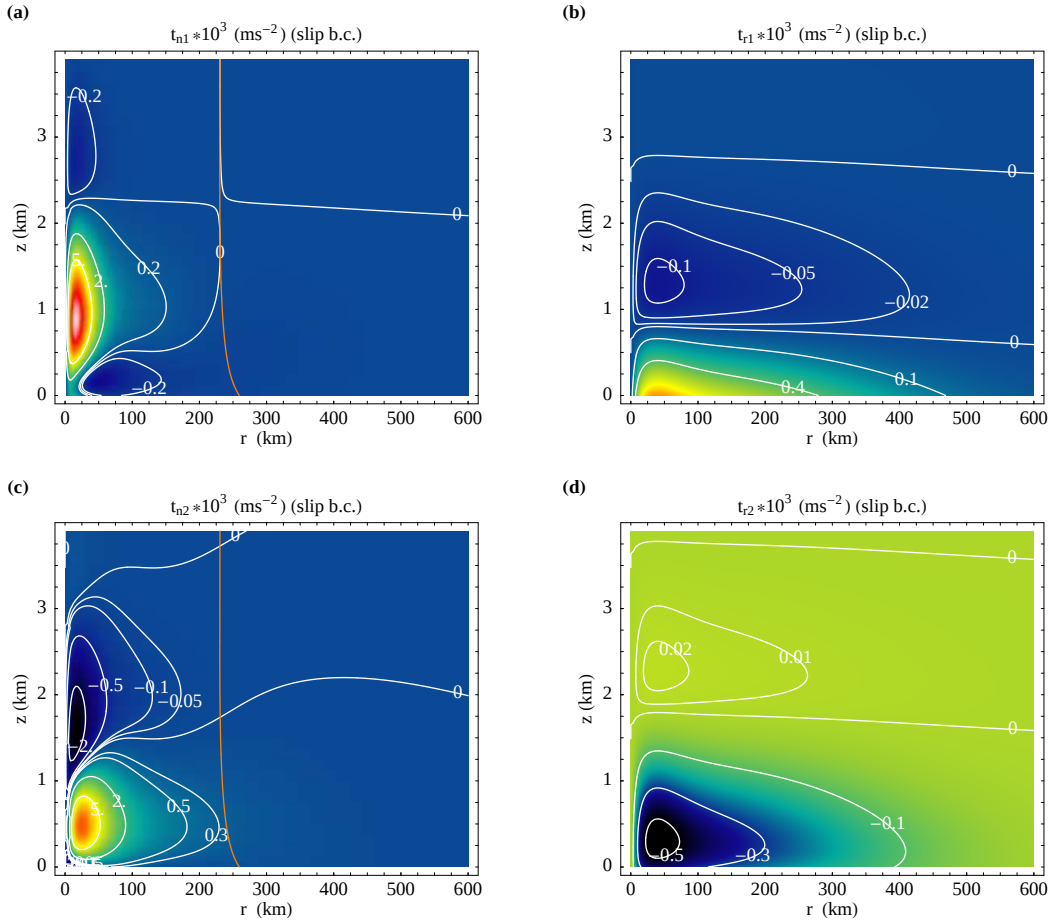

Figure 1.14: Comparison of neglected and retained terms (t_{n1} and t_{r1}) of the full differential equation of u-momentum (panel (a) and (b)) and the v-momentum (t_{n2} and t_{r2}) in panel (c) and panel (d) for the slip boundary condition. The orange vertical in panel (a) and (d) marks the radius where $w(r, z) = 0$.

There are just slight differences notable for the slip boundary condition. The main features are almost the same as in the no-slip case. The neglected and retained terms are of the same order of magnitude all over the domain. The neglected terms attain

their maxima in the inner core and for radii larger than $r_{w=0}$ (marked by the orange curve) their absolute values are small. Thus the same argumentation as for the no-slip case may be applied. The approximation is not significantly improved by imposing the slip boundary condition at the lower bound $z = 0$.

1.4 Discussion of the results

In the first chapter it was shown by the means of a scale analysis how the well known Ekman equations are derived. It was discussed how adequate the approximation is to describe the boundary layer flow in a hurricane. Typical features of this are known to be:

- The turning of the wind vector with height as visualized by the hodographs.
- There is a secondary circulation, which means that there is a low-level jet towards the storm center and in a layer aloft there is outflow.
- Close to the ground a maximum in the tangential flow is found. This means that the winds inside the boundary layer are actually spinning faster than the winds in the free atmosphere. Supergradient winds are obtained.

Although the Ekman eqations were shown to be appropriate only in regions with a small Rossby number (regions far from the storm center), they describe the main features of the boundary layer of a tropical cyclone resonably well: The solutions for the radial flow showed as well the effect of inflow close to the ground level as the region of outflow above and together with the downwards motion at large and the upwards motion at small radii the secondary circulation in the tropical cyclone was reproduced. In the tangential wind field supergradient winds (i.e. $v > v_{gr}$) were obtained.
The results were compared for two different boundary conditions. The first is the no-slip boundary condition which assumes that both the radial and the tangential flow are vanishing at the ground. The second was the slightly more sophisticated slip condition, where the effects of friction at the ground are taken into account. It was shown that the slip condition produced the more realistic results.
The obtained full solutions (u, v, w) were used to estimate the quality of the approximation by comparing the terms which were neglected in the full boundary layer equations

with those that were retained.
It was shown by that comparison that the approximation is not too crude in the outer regions of the storm where the assumption of a balance between the pressure gradient force and Coriolis and frictional force is well satisfied as the effects of rotation are small in that region. It was also shown that the region where Ekman-like solutions are valid is roughly coinciding with the region where air parcels are flowing from above into the boundary layer and carrying their properties with them. Even if the Ekman solutions were shown to be inaccurate in the core region the availability of analytic solutions is of advantage when the most general physical processes are to understand.
The Ekman equations were used before to describe different phenomena inside the boundary layer, but it was the first time that it was shown that they can also be used in the case of a tropical cyclone. Bearing their limitations in mind, they can be appropriate to understand fundemantal physical characteristics of the flow. As will be discussed in the next chapter (2) a similiar ansatz can be used to derive an extended and refined linear model starting with the full boundary layer equations Eq.(1.7) and Eq.(1.8).

Chapter 2

A linear model of the hurricane boundary layer

2.1 Eliassen's linear model applied to a hurricane

The Rossby number is a measure of the magnitude of the acceleration compared to the Coriolis force and hence a small Rossby number reflects good validity of the geostrophic approximation. It was assumed to be small when the Ekman equations were derived. However in the hurricane the Rossby number may become large in the core regions. Therefore, as it was discussed in chapter (1), the Ekman theory for a rotating boundary layer is not really appropriate for the swirling flow in a hurricane.

Although the approximation reveals certain characteristics of the flow, the analysis may be improved further. Now, as an extension of the Ekman theory, a continous model will be derived which is similiar to the linear model developed by Kepert (2001). In that paper he examined the linear equations for a steady boundary layer also allowing for asymmetries in the problem. The linear approximation for a symmetric vortex is an extension of the classical Ekman approach and has the advantage that analytic solutions to the problem are possible. Now it will be shown how the linear model may be derived from a detailed scale analysis of the Navier-Stokes equations. The turbulent stresses are represented by an eddy diffusivity formulation.

An advantage of the linear approach is that it is possible to check the self consistency of the approximation by computing the neglected nonlinear terms. The sensitivity of

the hurricane boundary layer problem to the choice of parameters such as the gradient wind profile at the top of the boundary layer, the Eddy diffusivity or the drag coefficient may be studied in detail using the linear model.

2.1.1 A scale analysis

As in chapter (1) the variation of air density with height is neglected as the boundary layer is assumed to be relatively shallow. As before it is assumed for the present that the turbulent momentum transfer may be represented in terms of a constant eddy diffusivity, K_M. Again the starting point for the calculations are the momentum equations for an axisymmetric vortex, expressed in cylindrical polar coordinates, (r, λ, z):

$$\frac{\partial u}{\partial t} + u\frac{\partial u}{\partial r} + w\frac{\partial u}{\partial z} - \frac{v^2}{r} - fv = -\frac{1}{\rho}\frac{\partial p}{\partial r} + K_M\left(\nabla^2 u - \frac{u}{r^2}\right), \tag{2.1}$$

$$\frac{\partial v}{\partial t} + u\frac{\partial v}{\partial r} + w\frac{\partial v}{\partial z} + \frac{uv}{r} + fu = K_M\left(\nabla^2 v - \frac{v}{r^2}\right), \tag{2.2}$$

$$\frac{\partial w}{\partial t} + u\frac{\partial w}{\partial r} + w\frac{\partial w}{\partial z} = -\frac{1}{\rho}\frac{\partial p}{\partial z} + K_M\nabla^2 w, \tag{2.3}$$

where (u, v, w) is the velocity vector, p is the perturbation pressure and ρ is the density of air. Again the equations are completed by the continuity equation, which for a homogeneous fluid is:

$$\frac{1}{r}\frac{\partial ru}{\partial r} + \frac{\partial w}{\partial z} = 0. \tag{2.4}$$

It is again assumed that the flow at the top of the boundary layer is in gradient wind balance, i.e. it satisfies the equation:

$$\frac{v_{gr}^2}{r} + fv_{gr} = \frac{1}{\rho}\frac{\partial p}{\partial r}. \tag{2.5}$$

The scale analysis, which is accomplished in chapter (1), shows that the radial pressure gradient throughout the boundary layer can be assumed approximately equal to that at the top of the layer. Using this result it is possible to substitute for the pressure

u−momentum

$\frac{\partial u}{\partial t}$	$+u\frac{\partial u}{\partial r}$	$+w\frac{\partial u}{\partial z}$	$-\frac{v'^2}{r}$	$-\xi_{gr}v'$	$=$	$K\frac{\partial^2 u}{\partial z^2}$	(1)
$\frac{U}{T}$	$\frac{U^2}{R}$	$W\frac{U}{Z}$	$\frac{V'^2}{R}$	$\Xi V'$		$K\frac{U}{Z^2}$	(1a)
$S_u^2 S_{v'}^{-1} Ro_\Xi$	$S_u^2 S_{v'}^{-1} Ro_\Xi$	$S_u^2 S_{v'}^{-1} Ro_\Xi$	$S_{v'} Ro_\Xi$	1		$A(R_e S_{v'})^{-1} S_u Ro_\Xi$	(1b)

v−momentum

$\frac{\partial v'}{\partial t}$	$+u\frac{\partial v'}{\partial r}$	$+w\frac{\partial v'}{\partial z}$	$+\frac{uv'}{r}$	$+\zeta_{a_{gr}}u$	$=$	$K\frac{\partial^2 v'}{\partial z^2}$	(2)
$\frac{V'}{T}$	$U\frac{V'}{R}$	$W\frac{V'}{Z}$	$U\frac{V'}{R}$	ΛU		$K\frac{V'}{Z^2}$	(2a)
$S_{v'} Ro_\Lambda$	$S_{v'} Ro_\Lambda$	$S_{v'} Ro_\Lambda$	$S_{v'} Ro_\Lambda$	1		$A(R_e S_u)^{-1} Ro_\Lambda$	(2b)

Table 2.1: Scaling of the terms in Eqs.(2.6) and (2.7). Here $A = Z/R$, $S_u = U/V$, $S_{v'} = V'/V$, $Ro_\Xi = V/(R\Xi)$, $Ro_\Lambda = V/(R\Lambda)$, and $R_e = VZ/K$.

gradient in terms of v_{gr} by the use of Eq.(2.5). The tangential wind speed may be split up into two parts, v_{gr} and the deviation from that, v', called the *tangential wind deficit*. This means it is $v = v_{gr}(r,t) + v'$ and Eqs.(2.1) and (2.2) reduce to:

$$\frac{\partial u}{\partial t} + u\frac{\partial u}{\partial r} + w\frac{\partial u}{\partial z} - \frac{v'^2}{r} - \xi_{gr}v' = K_M\frac{\partial^2 u}{\partial z^2}, \tag{2.6}$$

$$\frac{\partial v'}{\partial t} + u\frac{\partial v'}{\partial r} + w\frac{\partial v'}{\partial z} + \frac{uv'}{r} + \zeta_{a_{gr}}u = K_M\frac{\partial^2 v'}{\partial z^2} \tag{2.7}$$

where

$$\xi_{gr} = \frac{2v_{gr}}{r} + f \qquad \text{and} \qquad \zeta_{a_{gr}} = \frac{dv_{gr}}{dr} + \frac{v_{gr}}{r} + f$$

are the absolute angular velocity and the vertical component of absolute vorticity of the gradient wind.

Now Eqs.(2.6) and (2.7) are inspected in more detail to underpin the final derivation of the linear model.

Let U, V, V' and W be scales for u, v, v', w, and let R and Z be length scales for r and z. Again an advective time scale $T = R/U$ for the radial flow is chosen and Δp denominates a scale for changes in the perturbation pressure, p. As before the ratios in the first lines under each equation in Table (2.1) show the scale of the equation term above it while the second line shows the corresponding nondimensional scales. The latter are obtained by dividing line (1a) in Table (2.1) by $V'\Xi$ to obtain (1b), and

dividing line (2a) in this table by $U\Lambda$ to obtain (2b). Here Ξ is taken as a scale for ξ_{gr} and Λ for $\zeta_{a_{gr}}$. It is seen that the extended analysis now introduces 6 nondimensional parameters:

- $Ro_\Lambda = V/(R\Lambda)$, a local Rossby number in the tangential momentum equation based on the gradient wind (scale V) and the local absolute vorticity of the gradient wind above the boundary layer (Λ);
- $Ro_\Xi = V/(R\Xi)$, a local Rossby number in the radial momentum equation based on twice the absolute rotation rate of the gradient wind, Ξ, instead of Λ;
- $S_u = U/V$, the ratio of the radial to tangential wind speed;
- $S_{v'} = V'/V$, the ratio of the departure of the tangential wind speed from the gradient wind to the gradient wind, itself;
- $R_e = VZ/K$, a *Reynolds number*, which characterizes the importance of the inertial to the friction terms;
- $A = Z/R$, an aspect ratio, which measures the ratio of the boundary-layer depth to the radial scale.

Investigating Table (2.1), it is seen that a vertical scale Z which makes the largest friction terms as important as the linear terms in (1a) and (2a) is such that $\Xi V' \approx KU/Z^2$ and $\Lambda U \approx KV'/Z^2$. From that it follows that $Z = (K/I^*)^{\frac{1}{2}}$, where $I^{*2} = \Lambda\Xi$ is a scale for the inertial stability parameter defined by $I^2 = \xi_{gr}\zeta_{a_{gr}}$. If $Ro = V/(Rf) \ll 1$, ξ_{gr} and $\zeta_{a_{gr}}$ are both approximately equal to f and the vertical scale reduces to $(K/f)^{\frac{1}{2}}$, which is the appropriate scaling for the classical Ekman layer. However the scale analysis in Table (2.1) shows that further approximations are not possible without estimates of the nondimensional parameters $S_u = U/V$ and $S_{v'} = V'/V$ and the radial variations of the local Rossby numbers $Ro_\Xi = V/(R\Xi)$ and $Ro_\Lambda = V/(R\Lambda)$.
As the choice of the tangential wind field v_{gr} is responsible for the values of $Ro_\Xi = V/(R\Xi)$ and $Ro_\Lambda = V/(R\Lambda)$, five different wind profiles are examined below to attain estimates of these parameters.

Figure (2.1) shows five different profiles for the tangential wind field v_{gr} and their absolute vorticity $\zeta_{a_{gr}} = \frac{dv_{gr}}{dr} + \frac{v_{gr}}{r} + f$, where a value of $f = 5 \times 10^{-5}$ s^{-1} is used. The

wind profiles have all the same maximum of 40 $\mathrm{m\,s^{-1}}$ which is attained at a radius of 40 km, but their width is varying. This variation is characterized by the radius of *gale force winds*. That is the radius at which the wind speed exceeds a value of 17 $\mathrm{m\,s^{-1}}$.

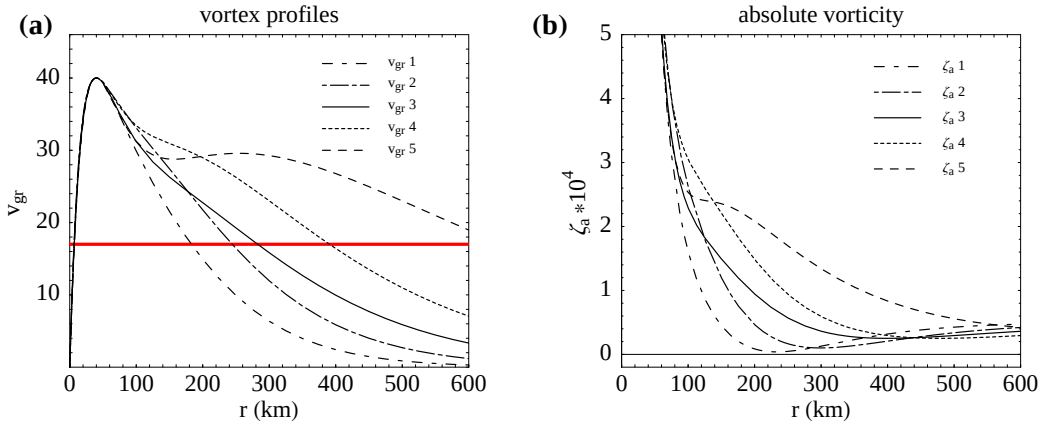

Figure 2.1: wind profiles of v_{gr} with threshold of gale force winds marked in red, (panel (a)), and the absolute vorticity $\zeta_{a_{gr}}$ of these profiles, (panel (b)).

The wind profiles are described and discussed more accurately in the appendix. Figure (2.2) shows the local Rossby numbers $Ro_\Xi = v_{gr}/(r\xi_{gr})$ (panel (a)) and $Ro_\Lambda = v_{gr}/(r\zeta_{a_{gr}})$ (panel (b)), calculated for the five wind profiles shown in Fig.(2.1), panel(a). As $Ro_\Xi = v_{gr}/(r\xi_{gr}) = \frac{vgr/r}{2v_{gr}/r+f}$ it is clear that Ro_Ξ cannot exceed a value of 0.5 and is decreasing with increasing radius. This is valid for all profiles of v_{gr} as Fig.(2.2), panel (a) also confirms.

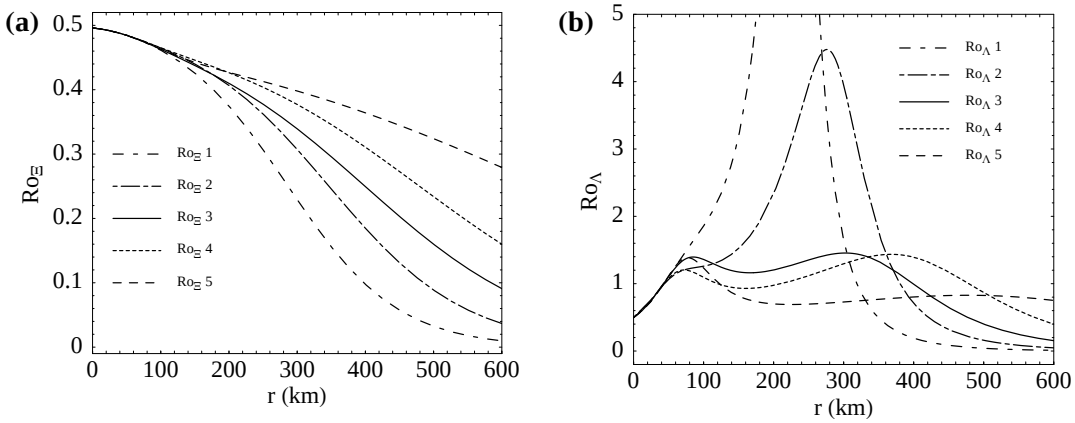

Figure 2.2: $Ro_\Xi = v_{gr}/(r\xi_{gr})$ (panel (a)) and $Ro_\Lambda = v_{gr}/(r\zeta_{a_{gr}})$ (panel (b)) calculated for the five wind profiles shown in Fig.(2.1), (panel (a)).

What is easy to see for Ro_Ξ, namely the existence of an upper bound, is not obvious for

Ro_Λ. Actually this parameter could become quite large for a sufficiently small absolute vorticity. In the calculation shown in Fig.(2.1), panel (b) the largest values for Ro_Λ are obtained for vortex profile 1, which has the smallest absolute vorticity. In that case the maximum value is about 13.

With these estimates for the local Rossby numbers it is now possible to interpret the scale analysis further. If one assumes a situation where the effects of friction are negligible, say S_u and $S_{v'}$ are small compared with unity, the nonlinear terms on the left hand side of Eqs.(2.6) and (2.7) may be neglected. Of course this is only possible in the case where Ro_Λ does not exceed unity appreciably and it is $Ro_\Lambda = O(1)$. Formally it follows from Table (2.1) under the assumption

$$S_u \ll 1, \quad S_{v'} \ll 1 \quad \text{and} \quad Ro_\Lambda = O(1)$$

that the equations (2.6) and (2.7) reduce to the linear system

$$-\xi_{gr} v' = K_M \frac{\partial^2 u}{\partial z^2}, \tag{2.8}$$

$$\zeta_{a_{gr}} u = K_M \frac{\partial^2 v'}{\partial z^2}. \tag{2.9}$$

In the case of $Ro \ll 1$ this system reduces to the classical Ekman equations which were discussed in detail in the foregoing chapter. Calculations with a slab boundary-layer model which are described in detail in chapter (3) show that $U \approx V' \approx 0.2V - 0.3V$. This means that in that special case neither S_u nor $S_{v'}$ are very small compared with unity. Thus in a practical case the approximation is not too good and the solutions are not too accurate. Recently Smith and Montgomery (2008) confirmed this as they showed that in the case of a slab boundary layer model the solutions obtained from a linear model were poor compared to the results with the corresponding nonlinear system.

However, the full nonlinear boundary layer equations in the steady case are parabolic and thus hard to solve. So it is interesting to examine this approximation even though the neglect of terms of magnitude 0.2 - 0.3 compared with unity is unlikely to be very accurate. For one thing the equations (2.8) and (2.9) are relatively easy to solve and they are a generalization of the Ekman layer theory. Another matter of particular interest is to investigate the accuracy of the approximations made, using the obtained analytic solutions of the model.

2.1.2 Analytic solutions

Equations (2.8) and (2.9) may be readily solved by eliminating either u or v' to give a fourth-order ordinary differential equation for the other variable. For example, eliminating u gives

$$\frac{\partial^4 v'}{\partial z^4} + \frac{C^2}{K_M^2} v' = 0 \tag{2.10}$$

where $C^2 = \xi_{gr}\zeta_{a_{gr}}$. General solutions of Eq.(2.10) that are bounded as $z \to \infty$ have the form

$$v'(z) = V_1 e^{-(1-i)\sqrt{\frac{C}{2K_M}}z} + V_2 e^{-(1+i)\sqrt{\frac{C}{2K_M}}z} \tag{2.11}$$

where V_1 and V_2 are constants. This may be written in the form

$$v'(z) = e^{(-\frac{z}{\delta})}(a_1 \cos(z/\delta) + a_2 \sin(z/\delta)) \tag{2.12}$$

where $\delta = \sqrt{2K_M/C}$ is a boundary-layer scale thickness and a_1 and a_2 are constants. The corresponding solution for u is obtained by substituting (2.12) into (2.9):

$$u(z) = -\frac{2K_M}{\zeta_a \delta^2} e^{(-\frac{z}{\delta})}(a_2 \cos(z/\delta) + a_1 \sin(z/\delta)). \tag{2.13}$$

Now a slip boundary condition, as explained in chapter (1.2), is applied at the surface ($z = 0$) with a quadratic drag law for the surface stress. Defining $\vec{x} = (v_{gr} + v', u)$ and a drag coefficient C_D, this condition takes the form

$$K_M \frac{\partial \vec{x}}{\partial z} = C_D |\vec{x}|_{z=0} \vec{x} \quad \text{at} \quad z = 0. \tag{2.14}$$

Substituting the expressions (2.13) for u and (2.12) for v' this becomes

$$\left.\frac{\partial v'}{\partial z}\right|_{z=0} = \frac{(a_2 - a_1)}{\delta} \quad \text{and} \quad \left.\frac{\partial u}{\partial z}\right|_{z=0} = \frac{2K_M}{\zeta_a \delta^2}\frac{(a_1 + a_2)}{\delta}.$$

With $|\vec{x}|_{z=0} = \sqrt{(v_{gr} + a_1)^2 + \left(\frac{2K_M}{\zeta_a \delta^2}\right)^2 a_2^2}$ the boundary condition at the surface finally gives two algebraic equations

$$\begin{aligned} a_2 - a_1 &= \nu\sqrt{(\ldots)}(v_{gr} + a_1), \\ a_2 + a_1 &= -\nu\sqrt{(\ldots)}a_2 \end{aligned} \tag{2.15}$$

where $\sqrt{\ldots} = \sqrt{(1+\frac{a_1}{v_{gr}})^2 + (\frac{2K_M}{\zeta_a\delta^2})^2(\frac{a_2}{v_{gr}})^2}$ and $\nu = C_D R_e$ with $R_e = \frac{v_{gr}\delta}{K_M}$. These two equations can be solved to calculate the coefficients $a_1(r)$ and $a_2(r)$ and to obtain the full solutions $(u(r,z), v(r,z), w(r,z))$ in terms of the local tangential wind speed at the top of the boundary layer, $v_{gr}(r)$. The vertical velocity $w(r,z)$ is obtained by integrating the continuity equation Eq.(2.4).

2.2 Calculations

2.2.1 The control calculation

The control calculation is based on the wind profile vortex 3 plotted in solid in Fig.(4.12). Also a constant eddy diffusivity $K_M = 10$ m^{2}s^{-1}, and a constant drag coefficient $C_D = 2.0 \times 10^{-3}$ are chosen. Let again $f = 5 \times 10^{-5}$ s^{-1}.

Figure (2.3) shows contour plots of the radial wind speed $u(r,z)$ and tangential wind deficit $v'(r,z) = v(r,z) - v_{gr}(r)$ in the boundary layer which are given analytically by:

$$u(r,z) = -\frac{2K_M}{\zeta_{a_{gr}}\delta^2} e^{-z/\delta} \left(a_2(r)\cos(z/\delta) - a_1(r)\sin(z/\delta)\right), \tag{2.16}$$

$$v'(r,z) = e^{-z/\delta} \left(a_1(r)\cos(z/\delta) + a_2(r)\sin(z/\delta)\right). \tag{2.17}$$

As a_1 and a_2 are functions of v_{gr}, the solutions for u and v' are also strongly depending on the chosen profile for v_{gr}. The zero contours in Fig.(2.3) are plotted in red and are also analytically given by

$$z_{u=0}(r) = \delta \arctan\left(\frac{a_2(r)}{a_1(r)}\right), \tag{2.18}$$

$$z_{v'=0}(r) = -\delta \arctan\left(\frac{a_1(r)}{a_2(r)}\right). \tag{2.19}$$

These equations show also that the different regimes for the tangential and the radial

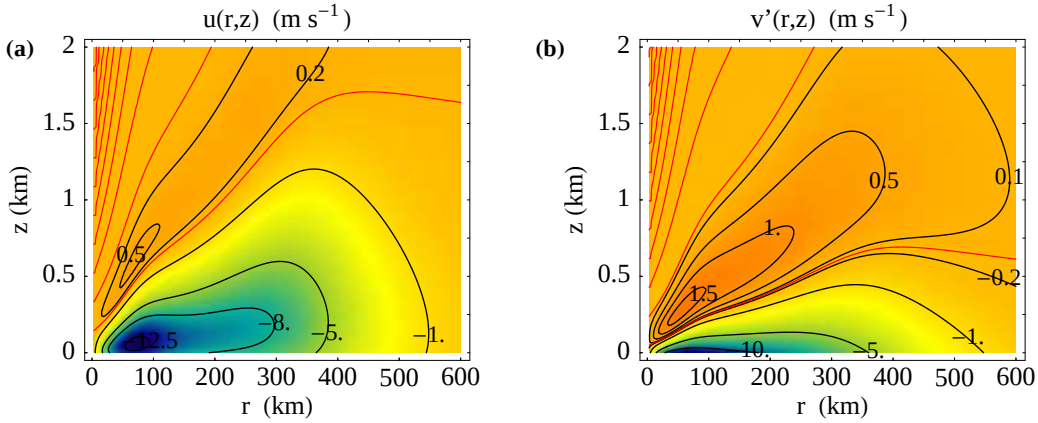

Figure 2.3: Radial wind speed $u(r, z)$ (panel (a)) and tangential wind deficit $v'(r, z) = v(r, z) - v_{gr}(r)$ (panel (b)) in the boundary-layer for vortex 3. The zero contours are plotted in red color.

flow may also be anticipated roughly by an inspection of the boundary layer depth scale δ.

The maximum inflow of about 13.25 m s^{-1} occurs at a radius of 71.5 km, about twice the value of r_m, and at a height of about 54 m above the surface. The cap level of the inflow region ($u(r, z) \leq 0$) is decreasing rapidly from about 1.7 km at a radius of 600 km to almost zero in the core region. Above that layer, limited by the zero contour $z_{u=0}(r)$, there is weak outflow which is strongest ($u(r, z) > 0.5$ m s^{-1}) for radii between 40 km and 100 km and in a height range between 450 m to 850 m.

The tangential winds are supergradient in regions where $v'(r, z) \geq 0$. The domain is divided by $z_{v'=0}(r)$ in a region of subgradient and one of supergradient flow. For the control calculation there is a large area of supergradient winds at heights between about 800 m and 2000 m at radii larger than 400 km and in a much shallower height range at lesser radii. The maximum supergradient winds are 1.7 m s^{-1} and occur at a radius of 55 km and in the height of 271 m. Above the flow turns slightly subgradient again. This area of subgradient flow is coinciding roughly with the region of weak outflow ($u(r, z) > 0$) that occurs above the inflow layer. As it was stated correctly by Kepert (2001) the occurrence of supergradient winds is due to the radial transport of momentum surfaces by frictionally induced inflow. If there was no friction and if one assumes that angular momentum surfaces are close to vertical one would expect the level of supergradient winds to occur close to the level at which the radial wind is maximum. It is seen from Fig. (2.3) that the maximum radial winds occur close to the

surface. This is explained by the fact that friction there produces the largest deviation of the tangential wind from the gradient wind. Therefore the largest net radial force is produced here. With the supergradient winds found in a level distinct from the level of maximum radial inflow it can be deduced that the vertical diffusion of momentum is the factor which explains the structure of the boundary layer in the linear model. In that case the surfaces of absolute angular momentum are not vertical near the surface and there is no conservation of absolute angular momentum by radial motion in the boundary layer.

It is seen from the linear equations that there must be a balance between the generalized Coriolis force, $(\xi_{gr}v', -\zeta_{a_{gr}}u)$, and the vertical diffusion of horizontal momentum, $\frac{\partial^2}{\partial z^2}(u, v')$. An inspection of the level of supergradient winds ($v' > 0$) shows that there the generalized Coriolis force in the radial momentum equation $\xi v'$ is positive and hence is acting radially outwards. In the linear approximation this force is balanced by the upward diffusion of negative radial momentum, $\partial\tau_x < 0$, with a radial stress $\tau_x = K_M(\partial u/\partial z)$ in a height z. In the tangential wind direction a similiar balance may be deduced.

This is an important distinction of the linear to the nonlinear model. In the nonlinear case the vertical advection will also be responsible for some transfer of horizontal momentum in the vertical direction. It has been argued (e.g. Kepert 2001) that this is the primary reason for the deviations of solutions of the linear from the nonlinear model. However it is shown here, that the radial advection is also a crucial factor (see chapter (2.3))!

Now it is possible to derive an analytic solution for the vertical flow $w(r, z)$, evaluating the continuity equation. It is

$$w(r,z) = \frac{\partial}{\partial r}\left(\frac{e^{-z/\delta}K_M r}{\delta\zeta_{a_{gr}}}\left(e^{z/\delta}(a_1 - a_2) - \cos(z/\delta)(a_1 - a_2) - \sin(z/\delta)(a_1 + a_2)\right)\right) \tag{2.20}$$

and finally the expression for $w(r, z)$ takes the form

$$w(r,z) = \frac{e^{-z/\delta}K_M}{r\delta^3\zeta_{a_{gr}}^2}\left[-e^{z/\delta}\delta A + \cos(z/\delta)B + \sin(z/\delta)C\right] \tag{2.21}$$

where

$$
\begin{aligned}
A &= \zeta_a\left(\delta(a_1 - a_2 + r(a_1' - a_2')) - r(a_1 - a_2)\delta'\right) - r(a_1 - a_2)\delta\zeta_{a_{gr}}', \\
B &= \zeta_a\left(\delta^2(a_1 - a_2 + r(a_1' - a_2')) - r(a_2(2z - \delta) + a_1\delta)\delta'\right) - r(a_1 - a_2)\delta^2\zeta_{a_{gr}}', \\
C &= \zeta_a\left(\delta^2(a_1 + a_2 + r(a_1' + a_2')) - r(-2za_1 + (a_1 + a_2)\delta)\delta'\right) - r(a_1 + a_2)\delta^2\zeta_{a_{gr}}'.
\end{aligned}
$$

An inspection of Eq.(2.21) shows, that in the limit $z \to \infty$ the vertical velocity approaches a state where it is independent of height. It is

$$w_\infty(r) = \frac{-K_M}{r\delta^2\zeta_{a_{gr}}^2}A. \tag{2.22}$$

A contour plot of the function $w(r, z)$ (Fig.(2.4)) confirms that result. A similiar shape of the profile is found for all heights $z >$ 150 - 200 m. Just close to the boundary $w(r, z)$ is decreasing rapidly due to the effects of friction and finally the vertical velocity vanishes at $z = 0$.

For any height z > 150 - 200 m, where the vertical flow is almost independent of height, the maximum vertical velocity occurs close to the radius of maximum tangential wind speed in the eyewall, r_m. It is worth to note that the overall maximum value of $w(r, z)$ between the ground level and z = 2 km is not found in the area where the vertical flow is already independent of height, but in a region close to the ground as Fig.(2.4) shows. The absolute maximum value is 0.10 $\mathrm{m\,s^{-1}}$. It appears to be attained just nine kilometers outside r_m in a height of only 431 m in an area where the influence of the surface is still notable.

The solid red line in Fig.(2.4) marks the point where w is zero and the vertical flow is changing sign. In the limit $z \to \infty$ the zero contour is given by the condition $A = 0$ because $\frac{-K_M}{r\delta^2\zeta_{a_{gr}}^2} \neq 0$. As shown in Fig.(2.4) the radius where $w(r, z) = 0$ stays almost constant for the whole range of z not only for large heights. Thus the two different flow regimes, namely the region of inflow and upflow are clearly divided by an almost constant radius $r_{w=0}$.

Fig.(2.5) shows the boundary layer depth scale δ and the vertical velocity at a height of z = 2 km for this calculation. Note that δ decreases rapidly towards the vortex center, a consequence of the significant growth of both ξ_{gr} and $\zeta_{a_{gr}}$ with increasing wind speed.

The maximum vertical velocity is 9.5 $\mathrm{cm\,s^{-1}}$ and is attained at a radius of 49 km, just nine kilometers outside r_m. Fig.(2.5) also shows that w is negativ for radii larger than

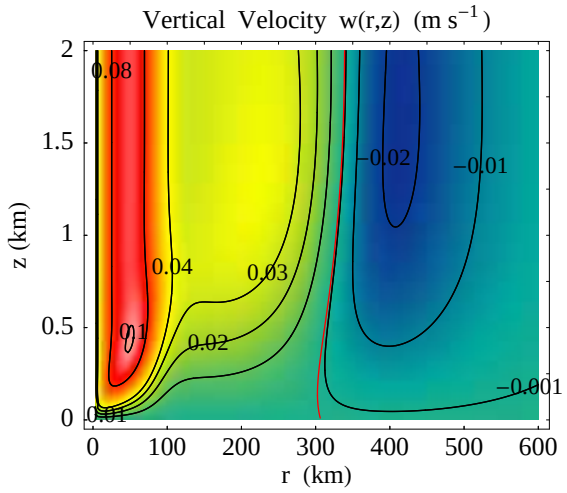

Figure 2.4: Vertical velocity w(r,z) for vortex 3 in m s^{-1}; the red curve marks $w(r, z) = 0$.

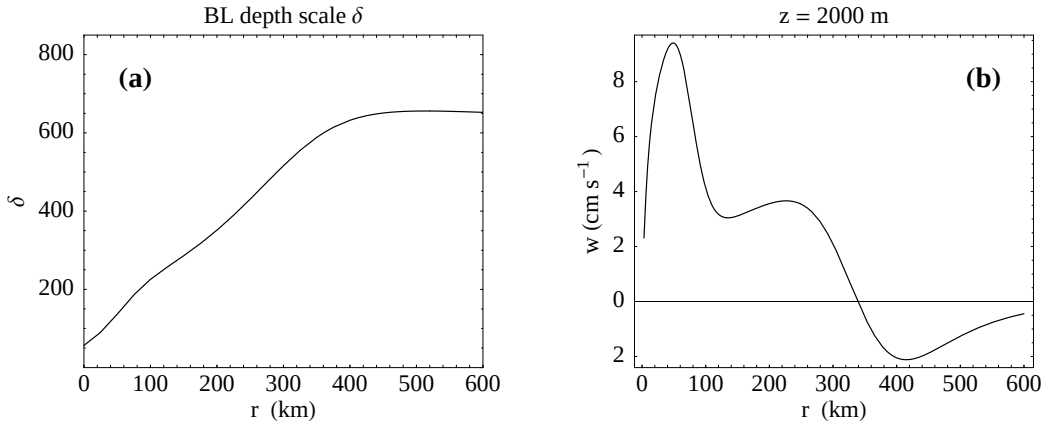

Figure 2.5: Boundary-layer depth scale δ (panel (a)) and vertical velocity w (panel (b)) at a height of z = 2000 m for vortex profile 3.

339 km where it changes sign. Thus the flow is directed inward the boundary layer for large radii. The fact that there is a large area where the air is ascending is representing an important limitation of the linear model for the case of the hurricane boundary layer. This will be discussed later together with the question how accurate the linear solution may be especially in regions where there is found strong radial advection (see chapter (2.3)).

2.2.2 Dependence on the vortex profile

An inspection of the boundary-layer depth scale shows that the parameters that are of importance for the flow evolution are the eddy diffusivity K_M and the characteristics of the vortex profile $v_{gr}(r)$ at the top of the boundary layer. Fig.(2.6), panel (a), shows the depth scale δ for the five different profiles shown in Fig.(4.12). The results for δ are very similiar for all profiles at large radii and also in the core region. However, at intermediate radii, notable deviations are found. This differences are due to differences in the intermediate inertial parameters, which are smaller for narrower vortices due to a more negative relative vorticity.

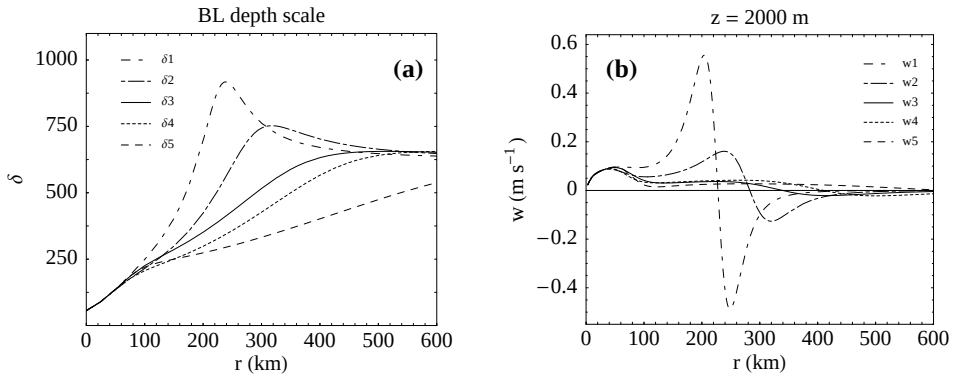

Figure 2.6: (a) Boundary-layer depth scale δ for wind profiles vortex 1 - vortex 5 and (b) corresponding vertical velocity $w(r, z)$.

The depth scale has its maximum value at a radius of 600 km for profiles 3 to 5. The obtained maximum value is 540 for profile 5 and increasing to a value of 670 for profiles 3 and 4. Profiles 1 and 2 both have their maximum towards the center. Profile 1 peaks at $r = 230$ km with a value of 920, profile 2 has its maximum at $r = 310$ km and reaches a value of 750. Towards the center the scales are steadily decreasing for all five profiles until they share a value of 70 at $r = 0$ km. In the center of the covered area at a radius of about 200 - 300 km the difference beween the obtained depth scales is largest. While δ stays more or less constant with a value of about 650 km up to a radius of 300 km for vortex 1, it has already declined to about 70 percent of its starting value for vortex 5. As Fig.(2.6), panel (a) shows, the result for vortex 1 is substantially different from the others. For vortex 1, the depth scale δ shows a considerable increase and a significant local minimum. This pronounced maximum and local minimum is unique for that vortex profile. As expected the results for the vertical velocity $w(r, z)$ reflect

those for the depth scale δ. The profiles for w corresponding to vortex 1 and vortex 2, the ones with a pronounced peak, show both a local maximum in the region where the flow is directed out of the boundary layer ($w(r,z) > 0$). The results for vortex 3 - vortex 5 are very similiar in shape and the attained range of values but it is remarkable that the radius where the flow changes sign is significantly depending on δ. For vortex 1 and thus for the largest δ air parcels are transported into the boundary layer for radii larger than 227 km. With decreasing depth scale this is changing dramatically. For vortex 3 the radii have already to be larger than 340 km and for vortex 5 $w(r,z)$ is positive for all radii shown in Fig.(2.6 (b)).

As profiles 2 - 5 do not differ substantially, only the results of the calculations carried out for vortex 2 and vortex 5 are shown. It was shown before in section (2.1.1) that the linear approximation is only performing acceptable for the case of a profile where $Ro_\Lambda = v_{gr}/(r\zeta_{a_{gr}})$ is of order unity. However this was not true for profile one where Ro_Λ was shown to attain a maximum value of about 13. Hence it doesn't make sense to investigate this profile in the case of the linear approximation. Figure (2.7) shows the result for $u(r,z)$ and $v'(r,z)$ for vortex profiles 2 and 5.

Panels (a) and (c) of Fig.(2.7) show a comparison of the radial wind speed $u(r,z)$. The result for vortex 5 (Fig.(2.7), panel (c)) is very similiar to the control calculation but shows some special features. A region of strong inflow is topped by a layer of weak outflow.

An inspection of the boundary layer depth scale δ for vortex 5 (Fig.(2.6)) anticipates the result for the contour line $u(r,z) = 0$, as motivated by Eq.(2.18). The maximum inflow of about $-12.5\ \mathrm{m\,s^{-1}}$ appears near the ground close to the radius of maximum winds r_m. This is similiar to the result for vortex 3, but the inflow stays at a high level of about $-7\ \mathrm{m\,s^{-1}}$ for all radii, while for the control calculation it is decreasing almost linearly until it reaches $-0.5\ \mathrm{m\,s^{-1}}$ at $r = 600$ km. A comparison of the depth scale δ for vortex 3 and vortex 5 shows that at large radii, δ is much smaller for vortex 5 and there is also found a much shallower inflow layer for vortex 5. And according to the δ-profile for vortex 2, the steepest contour line $u(r,z) = 0$ is found for vortex 2 (Fig.(2.7), panel (a)). Similiar to the control calculation the values for $u(r,z)$ near the ground are decreasing almost linearly from $-12\ \mathrm{m\,s^{-1}}$ to $-0.5\ \mathrm{m\,s^{-1}}$ at $r = 600$ km, but now the maximum is about $-14\ \mathrm{m\,s^{-1}}$ and lies in a height of about 270 m and with a radius of 250 km far from the core region.

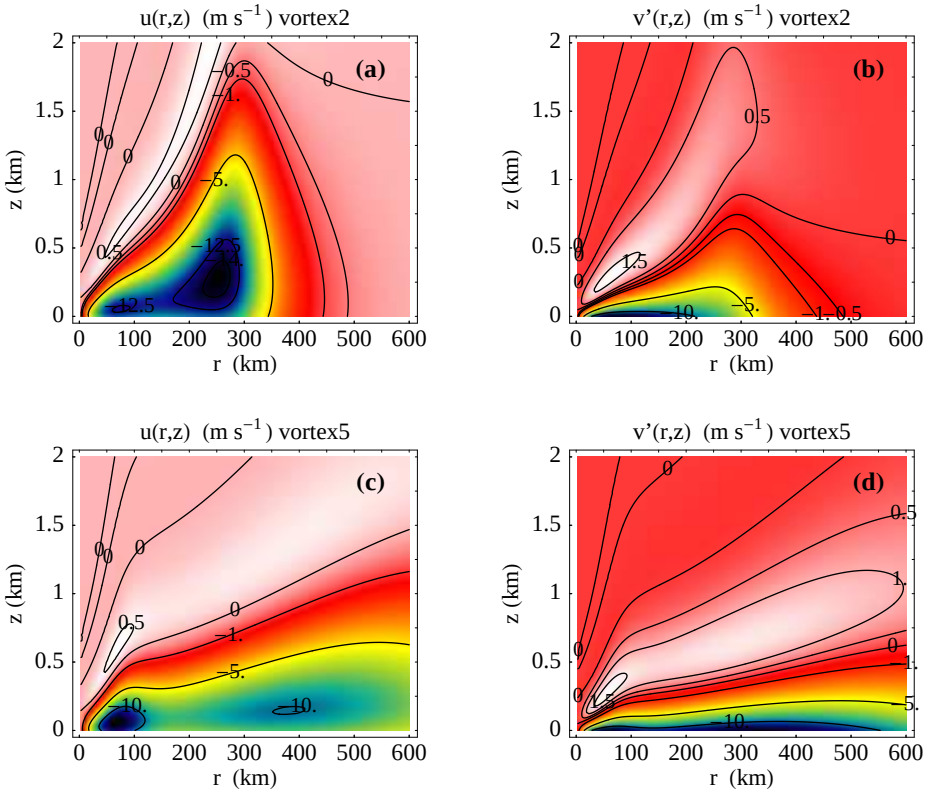

Figure 2.7: Wind speeds $u(r, z)$ and wind deficit $v'(r, z)$ for vortex profile 2 (panel (a) and (b)) and vortex profile 5 (panel (c) and (d)).

Panels (b) and (d) of Fig.(2.7) show a comparison of the tangential wind deficit $v'(r, z)$. For vortex 2 the tangential wind deficit close to the ground is decreasing with increasing radius whereas for vortex 5 high values are obtained for all radii. Both distributions show supergradient flow of about 1.5 m s^{-1} but for vortex 5 the area, where the flow is significantly supergradient, is covering all radii and is lying in a height range of 200 m close to the core and 1.5 km for $r = 600$ km while for vortex 2 $v'(r, z) \leq 0.5$m s^{-1} for all radii larger than 300 km.

2.2.3 The influence of eddy diffusivity

As an inspection of the full solution (u, v, w) has shown that the boundary layer depth scale $\delta = \sqrt{2K_M/C}$ is the determining factor of the obtained profiles and therefore (equally important as the choice of the profile for v_{gr}) the choice of the eddy diffusivity K_M must be of high influence for the solution. A range of constant values of K_M is

investigated now to highlight the importance of this parameter.

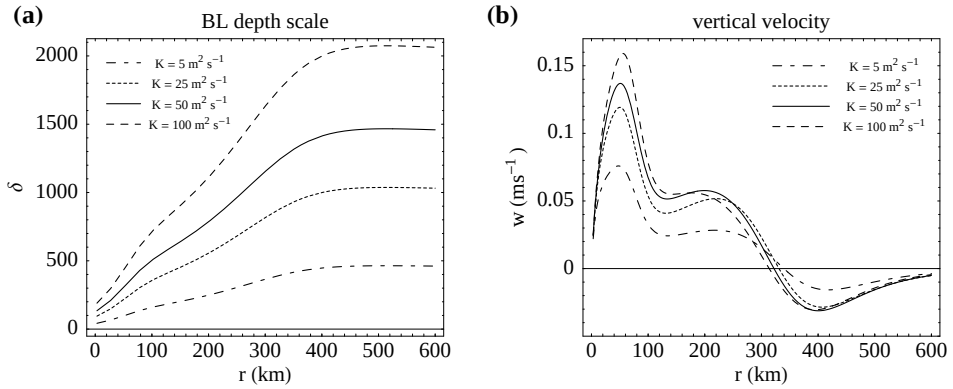

Figure 2.8: Boundary layer depth scale δ (panel (a)) and vertical velocity $w(r, z)$ (panel (b)) for varying K_M for vortex profile 3.

Figure (2.8) panel (a) shows the resulting boundary layer depth scale δ for values of K_M varying between 5 m^2s^{-1} to 100 m^2s^{-1}. The range of values used for K_M follows the values that appear in the literature as for example in Kepert (2001) ($K_M = 5$ m^2s^{-1}) or Montgomery *et al.* (2001) which used a value of $K_M = 50$ m^2s^{-1} and provided an estimate of the eddy diffusivity of $K_M = 500$ m^2s^{-1}, using data from hurricane "Norbert" (1984), presented by Marks *et al.* (1992). This exemplifies the fact that there is a wide range of values for K_M in use. As δ is proportional to the square root of K_M the boundary layer depth scale increases with increasing K_M. In all cases δ is almost constant for radii between 400 km and 600 km and decreases rapidly towards the center. For $K_M = 5$ m^2s^{-1} the maximum value is about 500 while for $K_M = 100$ m^2s^{-1} it is four times larger with a value of about 2000. Panel (b) of Figure (2.8) shows the corresponding vertical velocity w. As expected the maximum vertical velocity is obtained in the core region and increases with increasing values of K_M. For $K_M = 5$ m^2s^{-1} the maximum (w_{max}= 0.08 $m\,s^{-1}$) lies at a radius of about 47 km while for K_M = 100 m^2s^{-1} it is already w_{max}= 0.16 $m\,s^{-1}$ at a slightly larger radius of 54 km. Figure (2.8) shows also that the region of upflow ($w > 0$) changes slightly with varying K_M.

Figure (2.9) panel (a) shows the significant increase in the vertical velocity with increasing eddy diffusivity. If K_M is varied from 5 m^2 s^{-1} to 100 m^2 s^{-1} the maximum of w doubles. Panel (b) of Figure (2.9) shows that the radius where w changes sign decreases from 340 km to about 315 km. This radius stays almost constant if z is varied. Thus the region where there is upflow in the boundary layer is smaller for large values of the eddy diffusivity. The results for the distributions of the radial velocity

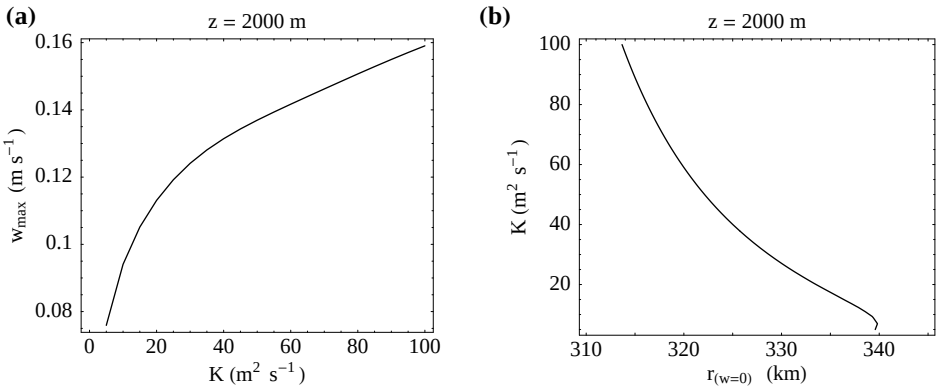

Figure 2.9: Maximum of vertical wind speed w_{max} (panel (a)) and the radius of the vortex where $w = 0$ (panel (b)) for varying K_M for $z = 2000$ m.

$u(r, z)$ and the tangential wind deficit $v'(r, z)$ can be deduced from the profiles of δ shown in Fig.(2.8), panel (a), as it is seen from Eqs.(2.18).

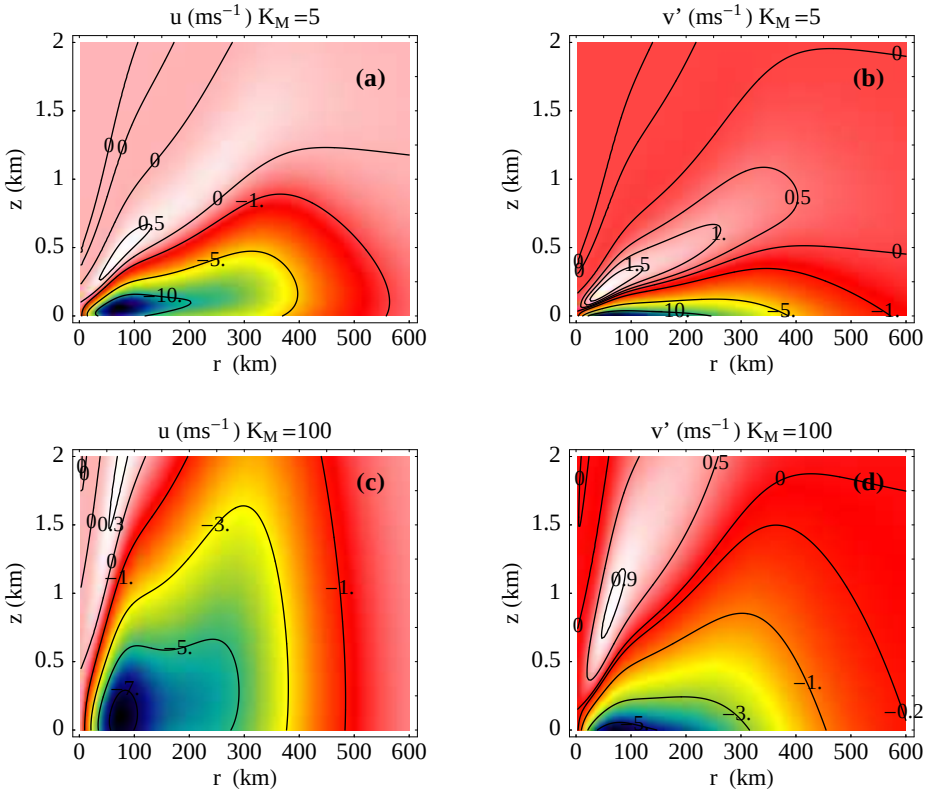

Figure 2.10: Wind speeds $u(r, z)$ and wind deficit $v'(r, z)$ for $K_M = 5$ m^{2}s^{-1} (panel (a) and (b)) and $K_M = 100$ m^{2}s^{-1} (panel (c) and (d)).

Figure (2.10) highlights the importance of the choice of a realistic eddy parameter K_M

for the solutions of the linear approximation. As expected the region of inflow for K_M = 5 m^2s^{-1} expands near the ground level at heights varying from about 1 km at a radius between 400 km and 600 km and declines rapidly towards the core region. It is topped by a layer of week outflow. The maximum of about 12 $m\,s^{-1}$ is obtained near the radius r_m where v_{gr} has it's maximum, close to the ground. For $K_M = 100$ m^2s^{-1} the result changes significantly. The maximum value is a bit lower, 7 $m\,s^{-1}$, but now there is inflow almost throughout the whole region except at heights larger than 500 m in the core region ($r < 100$ km).

2.2.4 A non-constant representation of the drag coefficient

Another parameter of great importance is the value of the drag coefficient C_D. In chapter (1) a slip boundary condition at the surface ($z = 0$) was applied with a quadratic drag law for the surface stress. Defining $\vec{x} = (v_{gr} + v', u)$ it was

$$K_M \frac{\partial \vec{x}}{\partial z} = C_D |\vec{x}|_{z=0}\, \vec{x} \quad \text{at} \quad z = 0. \tag{2.23}$$

Clearly the choice of the drag coefficient is important for the solutions obtained for $\vec{x}$. Now it is investigated how accurate the choice of a constant value for C_D is and how much the solutions are influenced by that parameter. Calculations are carried out with three different representations of C_D. The first one is the control calculation as described in section (2.2.1) which uses vortex 3, a constant Eddy diffusivity of $K_M = 10 m^2s^{-1}$ and a constant drag coefficient $C_D = 2.0 \times 10^{-3}$. The second calculation is as the control calculation but with a smaller drag coefficient of $C_D = 1.0 \times 10^{-3}$ and the third one uses a radially varying value for C_D. Following Shapiro (1983) for the third case study it is defined:

$$C_D = C_{D0} + C_{D1} |\vec{x}|_{z=0} \tag{2.24}$$

which means that starting from a value $C_{D0} = 1.1 \times 10^{-3}$ the drag coefficient is a linear function of the absolute value of the total wind speed $\vec{x} = (v_{gr} + v', u)$.

Again the starting point is the expressions for the radial wind speed and the tangential wind deficit derived before:

$$
\begin{aligned}
v'(z) &= e^{(-\frac{z}{\delta})}(a_1\cos(z/\delta) + a_2\sin(z/\delta)), \\
u(z) &= -\frac{2K_M}{\zeta_{a_{gr}}\delta^2}e^{(-\frac{z}{\delta})}(a_2\cos(z/\delta) - a_1\sin(z/\delta)).
\end{aligned}
$$

The slip boundary condition is applied at $z = 0$, but now with a drag coefficient calculated with Eq.(2.24). For C_D at $z = 0$ it is

$$
C_D = C_{D0} + C_{D1}\sqrt{(v_{gr} + a_1)^2 + \left(\frac{2K_M}{\zeta_{a_{gr}}\delta^2}\right)^2 a_2^2}
$$

and the boundary condition gives now two equations for the parameters a_1 and a_2:

$$
\begin{aligned}
a_2 - a_1 &= R_e(C_{D0} + C_{D1}|\vec{x}|_{z=0})\sqrt{(\ldots)}(v_{gr} + a_1), \\
a_2 + a_1 &= -R_e(C_{D0} + C_{D1}|\vec{x}|_{z=0})\sqrt{(\ldots)}a_2,
\end{aligned}
\tag{2.25}
$$

where $\sqrt{\ldots} = \sqrt{(1 + \frac{a_1}{v_{gr}})^2 + (\frac{2K_M}{\zeta_{a_{gr}}\delta^2})^2(\frac{a_2}{v_{gr}})^2}$ and $R_e = \frac{v_{gr}\delta}{K_M}$.

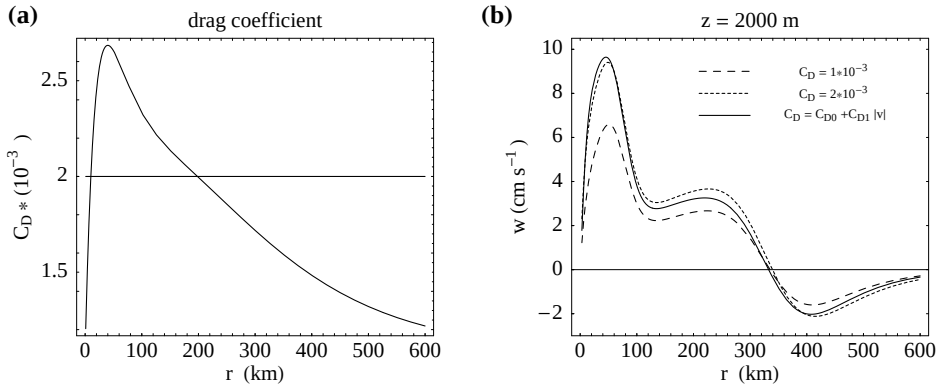

Figure 2.11: Radially varying drag coefficient C_D (panel (a)) and the vertical wind speed $w(r)$ (panel (b)) for varying C_D for $z = 2000$ m.

Figure (2.11) panel (a) shows the radially varying drag coefficient derived from Eq.(2.24) with $C_{D0} = 1.1 \times 10^{-3}$ and $C_{D1} = 4 \times 10^{-5}$. The solid line marks the value for C_D in the control calculation. At large radii where the absolute value of the total wind speed is small, C_D is close to C_{D0}, then it increases rapidly with increasing total wind speed until it reaches its maximum value of $C_D = 2.6 \times 10^{-3}$ at the radius of maximum wind speed $r_m = 40$ km. For radii smaller than r_m C_D drops off rapidly following the behaviour of the total wind speed in the core region. Figure (2.11) panel (b) shows the vertical wind speed $w(r)$ at a height of $z = 2$ km calculated with the three cases

described above. For a constant drag coefficient $C_D = 1.0 \times 10^{-3}$ the lowest vertical velocities are obtained. The maximum value of 6.5 $\mathrm{cm\,s^{-1}}$ is obtained at a radius of 51 km and is significantly lower than for $C_D = 2.0 \times 10^{-3}$. In the control calculation we find 9.4 $\mathrm{cm\,s^{-1}}$ at almost the same radius ($r = 49$ km). All three velocity profiles change sign at about $r = 335$ km with a variation of only ± 3 km. In general the absolute value of the vertical velocity is lower for smaller C_D. As the radially varying drag coefficient is lower than $C_D = 2.0 \times 10^{-3}$ for radii larger than 200 km the absolute value of w is lower than in the control calculation for those radii. But the response of the vertical velocity to an enhanced drag is not an immediate one. The solutions have to adjust to the enhanced drag. Just for radii smaller than about 53 km larger vertical velocities are obtained. However the maximum value (at $r = 45$ km) is 9.6 $\mathrm{cm\,s^{-1}}$ and thus just slightly larger as in the control calculation. In general the largest differences between the control calculation and the case with a radially varying drag coeffficient are just 0.5 $\mathrm{cm\,s^{-1}}$ obtained for radii of about 230 km.

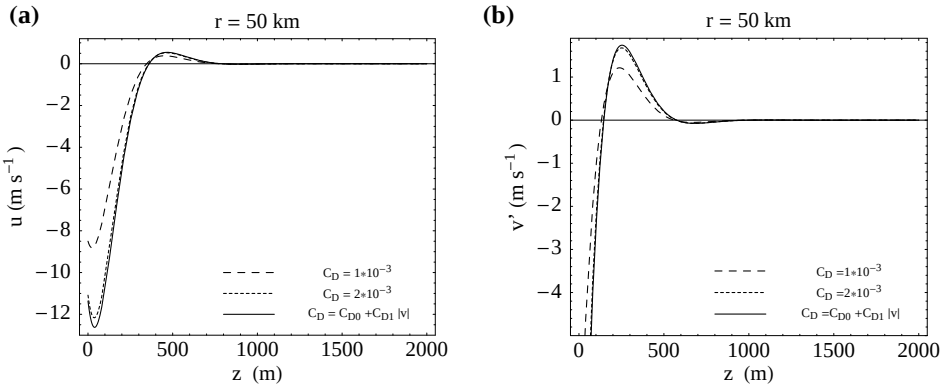

Figure 2.12: Radial wind speed $u(z)$ at $r = 50$ km (panel (a)) and the wind deficit $v'(z)$ at $r = 50$ km (panel (b)) for varying C_D.

Figure (2.12) panel (a) shows the radial wind speed $u(z)$ at a radius of 50 km close to the radius of maximum winds r_m. For the calculation with the underestimated drag coefficient in general lower radial wind speeds with significant deviations in the region close to the ground are found. There the radial wind for $C_D = 1.0 \times 10^{-3}$ is -8.7 $\mathrm{m\,s^{-1}}$ while for $C_D = 2.0 \times 10^{-3}$ it is -12.1 $\mathrm{m\,s^{-1}}$ and for the case of radially varying drag the highest value of -12.6 $\mathrm{m\,s^{-1}}$ is obtained. In general the control calculation and the calculation with a radially varying C_D do not show large differences. The deviation of about 0.5 $\mathrm{m\,s^{-1}}$ at the peak is the largest one for all heights z.

A similiar result is found for the tangential wind deficit at $r = 50$ km which is shown

in Figure (2.12) panel (b). An underestimation of C_D leeds to an underestimation of the wind deficit and especially of the tendency of supergradient winds ($v' > 0$). With increasing drag the maximum of the wind deficit is increasing from 1.25 $\mathrm{m\,s^{-1}}$ to 1.7 $\mathrm{m\,s^{-1}}$ for the control and finally 1.77 $\mathrm{m\,s^{-1}}$ for the radially varying drag coefficient. Again the difference of 0.07 $\mathrm{m\,s^{-1}}$ at the peak is the largest one for the control calculation and $C_D = C_{D0} + C_{D1}|\vec{x}|$.

The fact that the differences between the control calculation and the radially varying drag coefficient shown in Figure (2.11) and Figure (2.12) are small, it is concluded that the assumption of a constant drag coefficient of $C_D = 2.0 \times 10^{-3}$ as in the control calculation is a good approximation for the model studied in this chapter and there is no significant improvement of the results when a more sophisticated representation of this parameter is used.

2.3 An appraisal of the linear approximation

Based on the full solution for $u(r,z), v(r,z)$ and $w(r,z)$ it is possible to assess the accuracy of the linear approximation. As a steady state is assumed it is $\frac{\partial u}{\partial t} = 0$ and $\frac{\partial v'}{\partial t}$ and Equations (2.6) and (2.7) were simplified by omitting the terms

$$t_{n1} = u\frac{\partial u}{\partial r} + w\frac{\partial u}{\partial z} - \frac{v'^2}{r}$$

and

$$t_{n2} = u\frac{\partial v'}{\partial r} + w\frac{\partial v'}{\partial z} + \frac{uv'}{r},$$

respectively.

If $u(r,z), v'(r,z)$ and $w(r,z)$ are understood as approximate solutions of Eq.(2.6) and Eq.(2.7) the terms t_{n1} and t_{n2} can be interpreted as deviations of the complete equationset from the linear equations. They should be small compared with unity!

An estimate of the values of these expressions can be calculated using the solution of the linearized system. To appraise the accuracy of the linear approximation t_{n1} and t_{n2} are compared with the terms retained:

$$t_{r1} = -\left(\frac{2v_{gr}(r)}{r} + f\right)v'(r,z)$$

and

$$t_{r2} = \left(\frac{\partial v_{gr}(r)}{\partial r} + \frac{v_{gr}(r)}{r} + f \right) u,$$

respectively. Figure (2.13) shows this comparison.

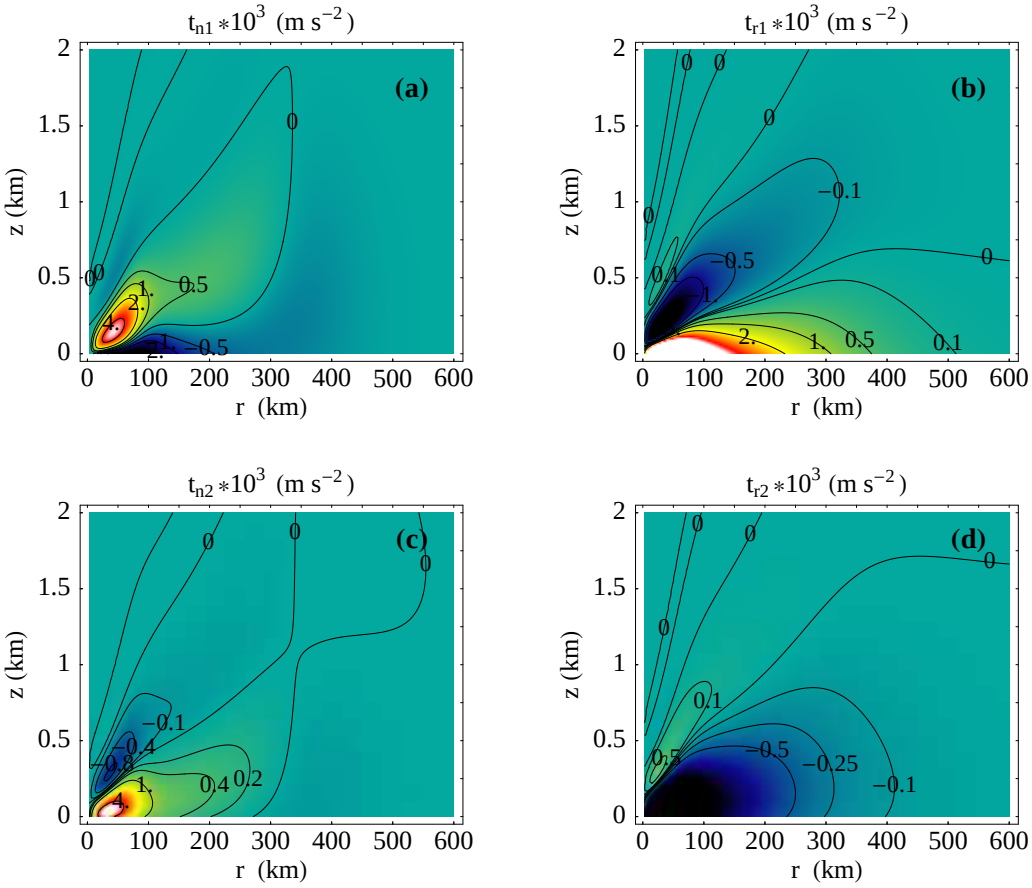

Figure 2.13: Evaluation of neglected terms t_{n1} and retained terms t_{r1} in Eq.(2.6), (panels (a) and (b)) and terms t_{n2} and t_{r2} in Eq.(2.7), (panels (c) and (d).

As expected the largest absolute values of t_{n1} and t_{n2} occur in a region close to the surface and the core region where the gradients for u and v' are large (Fig.(2.13), panels (a) and (c)). However the quality of the approximation can not only be evaluated by an examination of the absolute errors made but must also include a comparison with the nonneglected terms. Fig.(2.13) shows that the terms t_{r1} and t_{r2} are of the same order of magnitude as the values obtained for t_{n1} and t_{n2} over much of the region which is of interest. It is seen that the zero contours of t_{n1} and t_{n2} do not coincide with those of the retained terms t_{r1} and t_{r2}. Thus a comparison in terms of ratios of neglected to retained terms is very difficult to interpret. The neglected terms gain influence not only

in the core region, where their absolute values are largest, but also in areas where both neglected and retained terms become small at the same time. To compare the order of magnitude of the retained and neglected terms the relative error can be computed. Let

$$e_{rel1} = \left| \frac{t_{n1}}{t_{n1} + t_{r1}} \right|, \tag{2.26}$$

$$e_{rel2} = \left| \frac{t_{n2}}{t_{n2} + t_{r2}} \right| \tag{2.27}$$

be the relative errors of the terms which were neglected in Eq.(2.6) and Eq.(2.7). Figure 2.14 shows the logarithm of relative errors e_{rel1}, (panel (a)), and e_{rel2}, (panel (b)), of the approximation for Eq.(2.6) and Eq.(2.7). As an inspection of Figure (2.13) suggests, there is a large relative error not only in the core region but spreading over the whole domain. In Figure (2.13) the singularities at $t_{n1} + t_{r1} = 0$ and $t_{n2} + t_{r2} = 0$ dominate the picture, but they contribute little if the whole domain is taken into account.

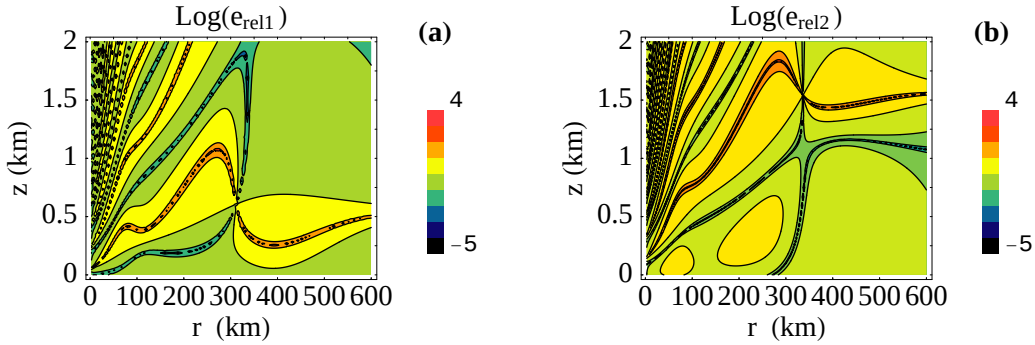

Figure 2.14: Logarithm of relative error e_{rel1}, (panel (a)) and relative error e_{rel2}, (panel (b)).

For large regions of the domain the neglected terms are of the same order of magnitude as the retained ones and hence the relative error is 1. To highlight the fact that there are also regions where the neglected terms are dominating Fig. (2.15) shows the area of the domain for which the relative errors are smaller than a certain threshold value.

For Equation (2.6) only about 60 percent of the whole domain have a relative error smaller than a hundred percent, for Eq. (2.7) this value is just slightly higher with 70 percent. It is remarkable that the approximation is only good (relative errors smaller than 20 percent) for few points of the domain. Fig. (2.15) shows that just about 15 percent of the domain have $e_{rel1} \leq 20\%$ while for $e_{rel2} \leq 20\%$ it is about 20 percent. However these calculations allow no statement about the errors of the solutions of the

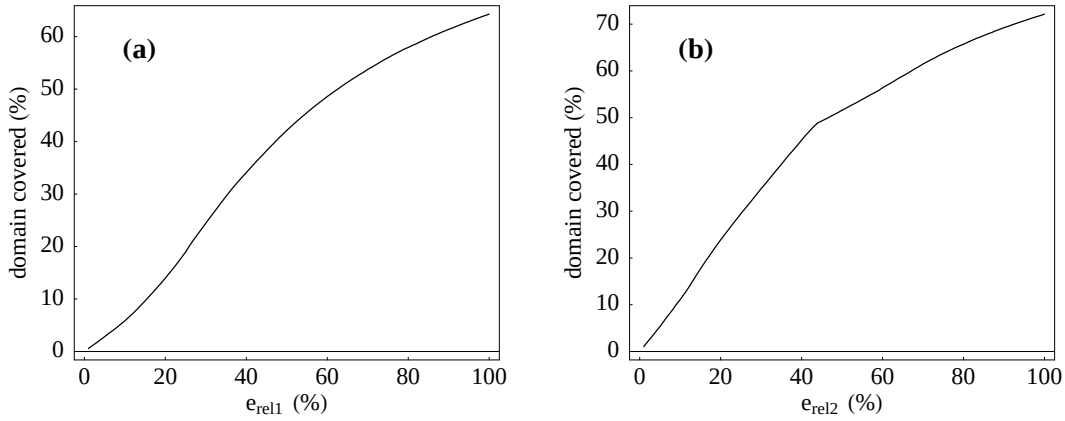

Figure 2.15: Percentage of area of the domain where the relative error is smaller than e_{rel1} plotted versus e_{rel1}, (panel (a)) and the same calculation for e_{rel2}, (panel (b)).

differential equation. To assess this problem one would need to solve Eq.(2.6) and Eq.(2.7) and afterwards compare the results for (u, v, w) directly.

Another hint how to estimate the accuracy of the linear approximation is given by the scale analysis itself. In section (2.1.1) it was shown that the importance of the neglected terms can be investigated by an inspection of the radial variations of Ro_{Ξ} and Ro_{Λ} as well as estimates of S_u and $S_{v'}$. These parameters are naturally depending on the chosen profile for v_{gr} (the details will be discussed later).

Figure (2.16) shows contour plots of the parameters $S_u = u/v_{gr}$ (panel (a)), and $S_{v'} = v'/v_{gr}$ (panel (b)).

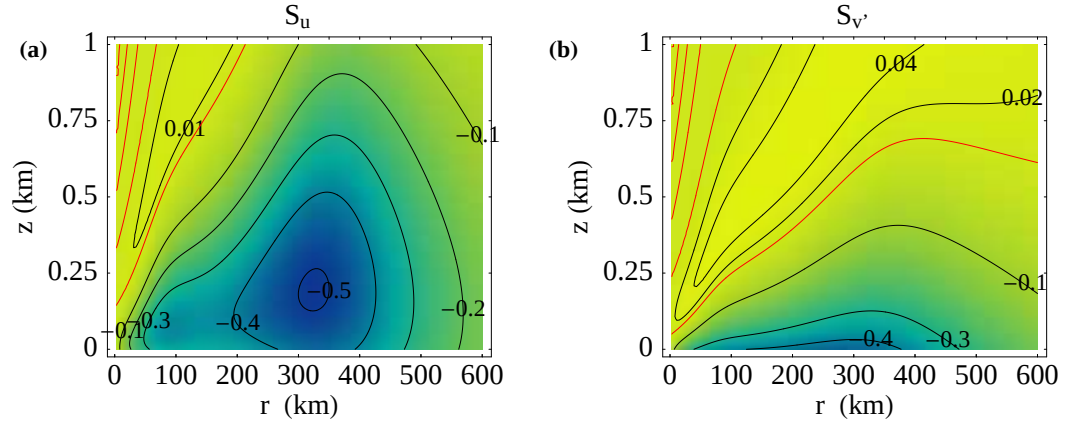

Figure 2.16: Ratio of the radial to the gradient wind $S_u = u/v_{gr}$, panel (a) and ratio of the tangential to the gradient wind $S_{v'} = v'/v_{gr}$, panel (b).

For the weak friction approximation which was studied before, it was assumed that

both, S_u and $S_{v'}$ are small compared to unity. As Fig.(2.16) shows this condition isn't valid for most of the domain for both parameters. S_u and $S_{v'}$ even reach values larger than 0.4 which is not really small compared to unity. It is remarkable that the highest values not only occur in the core region where the approximation naturally may be inaccurate but they spread all over the domain. The global maximum of $|S_u|$ is for example attained at a radius of about 330 km, far out from the radius of maximum winds. The result shown in Fig.(2.16) confirms the findings of the direct comparison of retained terms, t_{r1} and t_{r2}, and neglected terms, t_{n1} and t_{n2} which was shown in Fig.(2.13). It is to say that the assumptions of the weak friction approximation ($S_u \ll 1$ and $S_{v'} \ll 1$) are not valid for vortex profile 3 for all radii. As the scale analysis suggested, also the nonlinear terms could be neglected under the condition that the scales $S_u^2 > S_{v'}^{-1} Ro_\Xi$, $S_{v'} Ro_\Xi$ and $S_{v'} Ro_\Lambda$ are all small compared to unity. To check this, Figure (2.17) shows the radial profiles of the three parameters, evaluated in a height of 100 m for vortex profile 3.

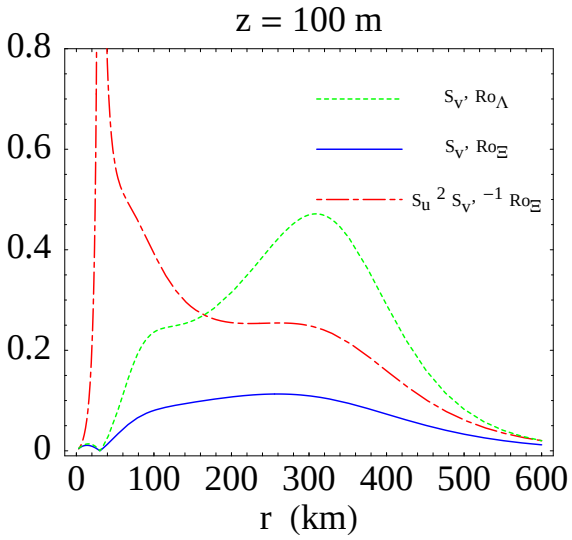

Figure 2.17: Radial profiles of the scales $S_u^2 s_{v'}^{-1} Ro_\Xi$, $S_{v'} Ro_\Xi$ and $S_{v'} Ro_\Lambda$, evaluated in a height of 100 m for vortex profile 3.

Clearly, for vortex profile 3 none of the parameters is very small compared to unity at most of the radii. Hence Fig.(2.17) is a further corroboration of the findings from above: the linear approximation to the boundary layer is inaccurate and does not provide much of an improvement to the classical Ekman layer anywhere near the inner core region of a hurricane. This inaccuracy is due to miscellaneous reasons.
Kepert (2001) stated that the neglect of the vertical advection, which was not supported

by a scale analysis, was the main fact to cause the crucial deviation of the linear model from nonlinear ones. In any case the scale analysis derived before suggests that not only the vertical advection is important. The neglect of radial advection should be almost equally important. To examine this idea further it is possible to calculate the contributions of the radial and vertical advection terms to the terms t_{n1} and t_{n2}. Figure (2.18) shows contour plots of the radial advections $u\frac{\partial u}{\partial r}$ and $u\frac{\partial v'}{\partial r}$, panel (a) and (b) and vertical advections $w\frac{\partial u}{\partial z}$ and $w\frac{\partial v'}{\partial z}$, panel (c) and (d).

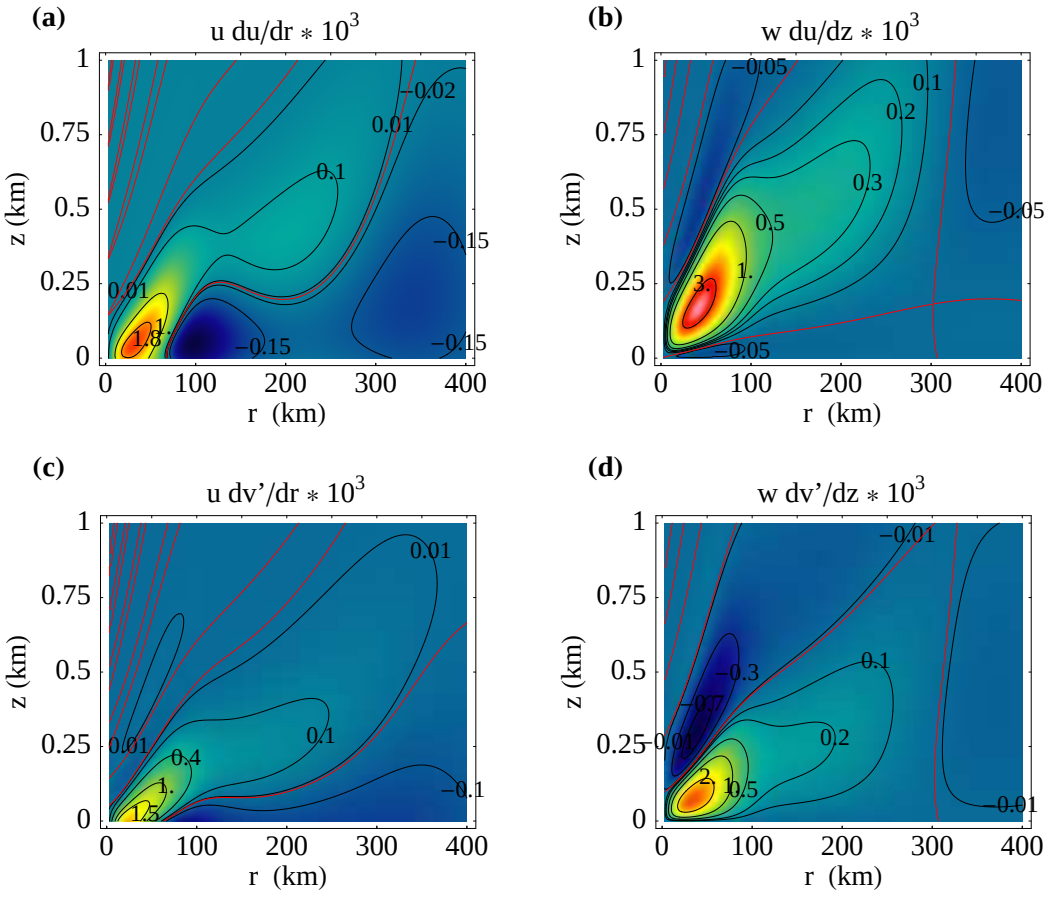

Figure 2.18: Radial advections $u\frac{\partial u}{\partial r}$ and $u\frac{\partial v'}{\partial r}$, panel (a) and (b) and vertical advections $w\frac{\partial u}{\partial z}$ and $w\frac{\partial v'}{\partial z}$, panel (c) and (d).

It is obvious that in both of the terms t_{n1} and t_{n2} the radial advection terms are of the same order of magnitude as the vertical advection terms. To highlight this fact Fig.(2.19) shows the radial variation of the advection terms evaluated at a height of 100 m, where their values are at a maximum.

The maximum values of the vertical advection terms are about twice as large as the

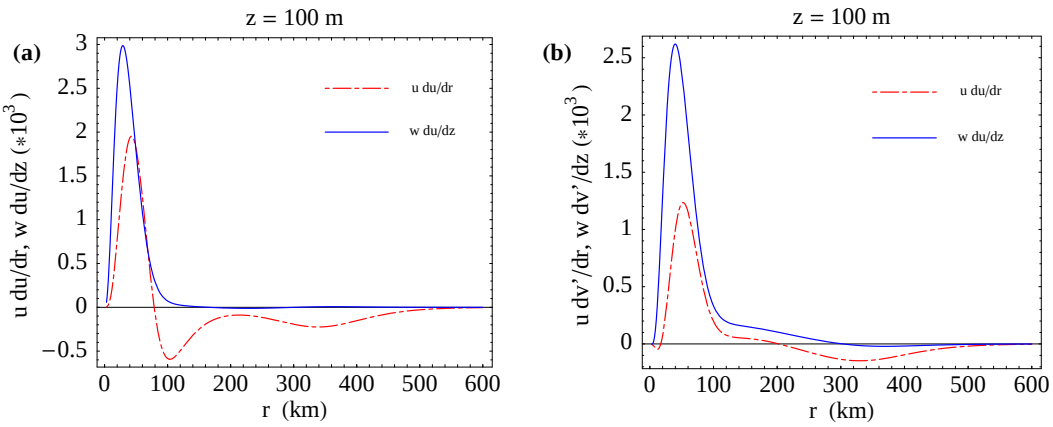

Figure 2.19: Comparison of radial and vertical advection terms in t_{n1}, panel (a) and in t_{n2}, panel (b) evaluated in a height of 100 m, where the values are close to their maximum.

maximum values in the radial terms, but over most of the domain the radial terms are as large as the vertical ones or even larger. This calculation gives additional evidence that the importance of the radial terms is underestimated and the effects of radial advection must not be ignored. However if other wind profiles are used, the results may change as S_u and $S_{v'}$, and thus the quality of the approximation depends crucially on the choice of a profile for v_{gr}.

Figure (2.20) shows a comparison of the neglected terms t_{n1} and t_{n2} for vortex 2 (panel (a) and (b)) and vortex profile 5 (panel (c) and (d)).

As before the absolute values of the neglected terms are in the same range as the terms retained in the analysis but the two vortex profiles show differences. Both t_{n1} and t_{n2} achieve their maximum values of about 4 $\mathrm{m\,s^{-1}}$ in the core region close to the ground level but for vortex 2 the area of high values up to 1 $\mathrm{m\,s^{-1}}$ is much larger covering a range of radii up to 250 km and heights up to 1 km. Both terms t_{n1} and t_{n2} show a pronounced local minimum at a radius of about 300 km from the ground up to heights of about 1 km which is not attained for vortex 5.

Again the accuracy of the approximation for each wind profile may be estimated by comparing the parameters S_u and $S_{v'}$. Figure (2.21) shows a comparison of the parameters S_u and $S_{v'}$ for the five different vortex profiles shown in Fig.(4.12). The calculation for Ro_Ξ and Ro_Λ shown in Fig.(2.2) suggested already that the accuracy of the approximation is highly dependent on the wind profile used. A fact that is highlighted by the profiles shown in Fig.(2.21). It was shown earlier that for vortex

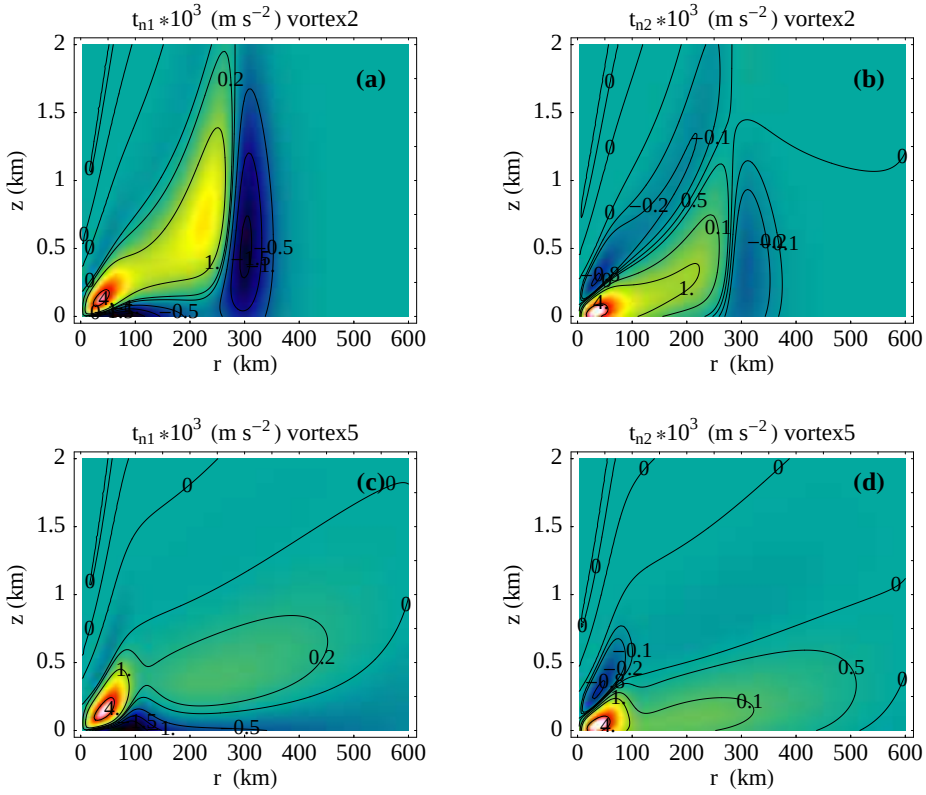

Figure 2.20: Terms t_{n1} and t_{n2} neglected in the approximation for vortex profile 2 (panel (a) and (b)) and vortex profile 5 (panel (c) and (d)).

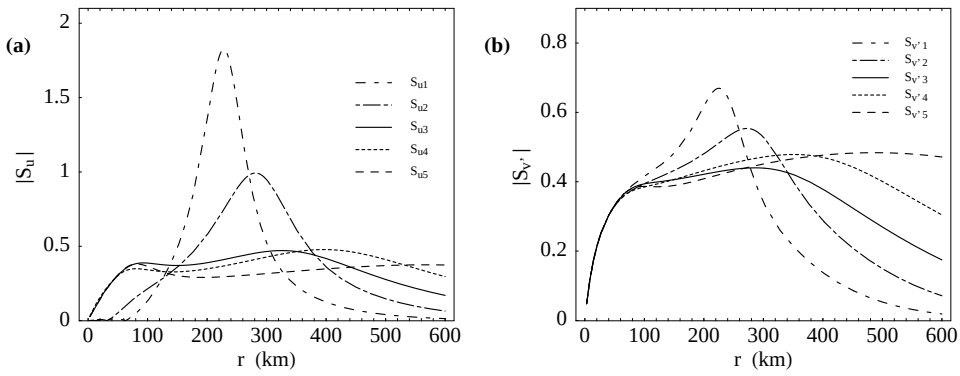

Figure 2.21: Parameters S_u (panel (a)) and $S_{v'}$ (panel (b)) for the five different vortex profiles.

1 the deviation of the parameters Ro_Ξ and Ro_Λ from the assumed value was largest and it was argued that the accuracy was weakest for that profile. This argument was strengthened also by the direct comparison of neglected and retained terms which was shown in Fig.(2.20). Figure (2.21) is the ultimate confirmation of these findings.

S_u and $S_{v'}$ were assumed to be small compared to unity. This is not nearly true for vortex profile 1. Here the maximum value of S_u is 1.9 and therefore almost twice as large as unity. However it is of interest that for vortex profile 1, the value of S_u is smaller than in the case of profiles 3 to 5 for large regions of the domain. In general the results of S_u are more extreme for vortex 1 and 2, which means that the extreme values are significantly higher than in the other cases (vortex 3 and 4 have maxima of about 0.5, which is four times smaller than the maximum value for vortex 1), but for very small and very large radii the curves for vortex 1 and vortex 2 are below the others.

In the case of $S_{v'}$ the differences due to the use of different gradient wind profiles are not as large as in the case of the parameter S_u. The profiles are almost identical inside a radius of about 100 km. In all five cases the maximum of the parameter lies in the range of 0.4 to 0.6. In general it is to say that for all five profiles both S_u and $S_{v'}$ are not even small compared to unity for most of the area of the domain. However, the use of vortex 1 in the linear approximation may be somewhat better for very large and very small radii but it also causes more inaccuracies for radii close to the radius where its maximum values of S_u and $S_{v'}$ are attained. The results for vortex 3, which was used in the control calculation, show that this profile may be the best compromise for use in the linear model.

As it was discussed before the quality of the approximation is also very sensitive to the choice of the Eddy diffusivity K_M. Again for the choice of different values for K_M varying between 5 and 100 $\mathrm{m^2 s^{-1}}$ the neglected and the retained terms are of the same order of magnitude. Figure (2.22) shows how changes in the eddy diffusivity influence the neglected terms t_{n1} and t_{n2}.

The influence of the eddy diffusivity will become even clearer by an inspection of the scale parameters S_u and $S_{v'}$.

Figure (2.23) shows the parameters S_u (panel (a)) and $S_{v'}$ (panel (b)). For the calculation five different values of K_M varying between 5 to 100 $\mathrm{m^2 s^{-1}}$ were used. Fig.(2.23) shows that the values for S_u (panel (a)) and $S_{v'}$ (panel (b)) are decreasing significantly with increasing K_M. While for $K_M = 5$ $\mathrm{m^2 s^{-1}}$ the maxima of S_u and $S_{v'}$ are about 0.5, a value of $K_M = 100$ $\mathrm{m^2 s^{-1}}$ brings the maxima down to 0.3 and 0.2 which is a reduction of about one half. This finding can also be confirmed by an inspection of the radial profiles of the scales $S_u^2 S_{v'}^{-1} Ro_\Xi$, $S_{v'} Ro_\Xi$ and $S_{v'} Ro_\Lambda$. These scales are shown in

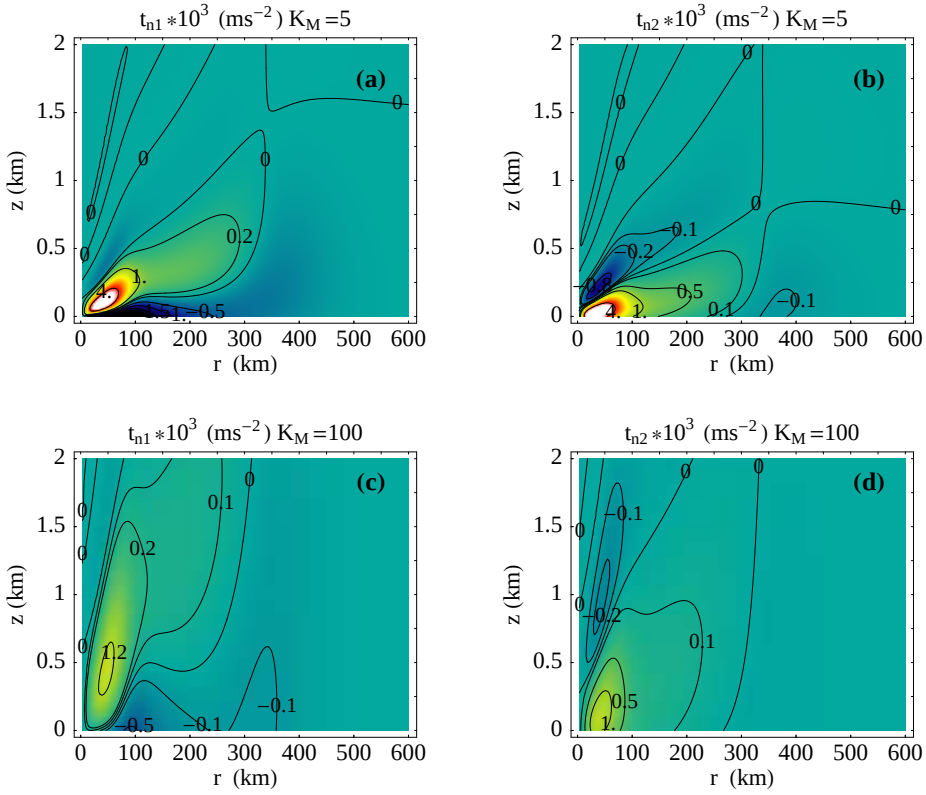

Figure 2.22: Neglected terms t_{n1} and t_{n2} for $K_M = 5$ m^{2}s^{-1} (panel (a) and (b)) and $K_M = 100$ m^{2}s^{-1} (panel (c) and (d)).

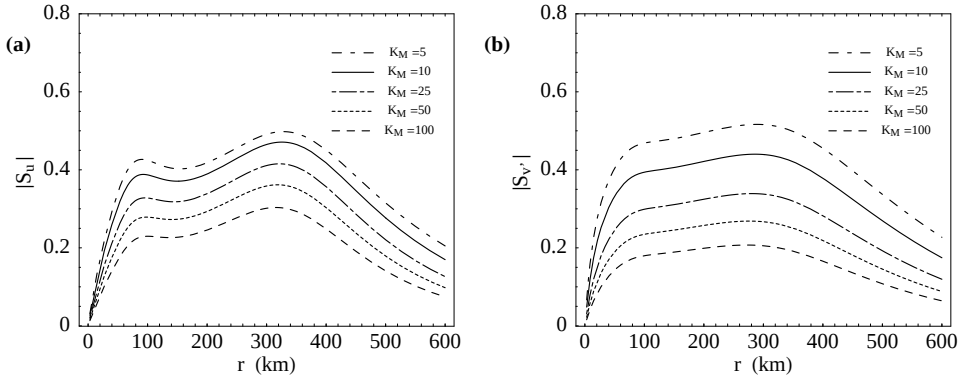

Figure 2.23: Parameters S_u (panel (a)) and $S_{v'}$ (panel (b)) for five different values of K_M varying between 5 to 100 m^{2}s^{-1}.

Figure (2.24) for $K_M = 5$ m^{2}s^{-1}, panel (a), and for $K_M = 100$ m^{2}s^{-1}, panel (b).

For $K_M = 5$ m^{2}s^{-1} the values of the scales exceed those calculated with $K_M = 100$ m^{2}s^{-1} by almost a factor of two. Thus it can be argued that the linear approximation performs better for larger values of Eddy diffusivity K_M.

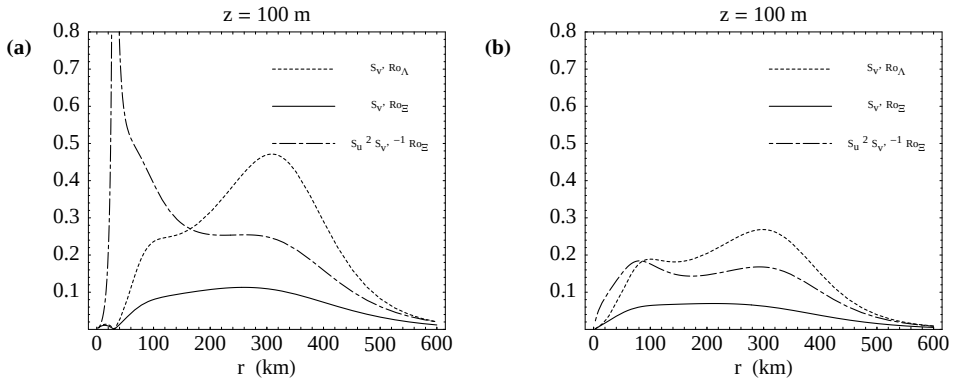

Figure 2.24: Radial profiles of the scales $S_u^2 S_{v'}^{-1} Ro_\Xi$, $S_{v'} Ro_\Xi$ and $S_{v'} Ro_\Lambda$, evaluated in a height of 100 m for $K_M = 5$ m^{2}s^{-1}, panel (a), and for $K_M = 100$ m^{2}s^{-1}, panel (b).

2.4 Discussion of the results

The foregoing analysis points to serious limitations of the linear boundary layer solution when applied to the inner core of hurricanes, even for radii well beyond the radius of maximum gradient wind speed.

However, this is not the only limitation. There is another important point that was not yet discussed. As pointed out by Smith and Vogl (2008) and will be discussed in the next chapter, it is probably incorrect to prescribe the tangential wind speed just above the boundary layer in the inner region, where the flow exits the boundary layer.

Many previous boundary-layer models have taken this approach (e.g. Smith 1968, Ooyama 1969, Leslie and Smith 1970, Bode and Smith 1975, Shapiro 1983, Kepert 2001, Smith 2003), but the consequences thereof have not been investigated or discussed in detail. Presumably with this limitation in mind, Kepert and Wang (2001) used a boundary condition that constrains the vertical gradient of the radial and tangential velocity components to be zero at the top of their computational domain. Nevertheless, because the radial motion at this boundary turns out to be close to zero (see their Fig. 2), the tangential wind speed must be close to the gradient wind at this boundary.

One has to concur with Kepert and Wang (2001) that it is more reasonable to suppose that boundary-layer air carries its momentum with it as it ascends out of the boundary layer, because this boundary is an *outflow boundary* of the problem.

Unfortunately, it is not possible to accommodate a zero vertical-gradient constraint in the analytic solution of the linear model. Since the radius at which the vertical motion

reverses sign at the top of the boundary layer occurs relatively far from the vortex center in the linear model, the inability to apply a zero vertical-gradient constraint further limits the usefulness of the model when applied to hurricanes. These remarks presumably apply to the extension of the linear model to nonaxisymmetric flow worked out by Kepert (2001).

It will be shown in the next capter that the same limitation does not exist in a slab boundary layer model. The reason is that boundary layer wind and gradient wind are not the same at the top of the boundary layer, even though the radial pressure gradient in the boundary layer is the same as that above (see Smith and Montgomery (2008) for a scale analysis for the slab boundary layer).

For the calculations shown here it was assumed that the turbulent diffusivity is constant with height and radius. A range of different constant values for the parameter K_M was investigated.

With the variation of the results caused by a change in K_M in mind it is to say that a constant eddy diffusivity is adequate for present purposes when combined with a bulk drag formulation of the surface layer (see e.g. Leslie and Smith 1970, Bode and Smith 1975). Keeping K_M constant with radius is potentially more serious as one would certainly expect turbulence levels to rise as the wind speeds increase significantly with decreasing radius. It was shown that it is possible to derive a K_M which is a function of the radius when the existence of a surface layer is postulated. Unfortunately observations provide little guidance on the magnitude of this increase. Thus the functional dependence of K_M may not be estimated against measurements.

In view of the result that the linear boundary-layer theory breaks down in the region of strong winds, it is questionably whether one would learn much more from calculations in which such a variation of K_M is postulated. Nevertheless, the scaling analysis in section 2.1 suggests that any increase will be reflected in a commensurate increase in the boundary layer depth above that predicted assuming a radially constant K_M.

Chapter 3

A simple slab model of the hurricane boundary layer

In the foregoing chapter a type of models of the hurricane boundary layer was discussed which could be subsummed under the term "continuous model". In these models the vertical structure as well as the radial variation were considered. The studies focussed exclusively on the dynamical constraints of the boundary layer, there was no representation of thermodynamic aspects.

The importance of the thermodynamical constraint was first recognized by Emanuel (1986). He proposed a simple axisymmetric model for a hurricane. In a slab model the equations are vertically integrated (which means that they are averaged over the whole depth of the boundary layer) and uniform profiles of the radial and tangential wind are assumed. The representation of the thermodynamic features in the hurricane boundary layer was a key feature in Emanuel (1986).

In his hurricane model, the tangential wind field above the boundary layer is assumed to be in thermal wind balance and air parcels flowing upwards and outwards into the upper troposphere.

These air parcels are assumed to conserve their absolute angular momentum and moist entropy. The model is closed by a simple, uniform-depth slab formulation for the boundary layer. Emanuel used this simple slab model to determine a functional relationship between the absolute angular momentum and moist entropy of air parcels that are moving out of the boundary layer.

In this chapter a slightly more sophisticated, axisymmetric, slab model than that employed by Emanuel *op. cit.* will be derived, following Smith (2003) and Smith and Vogl (2008) (see Fig.(3.1)). In the literature there is no other model of the hurricane boundary layer which is focussing not only on the dynamical but also on the thermodynamical processes.

This axisymmetric slab model is allowing for the effects of mean subsidence at large radii and for the effects of shallow convection. These effects have an important control on the radial variation of thermodynamic quantities. It turns out that shallow convection plays an important role as without a representation of mixing by shallow convection, the boundary layer saturates at an unrealistically-large radius.

The model derived below is a steady, moist, axisymmetric, slab model of constant depth, but the tangential wind speed at the top of the layer is prescribed as a function of radius. With these assumptions the boundary layer equations reduce to a set of coupled ordinary differential equations for the radial variation of the boundary-layer wind, temperature and moisture fields. It is possible to obtain high-resolution solutions of these equations by integrating inwards from some large radius. At this starting radius it is assumed that geostrophic balance and convective-radiative equilibrium conditions are dominant in the boundary layer. The model can be used to explore various aspects of the boundary layer including the influence of vortex size and structure, the influence of the chosen boundary layer depth itself, including radially varying boundary layer depth. It is also possible to discuss the influence of the parameter setup, i.e. the sensitivity of the slab model to changes in the drag or the eddy diffusivity. A particular advantage of this slab model is that it is not only the radial distribution of key dynamic quantities that may be explored but also that of basic thermodynamic quantities.

3.1 Summary of the model

Boundary layer equations

The boundary layer of a steady axisymmetric hurricane-like vortex on an f-plane is considered. This means that the spherical Earth is assumed to be a plane normal to the zenithal component of the Earth's rotation. The rotation rate f is assumed to be constant on the plane. This assumption turns out to be accurate enough when

atmospheric or oceanic motions are described for which the time scales are smaller than or comparable to $1/f$.

The boundary layer is assumed to have uniform depth δ and constant density. In a cylindrical coordinate system (r, ϕ, z), the boundary layer equations for a hurricane-like vortex in a homogeneous fluid can be written as

$$\frac{1}{r}\frac{\partial}{\partial r}(ru^2) + \frac{\partial}{\partial z}(uw) + \frac{v_{gr}^2 - v^2}{r} + f(v_{gr} - v) = \frac{\partial}{\partial z}\left(K_M \frac{\partial u}{\partial z}\right), \tag{3.1}$$

$$\frac{1}{r^2}\frac{\partial}{\partial r}(r^2 uv) + \frac{\partial}{\partial z}(vw) + fu = \frac{\partial}{\partial z}\left(K_M \frac{\partial v}{\partial z}\right). \tag{3.2}$$

The continuity equation takes the form

$$\frac{\partial}{\partial r}(ru) + \frac{\partial}{\partial z}(rw) = 0. \tag{3.3}$$

In these equations the wind vector is $\vec{u} = (u, v, w)$ so that u denotes the radial, v the tangential component of the flow and w stands for the vertical wind speed. $v_{gr}(r)$ is the tangential wind speed at the top of the boundary layer.

If χ denotes a scalar quantity, here dry static energy or specific humidity, there is an additional equation for these thermodynamic quantities which is of the form

$$\frac{1}{r}\frac{\partial}{\partial r}(ru\chi) + \frac{\partial}{\partial z}(w\chi) = \frac{\partial}{\partial z}\left(K_M \frac{\partial \chi}{\partial z}\right). \tag{3.4}$$

As before f denotes the Coriolis parameter, K_M is an Eddy diffusivity. These equations can now be integrated vertically from the ground at $z = 0$ to the top of the boundary layer $z = \delta$. First for simplicity it is assumed that δ is a constant and hence not depending on the radius r. Integration with respect to z then gives

$$\frac{d}{dr}\left(r\int_0^\delta u^2 dz\right) + [ruw]|_{z=\delta} + \int_0^\delta (v_{gr}^2 - v^2)dz + rf\int_0^\delta (v_{gr} - v)dz = -K_M r \left.\frac{\partial u}{\partial z}\right|_{z=0}, \tag{3.5}$$

$$\frac{d}{dr}\left(r^2\int_0^\delta uv dz\right) + [r^2 vw]\big|_{z=\delta} + fr^2\int_0^\delta u dz = -K_M r^2 \left.\frac{\partial v}{\partial z}\right|_{z=0}, \tag{3.6}$$

$$\frac{d}{dr}\left(r\int_0^\delta u\chi dz\right) + [rw\chi]|_{z=\delta} = -K_M r \left.\frac{\partial \chi}{\partial z}\right|_{z=0}, \tag{3.7}$$

$$\frac{d}{dr}\left(\int_0^\delta r u dz\right) + [rw]|_{z=\delta} = 0. \tag{3.8}$$

Now it is

$$[ruw]|_{z=\delta} = ru_b w_{\delta_+} + ru_{gr} w_{\delta_-}$$

and u_{gr} denotes the radial component of the flow in the region above the boundary layer. It is assumed that u_{gr} is zero so that there is just a tangential component of the flow for $z > \delta$. The flow inside the boundary layer for $z < \delta$ is denoted as $\vec{u_b} = (u_b, v_b)$. For the vertical motion it is

$$w_{\delta_+} = \frac{1}{2}(w_\delta + |w_\delta|)$$

and

$$w_{\delta_-} = \frac{1}{2}(w_\delta - |w_\delta|).$$

Note that it is $w_{\delta_+} = w_\delta$ if w_δ is positive and zero otherwise and $w_{\delta_-} = w_\delta$ if w_δ is negative and zero otherwise. As before at the surface a bulk drag law may be applied. It is assumed that

$$K_M \left.\frac{\partial \vec{u_b}}{\partial z}\right|_{z=0} = C_D \, |\vec{u_b}| \, \vec{u_b}. \tag{3.9}$$

As before C_D is a drag coefficient which may be chosen as a constant or as a radially varying parameter. A similiar law is valid for χ:

$$K_M \left.\frac{\partial \chi}{\partial z}\right|_{z=0} = C_\chi \, |\vec{u_b}| \, (\chi_b - \chi_s). \tag{3.10}$$

Here χ_b denotes the value of χ inside the boundary layer while χ_s represents that at the sea surface. The expression χ_{δ_+} denotes the value of χ just above the boundary layer.

If χ stands for the dry static energy, the value of χ_s can be calculated using the sea surface temperature, and if χ represents the moisture, it is the saturation specific humidity at this temperature. Now in the Equations (3.5) - (3.8) the integrals can be explicitely solved, giving:

$$\delta \frac{d}{dr}(ru_b^2) = -w_{\delta_+} r u_b - \delta(v_{gr}^2 - v_b^2) - \delta r f (v_{gr} - v_b) - C_D r \sqrt{u_b^2 + v_b^2} u_b, \tag{3.11}$$

$$\delta \frac{d}{dr}(ru_b rv_b) = -r w_{\delta_+} r v_b - r w_{\delta_-} r v_{gr} - \delta r^2 f u_b - C_D r^2 \sqrt{u_b^2 + v_b^2} v_b, \tag{3.12}$$

$$\delta \frac{d}{dr}(ru_b \chi_b) = -w_{\delta_+} r \chi_b - r w_{\delta_-} \chi_{\delta_+} + C_\chi r \sqrt{u_b^2 + v_b^2}(\chi_s - \chi_b), \tag{3.13}$$

and

$$\delta \frac{d}{dr}(ru_b) = -r w_\delta. \tag{3.14}$$

These equations can be divided by δ to give

$$\frac{d}{dr}(ru_b^2) = -\frac{w_{\delta_+}}{\delta} ru_b - (v_{gr}^2 - v_b^2) - rf(v_{gr} - v_b) - \frac{C_D}{\delta} r\sqrt{u_b^2 + v_b^2}u_b, \tag{3.15}$$

$$\frac{d}{dr}(ru_b rv_b) = -r\frac{w_{\delta_+}}{\delta} rv_b - r\frac{w_{\delta_-}}{\delta} rv_{gr} - r^2 fu_b - \frac{C_D}{\delta} r^2\sqrt{u_b^2 + v_b^2}v_b, \tag{3.16}$$

$$\frac{d}{dr}(ru_b\chi_b) = -\frac{w_{\delta_+}}{\delta} r\chi_b - r\frac{w_{\delta_-}}{\delta}\chi_{\delta_+} + \frac{C_\chi}{\delta} r\sqrt{u_b^2 + v_b^2}(\chi_s - \chi_b), \tag{3.17}$$

and

$$\frac{d}{dr}(ru_b) = -r\frac{w_\delta}{\delta}. \tag{3.18}$$

If η stands for any dependent variable, u_b, v_b or χ_b, it is

$$\frac{d}{dr}(ru_b\eta) = ru_b\frac{d\eta}{dr} + \eta\frac{d}{dr}(ru_b) = ru_b\frac{d\eta}{dr} - \frac{w_\delta}{\delta} r\eta. \tag{3.19}$$

Using this identity the vertically-integrated equations for radial momentum, azimuthal momentum, heat or moisture, and continuity can be written in the form:

$$u_b\frac{du_b}{dr} = u_b\frac{w_{\delta_-}}{\delta} - \frac{(v_{gr}^2 - v_b^2)}{r} - f(v_{gr} - v_b) - \frac{C_D}{\delta}\sqrt{(u_b^2 + v_b^2)}u_b - \frac{\overline{(u'w')}_\delta}{\delta}, \tag{3.20}$$

$$u_b\frac{dv_b}{dr} = \frac{w_{\delta_-}}{\delta}(v_b - v_{gr}) - \left(\frac{v_b}{r} + f\right)u_b - \frac{C_D}{\delta}\sqrt{(u_b^2 + v_b^2)}v_b - \frac{\overline{(v'w')}_\delta}{\delta}, \tag{3.21}$$

$$u_b\frac{d\chi_b}{dr} = \frac{w_{\delta_-}}{\delta}(\chi_b - \chi_{\delta+}) + \frac{C_\chi}{\delta}\sqrt{(u_b^2 + v_b^2)}(\chi_s - \chi_b) - \frac{\overline{(\chi'w')}_\delta}{\delta} - \dot{\chi}_b, \tag{3.22}$$

and

$$\frac{du_b}{dr} = -\frac{u_b}{r} - \frac{w_\delta}{\delta}. \tag{3.23}$$

In this equations C_χ is the surface transfer coefficient for χ_b, $\chi_{\delta+}$ is the value of χ just above the boundary layer, χ_s is the value of χ at the sea surface. The term $\dot{\chi}_b$ denotes any source of χ and the terms $\overline{(u'w')}_\delta$, $\overline{(v'w')}_\delta$, $\overline{(\chi'w')}_\delta$ represent turbulent fluxes at the top of the boundary layer.

If χ represents the dry static energy it is $\chi_s = c_pT_s$, where T_s denotes the temperature at the sea surface and c_p is the specific heat of air at a constant pressure. Additionally $\dot{\chi}_b$ is the sum of the terms $-c_p\dot{T}_b$ and $C_D(u_b^2 + v_b^2)^{3/2}$. Here $\dot{T}_b$ denotes the radiative cooling rate and $C_D(u_b^2 + v_b^2)^{3/2}$ has to be interpreted as the rate of generation of

enthalpy by frictional dissipation. Smith (2003) did not include the dissipation term and just was taking into account the radiative cooling rate. However it was shown by Bister and Emanuel (1998) that the dissipation term is also significant especially when it is coming to wind speeds of hurricane strength. If χ represents the moisture χ_s is the saturation specific humidity at the temperature T_s. In this case $\dot{\chi_b} = 0$.

Note that in this calculation condensation with latent heat release in the boundary layer is supressed. However it is checked that the boundary layer does not saturate, although the cloud base will become lower as the boundary layer humidity increases. As the quantities u_b, v_b and χ_b are vertically averaged, they are only functions of the radius and not of the height z. As it was discussed before $w_{\delta-}$ is nonzero only when $w_\delta < 0$. In this case it is equal to w_δ. Thus the terms that are involving $w_{\delta-}$ are representing transport processes in which the properties of the atmosphere above the boundary layer are transported downwards.

Representation of the drag coefficient

For the representation of the drag coefficient there are different possibilities. The most simple case would be to take an appropriate constant value as done for example by Kepert (2001). A constant value for C_D was also used in the calculations for the linear models discussed before. However, it was also shown there that a radially varying drag coefficient may cause slight changes in the results. Other possibilities would be to follow Shapiro (1983), as it was done for example by Smith (2003). There C_D was evaluated from the formula $C_D = C_{D0} + C_{D1}|\mathbf{u_b}|$, where $C_{D0} = 1.1 \times 10^{-3}$, $C_{D1} = 4 \times 10^{-5}$ and $\mathbf{u_b} = (u_b, v_b, 0)$. That means that C_D is linearly depending on the wind speed. He assumed also that $C_\chi = C_D$.

In the past good measurements of the exchange coefficients in a hurricane were rare. The extreme wind speeds obtained in the hurricane boundary layer make explorations for example by reconaissance flights or dropsondes quite difficult. Sea spray, for example, causes damage to the motors of the airplanes due to the salt which is entruding. However the technical possibilities are improving and recently Black *et al.* (2006) presented new aircraft measurements of the exchange coefficients at wind speeds up to 30 m s^{-1}. These measurements suggest that C_D no longer increases for wind speeds higher than about 20 m s^{-1}, although there is considerable scatter in the data. Including the

most recent results, for the calculations in later sections, values of $C_{D0} = 0.7 \times 10^{-3}$ and $C_{D1} = 6.5 \times 10^{-5}$ for wind speeds less than 20 m s^{-1} and $C_D = 2.0 \times 10^{-3}$, a constant, for larger wind speeds are used. These values are based on the interpretation of Black *et al.*'s Fig.(5). For C_χ simply a constant value equal to 1.1×10^{-3}, based on their Fig.(6) is included into the calculations.

To find u_b, v_b, and χ_b as functions of r an expression for the vertical velocity has to be derived first. For that purpose it is started with Equation (3.20) and substituting Equation (3.23) into it. Then an expression for w_δ follows immediately:

$$w_\delta = \frac{\delta}{1+\alpha}\left[\frac{1}{u_b}\left(\frac{(v_{gr}^2 - v_b^2)}{r} + f(v_{gr} - v_b) + \frac{C_D}{\delta}\sqrt{(u_b^2 + v_b^2)}u_b\right) - \frac{u_b}{r}\right], \qquad (3.24)$$

where α is zero if the expression in square brackets is negative and unity if it is positive. Now Eqs.(3.21) - (3.23), together with this expression for w_δ, form a system that may be integrated radially inwards from some large starting radius R to find u_b, v_b, and χ_b as functions of r. The values of these quantities at $r = R$ have to be given. The way how to calculate the starting values at the initial conditions is discussed in detail later. If χ is the specific humidity the surface moisture flux has to be calculated. Therefore it is necessary to know the saturation specific humidity q_{ss} at the ground level which is depending on the pressure at the surface. The surface pressure is not prescribed. It has to be calculated together with all other quantities. To do that the gradient wind equation

$$\frac{dp}{dr} = \rho\left(\frac{v_{gr}^2}{r} + f v_{gr}\right) \qquad (3.25)$$

is integrated.

Representation of shallow convection

In regions over the tropical oceans there are widespread areas of large-scale subsidence. Convection is an omnipresent feature in the boundary layer there. An important aspect of this convective boundary layer is, that shallow convection is occuring nearly everywhere. The regions where hurricanes occur are also part of this area. Thus shallow convective processes have to be taken into account when the boundary layer of hurricanes is studied. The shallow convection plays an important role in the exchange of heat and moisture between the subcloud layer, the layer which is modelled by the

simple slab model discussed in this section, and the cloudy layer above.

The thermodynamic variables represented by $\chi_{\delta+}$ above the boundary layer are not predicted here. So for simplicity a constant value for the mass flux of shallow convection, w_{sc} is chosen and added to $w_{\delta-}$ in Eqs.(3.20) - (3.22). Note that it is also added even if $w_{\delta-} = 0$.

This is equivalent to representing the flux terms $\overline{\eta' w'}_\delta$ in these equations by $w_{sc}(\eta_+ - \eta_b)$, where η is one of the dependent variables u, v, χ and the subscript '+' denotes a value just above the boundary layer. However, w_δ in Eq.(3.23) is left unchanged. This is due to the fact that there is no net exchange of mass between the cloud and the subcloud layers caused by shallow convection. The value for w_{sc} is chosen to ensure that the thermodynamic profile at large radius is close to radiative-convective equilibrium as explained in the next subsection.

Starting conditions at large radius

It is assumed that at the starting radius $r = R$, far from the axis of rotation, the flow above the boundary layer is steady and in geostrophic balance.

Alternatively it would be possible to assume a linearized form of the full equations.

$$-\xi_{gr} v_b' = -\frac{C_D}{\delta}\sqrt{(u_b^2 + v_b^2)}u_b, \tag{3.26}$$

$$\zeta_{a_{gr}} u_b = -\frac{C_D}{\delta}\sqrt{(u_b^2 + v_b^2)}v_b, \tag{3.27}$$

where $v_b' = v_b - v_{gr}$ and ξ_{gr} and $\zeta_{a_{gr}}$ are given by

$$\xi_{gr} = \frac{2v_{gr}}{r} + f$$

and

$$\zeta_{a_{gr}} = \frac{1}{r}\left(\frac{d}{dr}(rv_{gr})\right) + f = \frac{d}{dr}v_{gr} + \frac{v_{gr}}{r} + f.$$

If one defines now $u = u_b/v_{gr}$, $v = v_b/v_{gr}$, Eqs.(3.26) and (3.27) may be written as

$$-\xi v_{gr}(v-1) = -\frac{C_D}{\delta}v_{gr}^2\sqrt{(u^2+v^2)}u, \tag{3.28}$$

$$\zeta_a v_{gr} u = -\frac{C_D}{\delta}v_{gr}^2\sqrt{(u^2+v^2)}v. \tag{3.29}$$

Introducing the parameters $b = \xi_{gr}/\zeta_{a_{gr}}$ and $c = \zeta_{a_{gr}}\delta/(C_D v_{gr})$ to the equations yields

$$-bc(v-1) = -\sqrt{(u^2+v^2)}u, \tag{3.30}$$

$$cu = -\sqrt{(u^2+v^2)}v. \tag{3.31}$$

Dividing the first of these equations (3.30) by the second (3.31) gives the relation

$$u^2 = bv(1-v). \tag{3.32}$$

Now it is possible to derive an equation for v only. First squaring Eq.(3.30) and using Eq.(3.32) leads to the algebraic equation

$$v^2\left[b(1-v)+v\right] - bc^2(1-v) = 0. \tag{3.33}$$

This can be solved for v numerically and u can be calculated from Eq.(3.32). The vertical velocity w is then obtained by integrating the continuity equation.

Both possibilities to calculate the initial values, the linear approach or the assumption of geostrophic balance, are possible and it is seen that there is not much of a difference between both. For the following calculations the assumption of geostrophic balance is used to calculate the initial values.

If $v_{gr}(R)$ denotes the tangential wind at the starting radius R far from the storm center and C_D is equal to $C_{D0} + C_{D1}v_{gr}(R)$, the tangential and the radial wind speed in the boundary layer v_b and u_b satisfy the equations

$$\begin{aligned} f(v_{gr}-v_b) &= u_b\frac{w_{\delta_-}+w_{sc}}{\delta} - \frac{C_D}{\delta}\sqrt{(u_b^2+v_b^2)}u_b, & (3.34)\\ fu_b &= \frac{w_{\delta_-}+w_{sc}}{\delta}(v_b-v_{gr}) - \frac{C_D}{\delta}\sqrt{(u_b^2+v_b^2)}v_b. & (3.35) \end{aligned}$$

Now a first approximation to the solution is obtained analytically by neglecting momentum transport from above. In the equations this is realized by setting the first two terms on the right-hand-side of Eqs.(3.34) and (3.35) to zero. This leads to the equations

$$\begin{aligned} f(v_{gr}-v_b) &= -\frac{C_D}{\delta}\sqrt{(u_b^2+v_b^2)}u_b, & (3.36)\\ fu_b &= -\frac{C_D}{\delta}\sqrt{(u_b^2+v_b^2)}v_b, & (3.37) \end{aligned}$$

and a first guess for $u_b(R)$ and $v_b(R)$ is obtained. Now it is possible to calculate an expression for the vertical velocity $w_{\delta_-}(R)$ at the starting radius $r = R$ using the continuity equation (3.23). Then it follows

$$w_{\delta_-}(R) = -\delta\left(\frac{du_b}{dr} + \frac{u_b}{r}\right) = -\frac{\delta}{r}\frac{d}{dr}(ru_b). \tag{3.38}$$

This approximate solution is used as a first guess in an iteration procedure for w_{sc} that ensures zero moisture tendency at $r = R$. From the sea surface moist air is transported into the boundary layer so that there is a source of moisture at the ground level. On the other hand moist air is transported upwards and is leaving the boundary layer through the top, where it is replaced by drier air parcels from the atmosphere above. If there is assumed a zero moisture tendency this rate of moisture gain from the sea surface must be balanced by the loss through the top of the boundary layer and its replacement by dry air. This balance is expressed by the equation

$$C_\chi\sqrt{(u_b^2 + v_b^2)}(q_s - q_b) = (w_{sc} + w_{\delta_-}(R))(q_b - q_{\delta_+}). \tag{3.39}$$

If C_χ, q_s, q_b and q_{δ_+} are given and $w_{\delta_-}(R)$ is evaluated from Eq.(3.38), this is an equation for w_{sc}. When $w_{\delta_-}(R)$ and w_{sc} have been determined, Eqs.(3.34) and (3.35) are solved again, now using the values of w_{δ_-} and w_{sc} to find new values of u_b and v_b. Then the whole procedure is repeated until stable values are obtained for w_{δ_-} and w_{sc}. Once w_{δ_-} and w_{sc} are determined the representation of the drag may be refined using now $C_D = C_{D0} + C_{D1}\sqrt{(u_b^2 + v_b^2)}$. Then Eqs.(3.34) and (3.35) are used again to find values for u_b and v_b and the complete iteration process is repeated until stable values are obtained for all quantities, u_b, v_b, $w_{\delta_-}(R)$, w_{sc} and C_D.

As mentioned before for the iteration, the values of the sea surface temperature together with the specific humidities in the boundary layer, q_b, and just above the boundary layer, $q_{\delta+}$, have to be known at $r = R$. The sea surface temperature, T_s, and surface pressure, p_s, are used to determine the saturation specific humidity at the surface. Once the final value for w_{sc} is obtained, the temperature just above the boundary layer, $T_{\delta+}$, is calculated. This is done in a way so that for a specified radiative cooling rate and air temperature just above the surface, T_{as}, the sensible heat fluxes are in equilibrium at the starting radius $r = R$. Let $T_{\delta-}$ denote the temperature just below the boundary layer top.

The assumption of equilibrium leads to an equation for the difference $T_{\delta_+} - T_{\delta_-}$ between the temperature just above and just below the boundary layer of the form

$$T_{\delta_+} - T_{\delta_-} = \frac{1}{w_{sc}} \left[\frac{\dot{R}_b \delta}{c_p} - C_\chi (u_b^2 + v_b^2)^{1/2} (T_s - T_{as}) - \frac{C_D}{c_p} (u_b^2 + v_b^2)^{3/2} \right]. \qquad (3.40)$$

The temperature structure in the boundary layer including both T_b and T_{δ_-} is determined on the assumption that the dry static energy is uniform across the boundary layer. The last term in square brackets is the dissipative heating. This is included for completeness although it is small compared with the other terms at $r = R$.

Fig.(3.1) summarizes again the complete setup of the slab model as discussed above.

3.1.1 Comparison with S03

As mentioned before the slab boundary model described here is similiar to the one developed by Smith (2003). The revisited version discussed here fixed an error in the Runge-Kutta algorithm for the integration of the boundary layer equations and introduced some new features as a new convective equilibrium scheme or exchange coefficients evaluated from the most recent measurements. For completeness a comparison of the revised version and the model represented by Smith (2003) was carried out. For this calculation the same parameters as in the control calculation described by Smith (2003) in his section 6 were used. Including his calculations for the initial equilibrium state and his representation of the exchange coefficients. For the comparison only the dynamical fields are considered. The boundary layer depth is radially constant with a value of 550 m and w_{sc} is -2.2 cm s^{-1}.

Figure (3.2) shows a comparison of the radial and tangential wind components u_b and v_b and the total wind speed (denoted by vv) in the boundary layer in the control calculation (panel (a)) and that in Smith (2003) (panel (b)). It shows also the tangential wind speed v_{gr} at the top of the boundary layer.

From Fig.(3.2) it is clear that for that setup of parameters, there are significant quantitative differences in the corrected calculations. The tangential wind speed in the boundary layer is mostly lower beyond the radius r_m (the radius of maximum tangential wind speed above the boundary layer), but increases steeply as r approaches r_m. Inside a radius of 41.5 km it is supergradient and exceeds the maximum v_{gr} by 8 m s^{-1} at the radius where the solution breaks down. The fact that supergradient winds are obtained is an important difference between the both calculations.

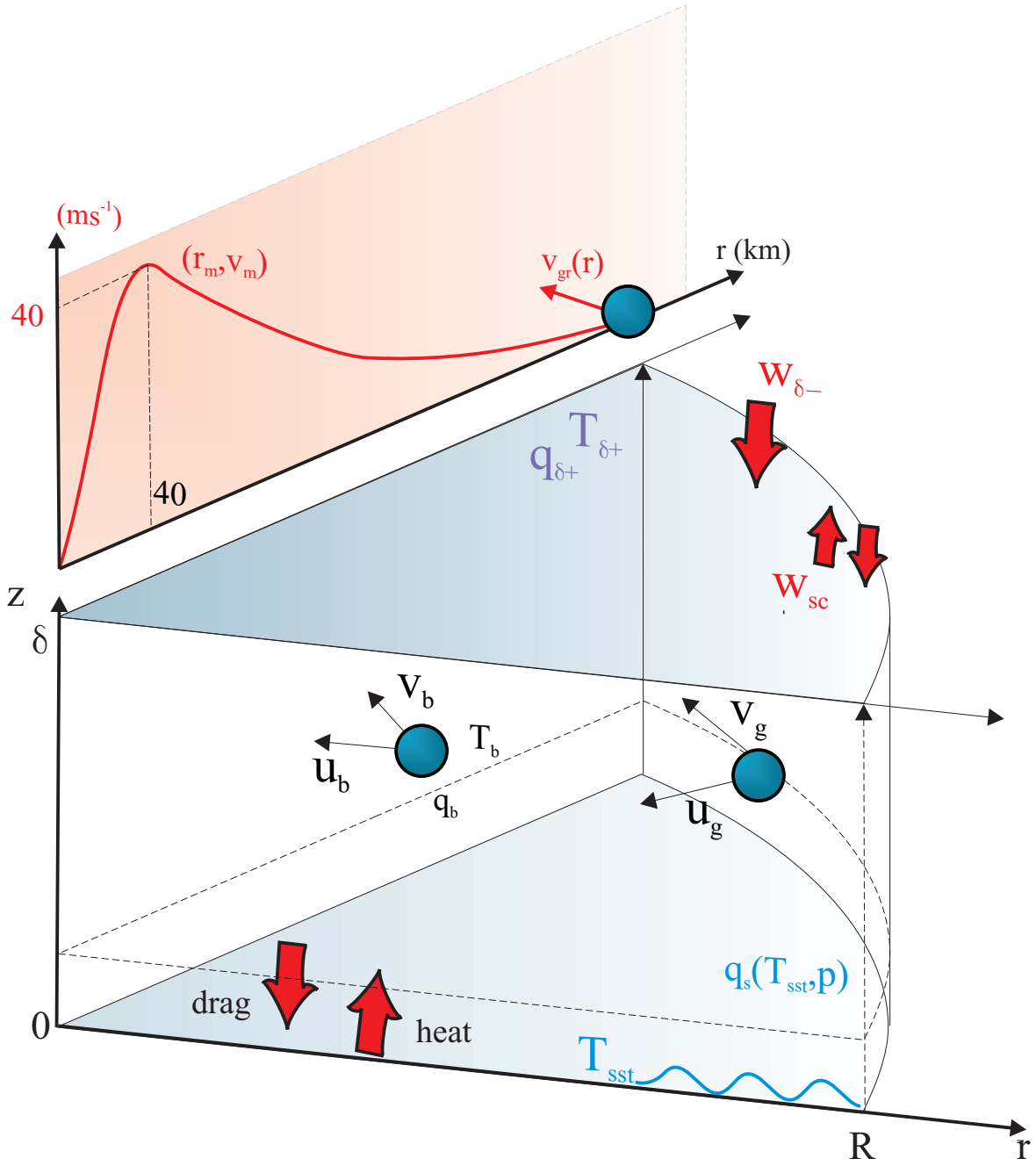

Figure 3.1: Schematic sketch of the slab boundary layer model. The values of the radial and tangential flow are denoted by (u_b, v_b) if it is inside the boundary layer and by (u_g, v_g) if the initial values of that quantities are referred to. The red curve at the top indicates the profile of the gradient wind v_{gr} which is imposed at the top of the boundary layer.

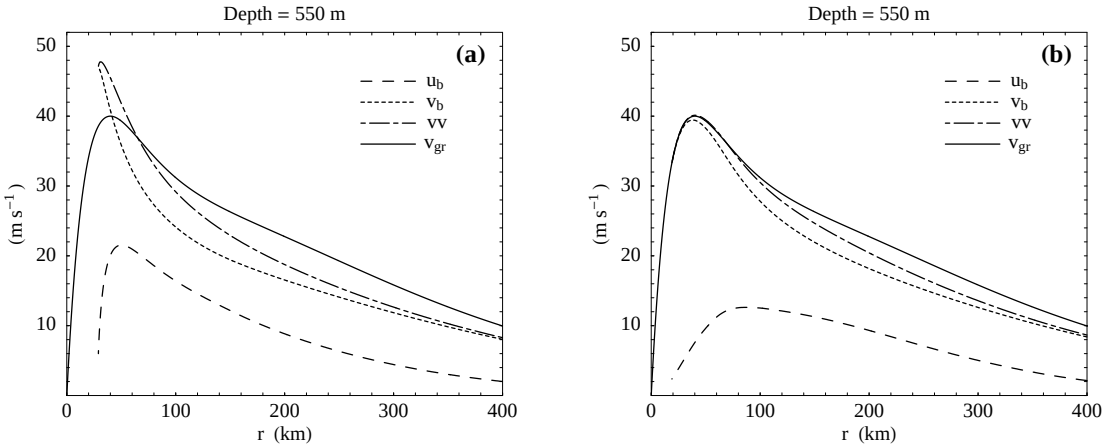

Figure 3.2: Comparison of radial profiles of radial (u_b) and tangential (v_b) wind components and the total wind speed vv in the boundary layer as well as the tangential wind speed above the boundary layer (v_{gr}) for (a) the new calculation and (b) the corresponding calculation in Smith (2003). The boundary layer depth, δ, is 550 m.

The radial wind speed is about twice as large as that in Smith (2003). It reaches its maximum at about 50 km ($1.25r_m$), compared to a little more than 80 km ($2r_m$). However, it is important to note that u_b becomes zero at a radius of about 28.4 km ($0.71r_m$). At that point the boundary layer equations are singular and the solutions break down. Near this radius, radial gradients are so steep that the underlying approximations of boundary-layer theory become questionable. The rapid decline in u_b near the singular radius implies a large vertical velocity at the top of the boundary layer. Indeed, the maximum upflow is much larger than that in Smith (2003). It is exceeding the values obtained by Smith (2003) by several m s^{-1} near the radius where the solution breaks down. In Smith (2003) it is only 0.15 m s^{-1} and occurs 1 km inside r_m.

The results of the new calculation exhibit a behavior that was not found in earlier studies (e.g. Smith 1968, Leslie and Smith 1970, Bode and Smith 1975) as well as in the calculations presented by Smith (2003).

So it is of interest to carry out investigations of the dynamical and thermodynamical aspects of the boundary layer, including checks using two independent codes (one a Fortran90 code and the other using Mathematica).

3.2 The new calculations - dynamical aspects

3.2.1 Dependence on boundary-layer depth

In the simple slab boundary layer model investigated by Smith (2003) only one single, radially constant boundary-layer depth has been studied. This boundary layer depth was chosen to be that of the subcloud layer in a very simple model for radiative-convective equilibrium at the starting radius.

An inspection of Eqs.(3.20)-(3.22) shows that the effective frictional stress (i.e. the surface stress divided by the boundary layer depth) and the effective enthalpy and moisture exchange coefficients are inversely proportional to the assumed depth. So it is of particular interest to investigate how the boundary-layer depth might influence the inward evolution of the layer.

For the remaining calculations the additional modifications to the model described by Smith (2003) were used. Specifically the most recent representations of the drag and heat/moisture exchange coefficients were used. These are based on the observations reported by Black *et al.* (2006). The new convective equilibrium scheme described in section 3.1 was introduced.

To aquire an equilibrium state it was necessary to choose slightly different values for the thermodynamic input parameters. These parameters are: $p_s = 1015$ hPa, $T_s = 29^o$C, $T_{as} = 28.5^o$C, $q_b = 14$ g kg^{-1}, $q_{\delta+} = 13.4$ g kg^{-1}. These lead to values for $T_{\delta+}$ and w_{sc} of 21.7^oC and -5.7 cm s^{-1}, respectively.

The results of calculations similar to those described in section 3.1.1, but for boundary layer depths 550 m, and 800 m are summarized in Fig.(3.3), which shows graphs similar to those in Fig.(3.2).

The flow behavior in the calculation for $\delta = 550$ m (Fig.(3.2), panel (a)) is similar to that for $\delta = 550$ m in Smith (2003) (Fig.(3.2), panel(b)). However, the solution becomes singular (i.e. $u_b \to 0$) at a larger radius: 35 km compared with 28.4 km. In addition, the maximum radial wind speed is lower (16 m s^{-1} compared with 21 m s^{-1}) and occurs at a slightly larger radius (54.7 km compared with 50 km). The maximum vertical velocity out of the boundary layer is less also: 1.8 m s^{-1} at $r = 35$ km compared with 3.8 m s^{-1} at r = 28.4 km in the case with $\delta = 550$ m. As the boundary layer depth increases to 679 m the radius at which the solution becomes singular increases to 40

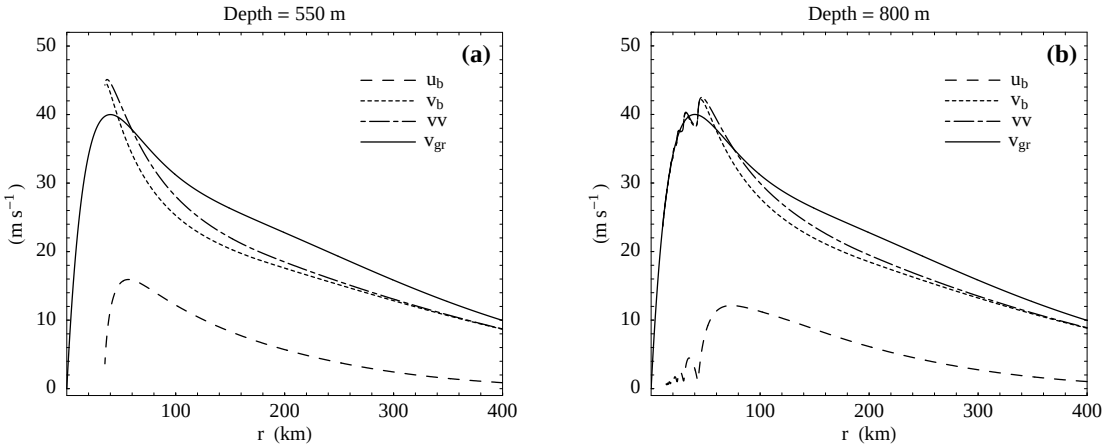

Figure 3.3: Comparison of radial profiles of radial (u_b) and tangential (v_b) wind components and the total wind speed vv in the boundary layer as well as the tangential wind speed above the boundary layer (v_{gr}), but for two calculations with boundary layer depths (a) 550 m, and (b) 800 m.

km and the maximum radial wind speed decreases to 14 m s^{-1} and the radius at which it occurs increases to 63 km. The maximum vertical velocity out of the boundary layer is slightly smaller, 1.6 m s^{-1}, and occurs at $r = 40$ km.

As δ increases beyond 679 m, a dramatic transition occurs in the solution behavior. For $\delta = 680$ m and beyond, the solution for $r < r_m$ is quite different from that for $\delta \leq 679$ m and extends to within a few kilometres of the rotation axis. In this "large depth" regime, the tangential wind speed in the boundary layer becomes subgradient again after reaching its peak supergradient value. It then oscillates about the prescribed wind profile above the boundary layer with ever decreasing amplitude as the axis is approached. The oscillations are accompanied by oscillations of the radial wind field and therefore in the vertical flow at the top of the boundary layer. This behavior is similar to that described in Smith (2003) for a vortex with $r_m = 100$ km.

The vertical motion at the top of the boundary layer in the calculations with boundary layer depths of 550 m and 800 m are shown in Fig.(3.4), panel (a) and (b). There is a slight adjustment near the starting radius on account of the sudden introduction of the inertial acceleration terms in the boundary layer, but the subsidence velocities at outer radii are relatively weak. The subsidence increases with decreasing radius and then decreases again shortly before changing to ascent. The change from subsidence to ascent occurs at a radius of 130 km when $\delta = 550$ km and 155 km when $\delta = 800$ km. Reasons for these differences are discussed below.

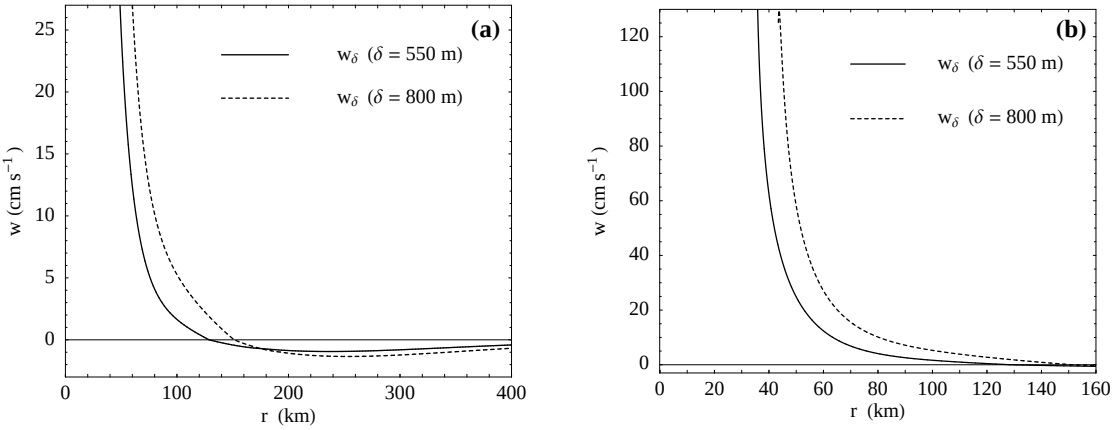

Figure 3.4: Radial profiles of vertical velocity (w_δ) at the top of the boundary layer in the calculations with boundary layer depths of 550 m and 800 m for the whole domain (panel (a)) and with emphasize on the inner region (panel (b)).

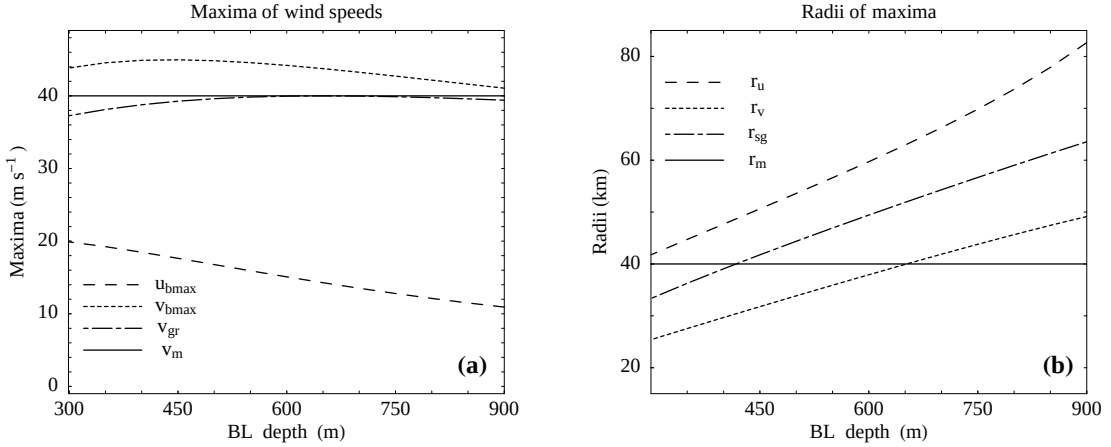

Figure 3.5: (a) Maximum radial and tangential wind speeds in the boundary layer, $u_{b,max}$ and $v_{b,max}$, and the tangential wind speed v_{gr}, at the top of the boundary layer at the radius where $v_{b,max}$ occurs, as functions of boundary-layer depth. (b) Radii r_u and r_v where the maximum radial and tangential wind speeds occur as functions of boundary-layer depth. Panel (b) also shows the first radius, r_{sg}, at which, starting from $r = R$, the tangential wind speed becomes supergradient. The solid horizontal line in panel (a) indicates the maximum tangential wind speed at the top of the boundary-layer, v_m, and that in panel (b) the radius r_m, at which this maximum occurs.

The dependence of the solutions to the boundary-layer depth is highlighted by plots of the maximum radial and tangential wind speed and the radii at which these occur as functions of δ as shown in Fig.(3.5).

As δ increases, the effective frictional stress (i.e. the surface stress divided by the boundary-layer depth) is becoming smaller. In that case the degree of supergradient flow is also progressively diminished. This behavior is visualized by the difference between the maximum tangential wind speed in the boundary layer, $v_{b,max}$, and the tangential wind speed above the boundary layer at the radius r_v at which $v_{b,max}$ occurs (Fig.(3.5), panel (a)). In contrast, r_v is growing when δ is becoming larger as shown in Fig.(3.5, panel (b)). The maximum inflow, $u_{b,max}$, decreases also (Fig.(3.5, panel (a)) while the radius at which it occurs increases (Fig.(3.5), panel(b)). It is also evident that the radius at which the flow first becomes supergradient shows an almost linear increase when δ is becoming larger. Now the question is turning up how this behavior of the solutions with varying boundary layer depth δ may be interpreted, taking Eqs.(3.20) and (3.21) into account. This topic is in detail discussed in the following section.

3.2.2 Interpretation

The foregoing behavior depends in a delicate way on the relative importance of various force terms in the radial and tangential components of the momentum equation. For the purpose of interpretation it is helpful to rewrite Eqs.(3.20) and (3.21) in the following form:

$$\frac{du_s}{ds} = \frac{w_{\delta_-} + w_{sc}}{\delta} - \frac{(v_{gr} - v_b)}{u_s}\left(\frac{(v_{gr} + v_b)}{R - s} + f\right) - \frac{C_D}{\delta}\sqrt{(u_s^2 + v_b^2)}, \quad (3.41)$$

$$\frac{dv_b}{ds} = \frac{w_{\delta_-} + w_{sc}}{\delta}\frac{(v_b - v_{gr})}{u_s} + \frac{v_b}{R - s} + f - \frac{C_D}{\delta}\sqrt{(u_s^2 + v_b^2)}\frac{v_b}{u_s}. \quad (3.42)$$

Here $u_s = -u_b$ is the radial inflow velocity and $s = R - r$, with $s \leq R$, measures distance inwards from the starting radius, R. In addition the flux terms on the far right of Eqs.(3.20) and (3.21) have been replaced with the formulation described in section (3.1). In this form the equations show how the (inward) radial and tangential components of flow change with decreasing radius.

If there are no frictional stresses the converging rings of air conserve their absolute

angular momentum, $rv + \frac{1}{2}fr^2$, and spin faster. However, in the boundary layer these rings of air are still spinning faster. But of course now frictional torque is acting and therefore the rate at which v_b increases is reduced significantly. This effect is represented by the last term in Eq.(3.42):

$$\frac{C_D}{\delta}\sqrt{(u_s^2 + v_b^2)}\frac{v_b}{u_s}.$$

For the development of supergradient winds it is now necessary to have a sufficiently large radial displacement of air parcels in the boundary layer. This displacement is on the other hand just possible if the radially-inward wind speeds are large enough.

From a Lagrangian viewpoint one may think of air parcels spiralling inwards. As they move slower inwards the tracks they follow become longer. This means that they have a longer way to go along where friction can act and reduce v_b.

An inspection of Eq.(3.42) shows that this effect is contained in the terms proportional to the inverse of u_s.

The foregoing discussion makes clear that the development of supergradient winds depends on the radial gradient of absolute angular momentum in the boundary layer and hence on that above the layer. This feature is also explored in the context of a linear boundary-layer model by Kepert (2001) and Kepert and Wang (2001). It is also consistent with the results in the context of the linear model in the foregoing chapter.

Equation (3.41) shows that the only term that can cause a radially-inward acceleration in the slab model is the net pressure gradient. The effect of this pressure gradient is contained in the second term on the right-hand-side of Equation (3.41):

$$\frac{(v_{gr} - v_b)}{u_s}\left(\frac{(v_{gr} + v_b)}{R - s} + f\right).$$

This term describes the net inward force which is due to the difference between the radial pressure gradient and the centrifugal and Coriolis forces. The first term in Eq.(3.41)

$$\frac{w_{\delta_-} + w_{sc}}{\delta}$$

stands for the effects of the downward transport of radial momentum. This is zero in the present model. Finally the third term

$$\frac{C_D}{\delta}\sqrt{(u_s^2 + v_b^2)}$$

represents the frictional stress. Both of these act to reduce the radial inflow. If the flow is supergradient, i.e. if $v_b > v_{gr}$, the net pressure gradient acts radially outwards also. The net inward force increases with the degree to which the tangential flow in the boundary layer is subgradient (i.e. to $v_{gr} - v_b$), which in turn increases as the effective frictional torque becomes larger. Equation (3.42) shows that this torque is the only term that leads to a reduction of v_b with decreasing radius as long as the flow in the boundary layer remains supergradient. The friction terms are inversely proportional to the boundary-layer depth. This means that shallower boundary layers favour lower tangential wind speeds. However shallower boundary layers lead to larger radial wind speeds. This is because, at least in the outer part of the vortex for large radii, they cause a larger net pressure gradient. If one approaches the core region of the vortex and the radii are becoming smaller the situation is a little different. Now the term $v_b/(R - s)$ in Eq.(3.42) becomes large and contributes to an increase in v_b with s. Thus larger radial wind speeds favor larger tangential wind speeds. This is because air parcels may move rapidly to smaller radii, where this effect is important. In addition they suffer less total frictional torque on the way (note that the frictional term in Eq.(3.42) decreases as u_s increases). The key to what determines the two flow regimes depends on which of the foregoing processes dominates and boils down to whether or not the flow can become subgradient again before u_b becomes zero. In the calculation with $\delta = 680$ m, the tangential flow just manages to become subgradient before u_b becomes zero, whereupon the inflow begins strengthen again with decreasing radius. Because the tangential wind speed at the top of the boundary layer decreases also, the flow again becomes supergradient so that u_b decreases rapidly and $v_b - v_{gr}$ decreases until u_b becomes subgradient again. These fluctuations are a kind of damped inertial oscillation as described in Smith (2003). These waves are not very significant in reality. It is more realistic to interpret them as an artifact which is descended of the prescription of the tangential wind field at the top of the boundary layer. The radial scale of the waves is on the order of a few kilometers and decreases with radius. Thus such waves would not be resolvable by most numerical models of hurricanes. Moreover the implied radial gradients associated with them would stretch the assumptions of boundary layer theory, which assumes radial gradients of quantities to be small compared with vertical gradients. It turns that these oscillations have much smaller amplitudes in calculations that allow the boundary depth to decline with radius (see section (3.2.6)).

The dynamical interpretations given above provide also an explanation for the differ-

ences in the radial location where, w_δ changes sign in Fig.(3.4). The larger effective friction for the shallower boundary layer implies a larger net radial pressure gradient, which, in turn, leads to a larger acceleration of the radial flow and a decrease in the radius at which the radial gradient of inward mass flux changes sign.

3.2.3 Dependence on vortex intensity

Decreasing the vortex intensity has an effect similiar to increasing the boundary layer depth. A repeat of the control calculation for different values of the maximum tangential wind speed at the top of the boundary layer, v_m, shows that as v_m decreases, the strength of supergradient winds decreases. In addition, the transition in regime from one, in which u_b becomes zero before v_b reduces to v_{gr}, to one in which v_b oscillates about v_{gr}, occurs at a smaller boundary-layer depth.

For example, if $\delta = 550$ m, the regime transition occurs if v_m is reduced by just 8 m s^{-1} to 32 m s^{-1}. As v_m decreases further, the behavior is similar to that when δ decreases at fixed v_m. Theses findings are consistent with the results of Kepert (2001). In his Figure 1, he showed that a larger gradient wind speed leads to a stronger jet, i.e. to an increase in the strength of supergradient winds. The behavior discussed above suggests that it might be possible to rescale the equations in a way that the v_m and δ dependence condenses into a single parameter, but this does not appear to be the case.

3.2.4 Dependence on mixing by shallow convection

Smith (2003) showed that it is important to include a representation of downward mixing by shallow convection. This prevents the boundary layer from completely saturating. The formulation is necessarily crude because thermodynamic quantities are not predicted above the boundary layer. This means that there is no physical basis for allowing the mass transport due to shallow convection to vary with radius. Nevertheless it is pertinent to ask how sensitive the foregoing results are to the magnitude chosen for w_{sc}. To answer this question two additional calculations were carried out, similar to the control calculation, but with $w_{sc} = 0$ in one and $w_{sc} = -10$ cm s^{-1} in the the other. It turns out that for $w_{sc} = 0$, the transition in boundary layer behavior described in section (3.2.1) occurs at a larger boundary layer depth (765 m instead of

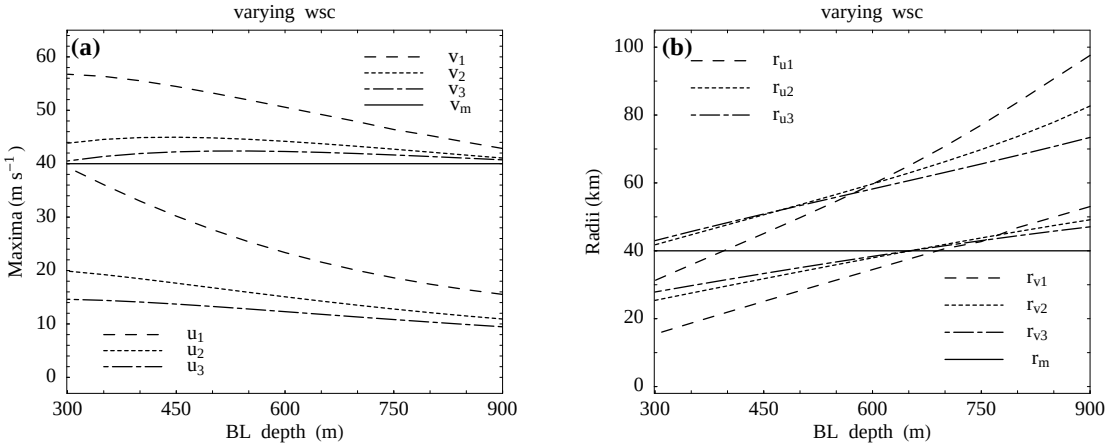

Figure 3.6: (a) Maximum radial and tangential wind speeds (u_n and v_n, respectively, $n = 1, 2, 3$) in the boundary layer, and the tangential wind speed at the top of the boundary layer at the radius at which the maximum v_n occurs, as functions of the boundary layer depth for three different values for w_{sc}: 0, -5 and -10 cm s^{-1}. (b) Radii at which the maximum radial and tangential wind speeds occur (r_{un} and r_{vn}, respectively) as functions of boundary layer depth. Solid horizontal lines are as in Figure (3.5).

680 m). In the case where $w_{sc} = -10$ cm s^{-1} and $v_m = 40$ m s^{-1}, there is no transition in behavior for any boundary layer depth. The tangential wind speed in the boundary layer becomes subgradient again after reaching its maximum value and then oscillates about the prescribed wind profile for any boundary layer depth. At the same time the radial wind field and the vertical flow oscillate. All of these effects are presented in Fig.(3.6), which shows the maxima of radial and tangential wind speed in the boundary layer (panel (a)) and the radii, where the maxima occur (panel (b)) as functions of the boundary-layer depth for the three values of w_{sc}. The maximum radial wind speed for $w_{sc} = 0$ is denoted by u_1, for $w_{sc} = -5$ cm s^{-1} by u_2, and for $w_{sc} = -10$ cm s^{-1} by u_3. The radii at which u_1, u_2 and u_3 occur are denoted by r_1, r_2 and r_3, respectively.

If δ is fixed both the maximum of the radial and of the tangential components are becoming smaller if the value of $|w_{sc}|$ is increasing. The maximum inflow is also becoming larger for a shallower boundary layer as it is for the degree of supergradient wind speed when $w_{sc} = 0$. However, if $|w_{sc}|$ is 5 cm s^{-1} and 10 cm s^{-1} the degree of supergradient wind is maximal for an intermediate value of δ.

The reason for the foregoing behavior is that the downward mixing of radial momentum by shallow convection reduces the strength of the inflow directly and thereby the strength of supergradient winds that can be achieved. An indirect reduction of the

inflow is caused by the downward mixing of azimuthal moment. This process causes a reduction of the net inward force and hence an indirect reduction of the inflow. In any case a diminished inflow causes a significant reduction of the strength of supergradient winds that may be obtained. If one fixes a value of w_{sc} this effects can be reduced by choosing a smaller boundary layer depth δ. This is due to the fact that the reduction of δ leads to a stronger effective frictional force in the boundary layer. The radii at which the maxima in u_b and v_b occur increase with δ. This effect, i.e. the rate of increase is largest for a calculation without any mixing by shallow convection.

Further calculations showed that the maximum amount by which the tangential wind becomes supergradient is sensitive to changes in w_{sc} and decrease significantly as w_{sc} increases in magnitude. The maximum vertical flow at the top of the boundary layer decreases a little also and the radius at which it occurs increases.

3.2.5 Dependence on a varying drag coefficient

It is also possible to investigate the effects of variations in the drag coefficient. It was defined $C_D = C_{D0} + C_{D1}|\vec{v}|$ and it was assumed that the drag coefficient does not increase further for total wind speeds larger that 20 ms^{-1}. C_D can be written in the form $C_D = C_{D0}(1 + cdx|\vec{v}|)$, where $cdx = \frac{C_{D1}}{C_{D0}}$. To investigate a broad range of profiles for C_D it is possible to vary the parameter cdx linearly.

Figure (3.7), panel (a), shows the maximum radial and tangential wind speeds in the boundary layer, and the tangential wind speed at the top of the boundary layer at the radius at which the maximum v_b occurs, as functions of $1/cdx$. An increase in $1/cdx$ corresponds to a reduction of the drag coefficient. It is seen that an increase in $1/cdx$ results in a decrease of radial wind speed in the boundary layer as well as in the tangential wind speed. This confirms the idea that increased frictional stress at the ground reduces the wind speeds above, when the frictional stress is represented by

$$\frac{C_D}{\delta}\sqrt{(u_s^2 + v_b^2)}.$$

From Fig.(3.7), panel (b), it is seen that not only the absolute values of the radial and the tangential wind speeds in the boundary layer are affected by a varying drag coefficient. Panel (b) shows the radii at which the maximum radial and tangential wind speeds occur (r_u and r_v, respectively) and the radius r_1, where the tangential

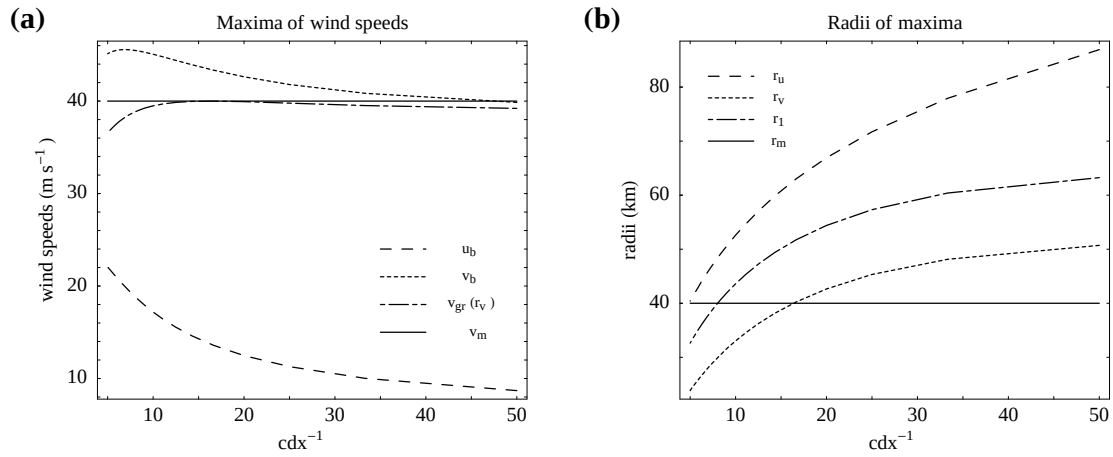

Figure 3.7: (a) Maximum radial and tangential wind speeds, (u_b and v_b), in the boundary layer, and the tangential wind speed at the top of the boundary layer at the radius at which the maximum v_b occurs, as functions of $1/cdx$. (b) Radii at which the maximum radial and tangential wind speeds occur (r_u and r_v, respectively) and the radius r_1, where the tangential wind speed is equal to v_{gr} as functions of $1/cdx$. Solid horizontal lines indicate $v_m = 40$ ms^{-1}, (panel (a)), and $r_m = 40$ km, (panel (b)).

wind speed is equal to v_{gr} as functions of $1/cdx$. It is seen from panel (b) that the maxima of the radial and the tangential wind occur at larger radii when $1/cdx$ is increased. It is also seen that the tangential wind speed turns supergradient further out from the core when $1/cdx$ is increased.

3.2.6 Effects of radially-varying boundary-layer depth

The model described in section 3.1 assumes a constant boundary layer depth. This may in fact not be too accurate. A scale analysis of the equations as presented in the foregoing chapter suggested that the boundary layer depth should decline with the radius. This may easily be seen by an inspection of the boundary layer depth scale derived there. Also the linear solution to the full boundary-layer equations (Eliassen and Lystad 1977, Kepert 2001 and Vogl and Smith 2009) suggests that the depth should decrease with declining radius at a rate inversely proportional to $\sqrt{C}$, where

$$C = (\zeta_{gr} + f)\left(\frac{2v_{gr}}{r} + f\right)$$

and

$$\zeta_{gr} = \frac{1}{r}\left(\frac{d(rv_{gr})}{dr}\right)$$

is the vertical component of relative vorticity at the top of the boundary layer. It is not possible to determine the radial variation of δ in the slab-model. However, it is straightforward to modify the Eqs.(3.20) - (3.23) to allow for a prescribed variation of $\delta(r)$. Now it is assumed that the boundary layer depth $\delta(r)$ is a prescribed function of radius r.

Starting with the boundary-layer equations (3.20) - (3.23) it is for $\delta = \delta(r)$:

$$\frac{d}{dr}\left(\int_0^{\delta(r)} ru^2 dz\right) - \delta'(r)ru^2 + (ruw)|_{z=\delta(r)} + \int_0^{\delta(r)} (v_{gr}^2 - v^2)dz + rf\int_0^{\delta(r)} (v_{gr} - v)dz = -Kr\frac{\partial u}{\partial z}\Big|_0,$$

$$\frac{d}{dr}\left(\int_0^{\delta(r)} r^2 uv dz\right) - \delta'(r)r^2 uv + (r^2 vw)|_{z=\delta(r)} + r^2 f\int_0^{\delta(r)} u dz = -Kr^2\frac{\partial v}{\partial z}\Big|_0,$$

$$\frac{d}{dr}\left(\int_0^{\delta(r)} ru\chi dz\right) - \delta'(r)ru\chi + (r\chi w)|_{z=\delta(r)} + = -Kr\frac{\partial \chi}{\partial z}\Big|_0,$$

$$\frac{d}{dr}\left(\int_0^{\delta(r)} ru dz\right) - \delta'(r)ru + (rw)|_{z=\delta(r)} = 0,$$

whereupon

$$\frac{d}{dr}(\delta(r)ru_b^2) - \delta'(r)ru_b^2 + w_{\delta_+}ru_b + \delta(r)(v_{gr}^2 - v^2) + \delta(r)rf(v_{gr} - v) = -C_D r(u_b^2 + v_b^2)^{\frac{1}{2}}u_b,$$

$$\frac{d}{dr}(\delta(r)ru_b rv_b) - \delta'(r)ru_b rv_b + w_{\delta_+}r^2 v_b + w_{\delta_-}r^2 v_{gr} + \delta(r)r^2 fu_b = -C_D r^2(u_b^2 + v_b^2)^{\frac{1}{2}}v_b,$$

$$\frac{d}{dr}(\delta(r)ru_b\chi_b) - \delta'(r)ru_b\chi_b + w_{\delta_+}r\chi_b + w_{\delta_-}r\chi_{\delta_+} + \delta(r)r^2 fu_b = -C_\chi r(u_b^2 + v_b^2)^{\frac{1}{2}}(\chi_s - \chi_b),$$

and

$$\frac{d}{dr}(\delta(r)ru_b) - \delta'(r)ru_b = -rw_\delta. \tag{3.43}$$

Now $\frac{d}{dr}(\delta(r)ru_b)\eta$ is examined with a dependent variable η which is u_b, rv_b or χ_b. It is

$$\frac{d}{dr}(\delta(r)ru_b)\eta \;=\; \delta(r)ru_b\frac{d}{dr}\eta + \eta\frac{d}{dr}(\delta(r)ru_b) \tag{3.44}$$

and from Eq.(3.43) follows now

$$\frac{d}{dr}(\delta(r)ru_b)\eta = \delta(r)ru_b\frac{d}{dr}\eta + \eta(\delta'(r)ru_b - rw_\delta). \tag{3.45}$$

Using this identity and simplifying the equations one ends up with a set of differential equations of the same type as for constant δ, where δ is just replaced by $\delta(r)$:

$$u_b\frac{du_b}{dr} = u_b\frac{w_{\delta_-}}{\delta(r)} - \frac{(v_{gr}^2 - v_b^2)}{r} - f(v_{gr} - v_b) - \frac{C_D}{\delta(r)}(u_b^2 + v_b^2)^{\frac{1}{2}}u_b, \quad (3.46)$$

$$u_b\frac{dv_b}{dr} = \frac{w_{\delta_-}}{\delta(r)}(v_b - v_{gr}) - (\frac{v_b}{r} + f)u_b - \frac{C_D}{\delta(r)}(u_b^2 + v_b^2)^{\frac{1}{2}}v_b, \quad (3.47)$$

$$u_b\frac{d\chi_b}{dr} = \frac{w_{\delta_-}}{\delta(r)}(\chi_b - \chi_{\delta_+}) + \frac{C_\chi}{\delta(r)}(u_b^2 + v_b^2)^{\frac{1}{2}}(\chi_s - \chi_b). \quad (3.48)$$

If a representation of turbulent fluxes at the top of the boundary layer is included, terms $\overline{(u'w')}_\delta$, $\overline{(v'w')}_\delta$, $\overline{(\chi'w')}_\delta$ have to be added to the equations and with a representation of radiative cooling $\dot{\chi}_b$ the equations take their final form:

$$u_b\frac{du_b}{dr} = u_b\frac{w_{\delta_-}}{\delta(r)} - \frac{(v_{gr}^2 - v_b^2)}{r} - f(v_{gr} - v_b) - \frac{C_D}{\delta(r)}(u_b^2 + v_b^2)^{\frac{1}{2}}u_b - \frac{\overline{(u'w')}_\delta}{\delta(r)}, \quad (3.49)$$

$$u_b\frac{dv_b}{dr} = \frac{w_{\delta_-}}{\delta(r)}(v_b - v_{gr}) - \left(\frac{v_b}{r} + f\right)u_b - \frac{C_D}{\delta(r)}(u_b^2 + v_b^2)^{\frac{1}{2}}v_b - \frac{\overline{(v'w')}_\delta}{\delta(r)}, \quad (3.50)$$

$$u_b\frac{d\chi_b}{dr} = \frac{w_{\delta_-}}{\delta(r)}(\chi_b - \chi_{\delta+}) + \frac{C_\chi}{\delta(r)}(u_b^2 + v_b^2)^{\frac{1}{2}}(\chi_s - \chi_b) - \frac{\overline{(\chi'w')}_\delta}{\delta(r)} - \dot{\chi}_b. \quad (3.51)$$

Now Eq.(3.43) is used to modify (3.49) to provide an expression for w_δ. Writing (3.43) as

$$\frac{d}{dr}(\delta(r)ru_b) = \delta'(r)ru_b - rw_\delta \quad (3.52)$$

and carrying out the differentiation gives

$$\delta'(r)rub + \delta(r)\left(u_b + r\frac{d}{dr}u_b\right) = \delta'(r)ru_b - rw_\delta. \quad (3.53)$$

Finally

$$\frac{d}{dr}u_b = \frac{1}{\delta(r)r}(-rw_\delta - \delta(r)u_b), \quad (3.54)$$

which leads to an expression for w_δ.

It is seen from the foregoing analysis that Eqs.(3.20) - (3.22) do not change in the case of a radially varying boundary layer depth. It is the vertical velocity that is affected. To summarize the calculations for $\delta = \delta(r)$ the average of any quantity $\phi(r, z)$ across the boundary layer is defined as

$$\phi_b = \frac{1}{\delta}\int_0^{\delta(r)} \phi(r,z)dz. \tag{3.55}$$

With this definition it immediately follows that

$$\frac{d\phi_b}{dr} = \frac{1}{\delta(r)}\int_0^{\delta(r)} \frac{d\phi(r,z)}{dr}dz - \left[\frac{1}{\delta(r)}\frac{d\delta(r)}{dr}\left(\phi_b - \phi_{\delta_+}\right)\right]. \tag{3.56}$$

Here ϕ_{δ_+} denotes the value of $\phi(r,z)$ just above the boundary layer. This equation can be applied to the radial velocity u_b in the boundary layer. Then the continuity equation

$$\frac{1}{r}\left(\frac{\partial ru}{\partial r} + \frac{\partial w}{\partial z}\right) = 0$$

gives

$$w_\delta = -\frac{1}{r}\frac{d}{dr}(ru_b\delta(r)) \tag{3.57}$$

and finally it follows

$$w_\delta = \frac{\delta(r)}{1+\alpha}\left[\frac{1}{u_b}\left(\frac{(v_{gr}^2 - v_b^2)}{r} + f(v_{gr} - v_b) + \frac{C_D}{\delta(r)}\sqrt{(u_b^2+v_b^2)}u_b\right) - \frac{u_b}{r}\right] - u_b\frac{d\delta(r)}{dr}. \tag{3.58}$$

In difference to the equation for w_δ for a constant boundary layer depth δ (Eq.(3.24)) the modified expression contains the additional summand $-u_b\frac{d\delta(r)}{dr}$. As an analysis showed, the contribution of this term turns out to be rather small. However for completeness it is added for the calculations with a radially varying boundary layer depth.

To assess the effect of a decrease in the boundary layer depth with declining radius we carried out a calculation in which

$$\delta(r) = \delta(R)\sqrt{(C_g/C)},$$

where $\delta(R)$ is the boundary layer depth at the starting radius, R, C_g is the value of C at this radius and

$$C = (\zeta_{gr} + f)\left(\frac{2v_{gr}}{r} + f\right)$$

as defined before. Fig.(3.8) shows the radial variation of $\delta(r)/\delta(R)$ for the vortex profile used here.

The solutions for $\delta(R) = 550$ m and 800 m are shown in Fig.(3.9).

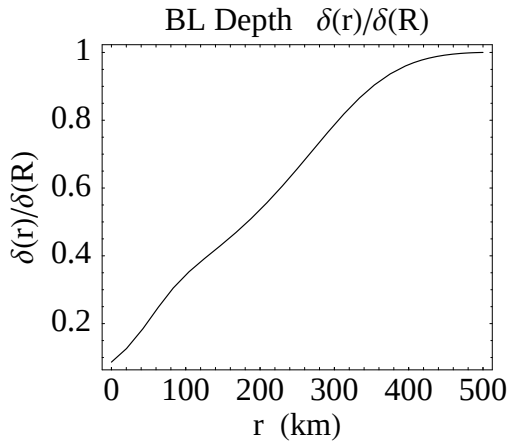

Figure 3.8: Assumed radial variation of the ratio of boundary-layer depth, $\delta(r)$, to that at radius R, $\delta(R)$, for the calculations shown in Fig.(3.9).

In both cases the tangential wind speeds in the boundary layer are decreased, especially inside a region of about 200 km and the peak winds are significantly lower in magnitude than v_m. In contrast the peak radial winds are larger than in the constant-depth calculations, especially in the calculation for $\delta(R) = 800$ m and the maxima occur at markedly smaller radii. These differences in behavior are consistent with the ideas presented in section (3.2.2). Here it was noted that a decreasing boundary-layer depth implies a larger effective drag throughout the layer. When the boundary-layer depth decreases towards the center of the vortex, the maximum vertical velocity at the top of the layer is reduced considerably from that in the constant-depth calculations. This results are more in line with that in previous calculations (e.g. Kepert and Wang 2001: see e.g. their Fig.(3)). The reducing-depth calculations still show slightly supergradient wind speeds and oscillations in radial and vertical motion, but now well inside r_m and again in a region where radial gradients are probably steep enough to invalidate the assumptions of boundary layer theory.

3.2.7 Effects of downward momentum transport

The calculations presented by Smith (2003) showed that in regions where there is inflow into the boundary layer ($w_\delta < 0$), the contribution of the terms involving $w_{\delta-} < 0$ to the radial derivatives on the left of Eqs.(3.20) - (3.22) is small. This suggests that a simplified approximate system of equations could be obtained by setting $w_{\delta-} = 0$ in

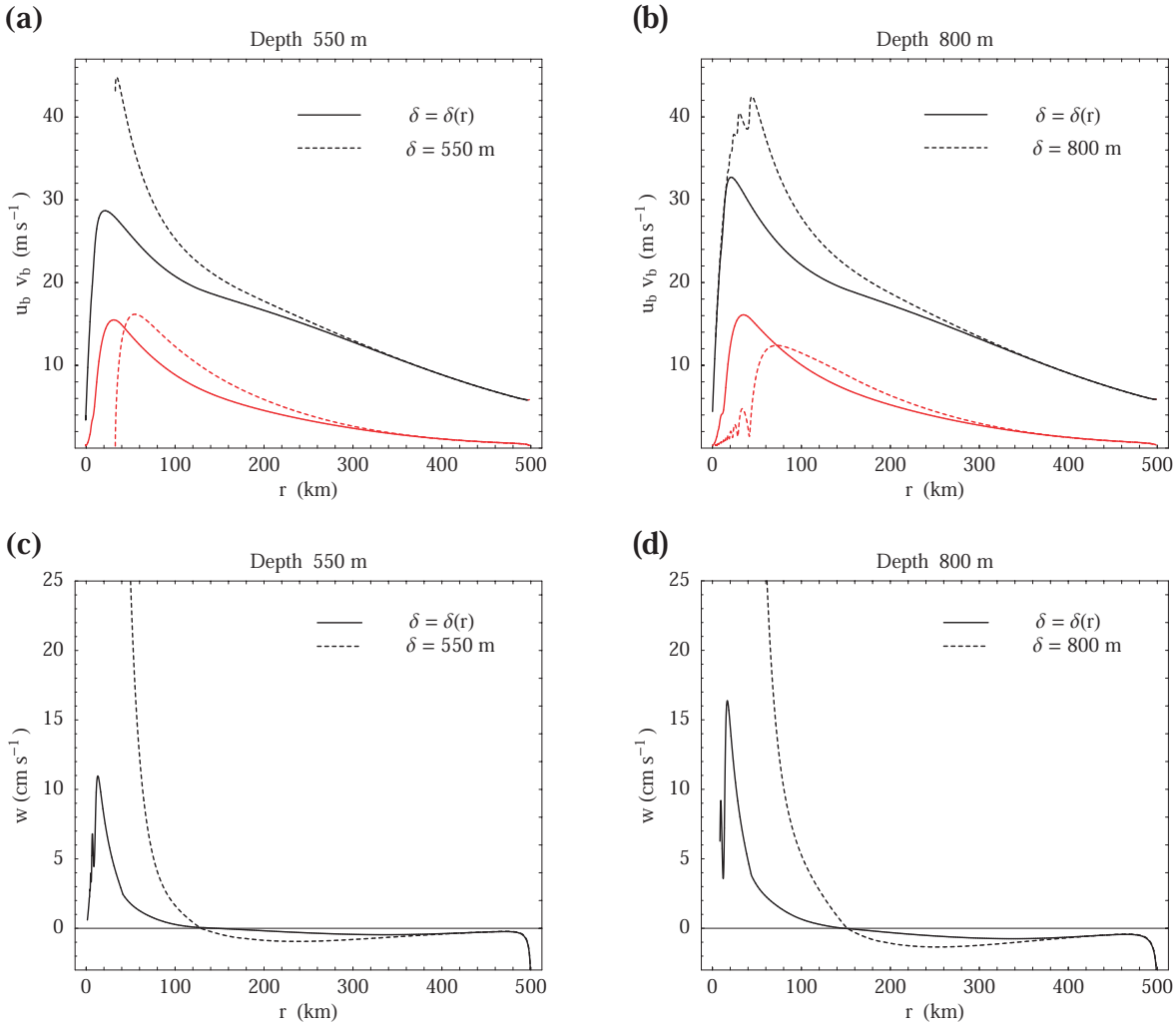

Figure 3.9: Comparison of radial wind speeds (red) and tangential wind speeds (black) in the boundary layer in the control calculation, which has a fixed depth $\delta(R)$ and a calculation in which $\delta(r) = \delta(R)\sqrt{(C_g/C)}$. (a) $\delta(R) = 550$ m, (b) $\delta(R) = 800$ m. Panels (c) and (d) show the corresponding comparisons of the vertical velocity at the top of the boundary layer.

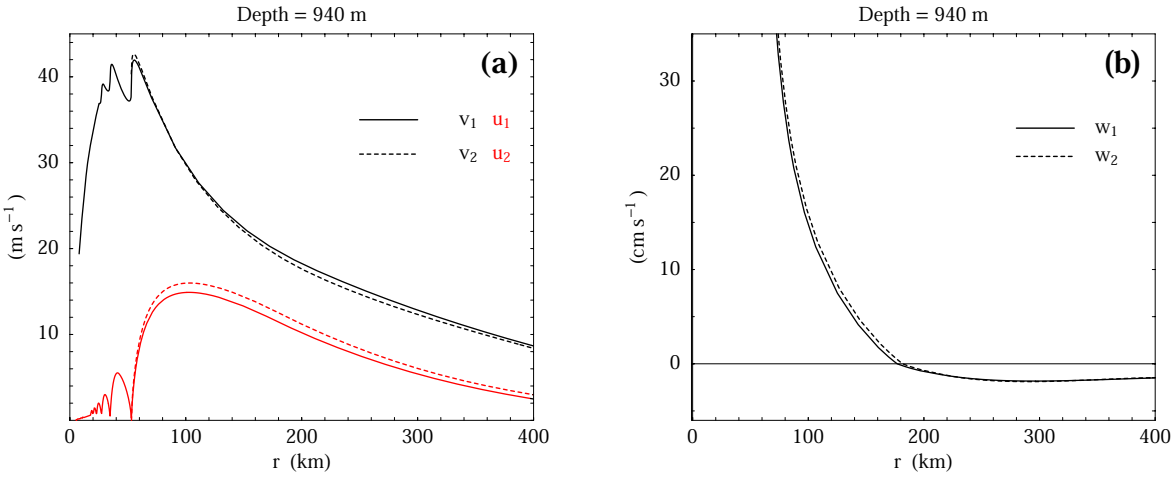

Figure 3.10: (a) Comparison of the radial and tangential wind speeds for a calculation with $\delta = 940$ m and without shallow convection (u_1 and v_1), and one in which $w_{\delta\_}$ is set to zero (u_2 and v_2). (b) compares the vertical motion (w_1 and w_2) at the top of the boundary layer in these two calculations

these equations and by diagnosing w_δ using the continuity equation, Eq.(3.23). Such an approximation is made, for example, by Emanuel (1986, 1995) in the development of a steady-state model for a hurricane. Here the accuracy of this approximation is explored in the case, where the boundary-layer depth varies with radius as in the foregoing section.

Figure (3.10) compares the radial and tangential wind components in the boundary layer and the vertical motion at the top of the boundary layer in two calculations. The first one is like the control calculation, but with a boundary layer depth of 940 m and no representation of shallow convection, the other one is just the same, but with the foregoing approximations. Evidently the approximation is quite acceptable. The neglect of the downward transport of momentum by the mean vertical motion has a negligible effect on the tangential wind field, but it leads to a slightly larger inflow. The predicted vertical velocity is marginally higher within a radius of about 210 km as it is shown in Fig.(3.10, panel (b)), but there is little difference beyond that radius. Even at radii less than r_m, the vertical motion is similar until a radius of about 50 km, where the approximate calculation breaks down. Evidently, for this boundary layer depth, the calculation is close to its transition point.

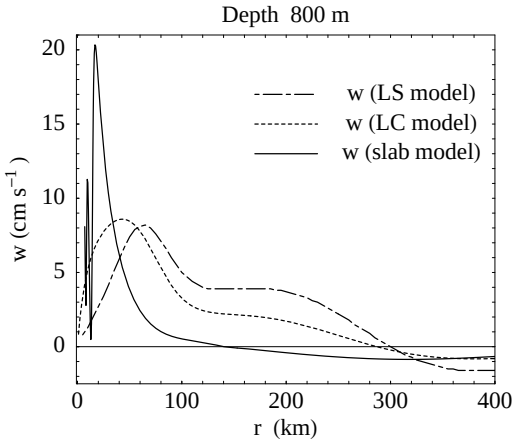

Figure 3.11: Comparison of vertical motion at the boundary layer top (800 m) predicted by the nonlinear slab model (solid line), the linear slab model (LS) and the linear model that allows the boundary layer to have vertical structure (LC).

3.2.8 Vertical motion at the top of the boundary layer

The formula for the vertical velocity at the top of the boundary layer (Eq.(3.24)) differs considerably from that derived by Kepert (2001), his Equation (28), which is based on a linear approximation to the full boundary-layer eqution and, indeed, from that obtained from a linear approximation to the slab model (see Smith and Montgomery 2008). The differences in vertical motion predicted by these different formulae for the tangential wind profile v_{gr} used here are shown in Fig.(3.11).

It is seen that the vertical velocity profile in the full nonlinear model is more peaked than in the approximate theories and the maximum upflow velocity is more than twice that of the linear theories and occurs at a significantly smaller radius. The linear slab model and the more complete version give similar profiles and similar maxima, but the maximum inflow occurs at a larger radius in the slab model.

3.3 Thermodynamical aspects

3.3.1 Dependence on boundary-layer depth

In difference to most of the models of the hurricane boundary layer the model discussed here provides the possibility to investigate not only the dynamical fields but also the

thermodynamical fields. An investigation of the thermodynamics was also presented by Smith (2003). The calculations discussed here include, *inter alia*, an improved algorithm for calculating the radiative-convective equilibrium state at the starting radius and have slightly different parameter values as used in Smith (2003). Therefore a comparison of the results is not as insightful as for the dynamic fields.

Here two of the new solutions for boundary layer depths of 550 m and 800 m are shown. The details are summarized in Fig.(3.12). Panels (a) and (c) of this show the radial profiles of the boundary layer temperature, specific humidity, saturation specific humidity, and saturation specific humidity at the sea surface, (q_{ss}) for the two solutions, while panels (b) and (d) of Fig.(3.12) show the sensible and latent heat fluxes at the surface and through the top of the boundary layer.

The boundary layer temperature is nearly constant in both cases with a value of about 25.8 ^{o}C for $\delta = 550$ m and the slightly smaller value of 24.5 ^{o}C for $\delta = 800$ m, but shows a small rise in the inner core region at radii less than about 100 km. In essence, the mean boundary layer temperature largely follows the sea surface temperature. Note that the temperature in the boundary layer decreases adiabatically with height and therefore it is in general $T_b < T_{SST}$. The increase in the core region is associated with dissipative heating, which appears to be significant at high wind speeds. Consistent with this heating, the sensible heat fluxes are slightly negative in the core region. Recently Smith (2006, 2007) showed that an inviscid balanced vortex, where the tangential circulation decays with height, has a cold core in regions near and directly at the surface.

The present calculations show that this is not the case when one accounts for the boundary-layer effects. Of course the strong surface winds and the effects of unsaturated downdraught cause some upwelling (Cione *et al.* 2000). This upwelling is the reason for some cooling of the ocean surface. An effect which is neglected here and hence must be kept in mind when comparing the two cases.

The results presented here suggest also that there is a kind of balance between two processes. On the one hand there is a kind of adiabatic cooling when air parcels are spiralling towards the core region, where the lowest pressure is obtained. On the other hand in outer regions of the vortex there are sensible heat fluxes and in the core region some dissipative heating is acting. This adiabatic cooling is more than compensated by the sensible heat fluxes and the dissipative heating.

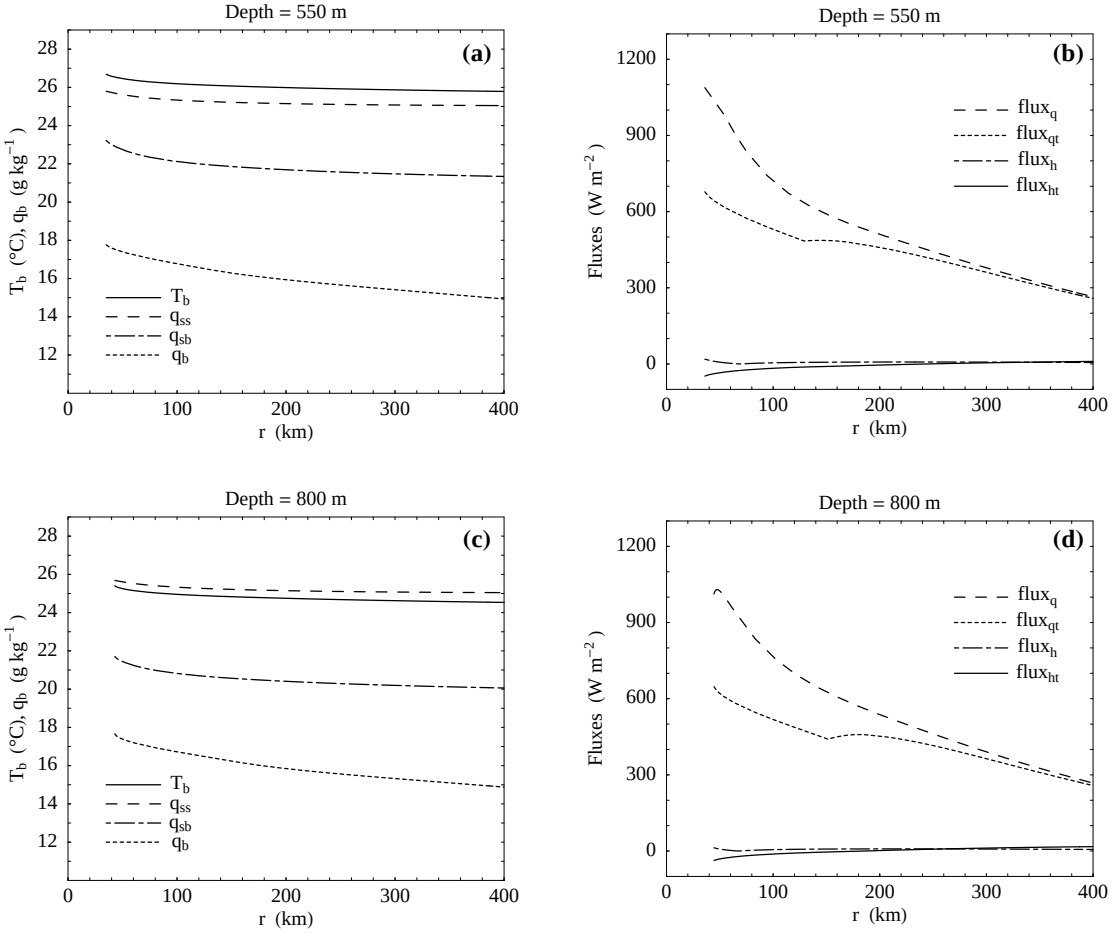

Figure 3.12: Radial profiles of boundary-layer temperature, T_b (^{o}C), specific humidity, q_b, saturation specific humidity, q_{sb}, and the saturation specific humidity at the sea surface , q_{ss} (all g kg^{-1}), for boundary-layer depth (a) 550 m and (c) 800 m. (b) and (d) show corresponding latent and sensible heat fluxes from the sea surface (flux$_q$ and flux$_h$, respectively) and through the top of the boundary layer (flux$_{qt}$ and flux$_{ht}$). All fluxes are given in W m^{-2}. Note that the sign of flux$_{ht}$ has been reversed for convenience of plotting.

The specific humidity shown in Fig.(3.12), panel (a), increases markedly with decreasing radius from a value of 14.5 $\mathrm{g\,kg^{-1}}$ at $r = 500$ km to about 17.8 $\mathrm{g\,kg^{-1}}$ at $r = 35$ km. This increase is associated with an increasing surface moisture flux, which outweighs the flux of dry air through the top of the boundary layer (panels (b) and (d)). The saturation specific humidity, q_{bs}, for a boundary layer depth of 550 m varies between 21.3 $\mathrm{g\,kg^{-1}}$ and 23.2 $\mathrm{g\,kg^{-1}}$ for radii between 500 km and about 35 km. The values for the deeper boundary layer ($\delta = 800$ m) are typically about 1.5 $\mathrm{g\,kg^{-1}}$ smaller. It is interesting to note that in both cases, $q_b < q_{ssst}$ at all radii. Thus the air does not become saturated near the sea surface, but the lifting condensation level lowers as the boundary layer moistens. The latent heat fluxes shown in Fig.(3.12), panel (b) and (d), are much larger than the sensible heat fluxes and they increase strongly with decreasing radius. The latent heat flux is coupled with the near-surface wind speed and the degree of disequilibrium between specific humidity of the air near the surface and the saturation specific humidity at the sea-surface. This means that if the latter is increasing the same is valid for the latent heat flux. Since the saturation specific humidity at the sea-surface is becoming larger with decreasing pressure, the degree of disequilibrium is maintained (see Figs. (3.12), panel (a) and panel (c)) and, of course, the wind speed increases with decreasing radius. The growing boundary layer moisture is causing an enhancement of the moisture contrast at the top of the boundary layer. This is due to the fact that the specific humidity of air above the boundary layer is held constant in the present model. It is this amplification in moisture contrast that accounts for the increase in the magnitude of the latent heat flux at the top of the boundary layer towards the vortex center. It is questionary how realistic this amplification in the moisture contrast is. Convective processes should increase the moisture content of the air above the boundary layer step by step towards the core region. The increase of the saturation specific humidity which is obtained in the calculations shown here should be even higher in reality. This means that the predicted growth of q_b for decreasing radius is only a lower bound for that expected in reality. The curves for the latent heat flux at the top of the boundary layer show a kink at the radius, where w_δ changes sign (about 130 km for $\delta = 550$ m and 150 km for $\delta = 800$ m). Inside these radii, $w_{\delta-}$ is zero and does not contribute to the fluxes at $z = \delta$. At large radii, w_{sc} dominates so that the moisture flux terms are similar for both values of δ. As the radius decreases the terms diverge from one another as $w_{\delta-}$ becomes significant.

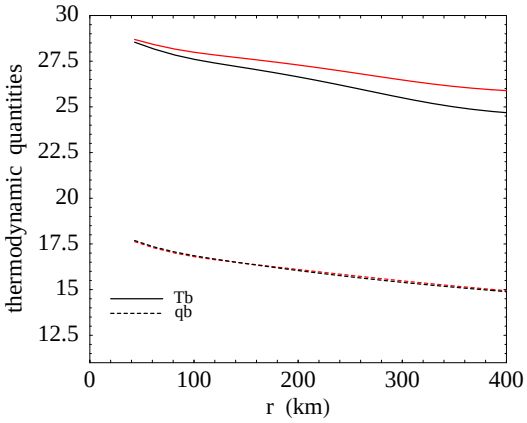

Figure 3.13: Radial profiles of boundary-layer temperature, T_b (^{o}C), and specific humidity, q_b (g kg^{-1}), for boundary-layer depth $\delta(R) = 550$ m (red) and $\delta(R)$= 800 m (black).

3.3.2 Effects of radially-varying boundary-layer depth

Now the calculation is repeated for a radially varying boundary layer depth $\delta = \delta(r)$. It is found that there is less sensitivity in the results for the thermodynamic variables as in those for the dynamical quantities. Calculations with $\delta(R) = 550$ m and $\delta(R) = 800$ m lead to results which are very similiar to those with a constant δ at large radii. This is to be expected since the boundary layer depth is in both cases similiar in that region. At the radius of maximum tangential wind speed above the boundary layer, r_m=40 km, the values are slightly higher.

It is seen from Fig.(3.13) that T_b is raised by about 1 ^{o}C while q_b is about maximally 1.5 g kg^{-1} higher compared to those shown in Fig.(3.12). In the calculations with a varying depth the peak values of T_b and q_b are very similiar. It is $T_b = 28.5^o$C and q_b =18 g kg $^{-1}$. This is due to the fact that both boundary layer depths, the one with $\delta(R) = 550$ m and the one with $\delta(R) = 800$ m, become very similiar at inner radii. For this calculations it was shown that the vertical velocities are becoming much smaller than in the cases with constant δ. This is the reason why there are no recognizable kinks in the curves for the moisture fluxes as shown in Fig.(3.14), at the top of the boundary layer.

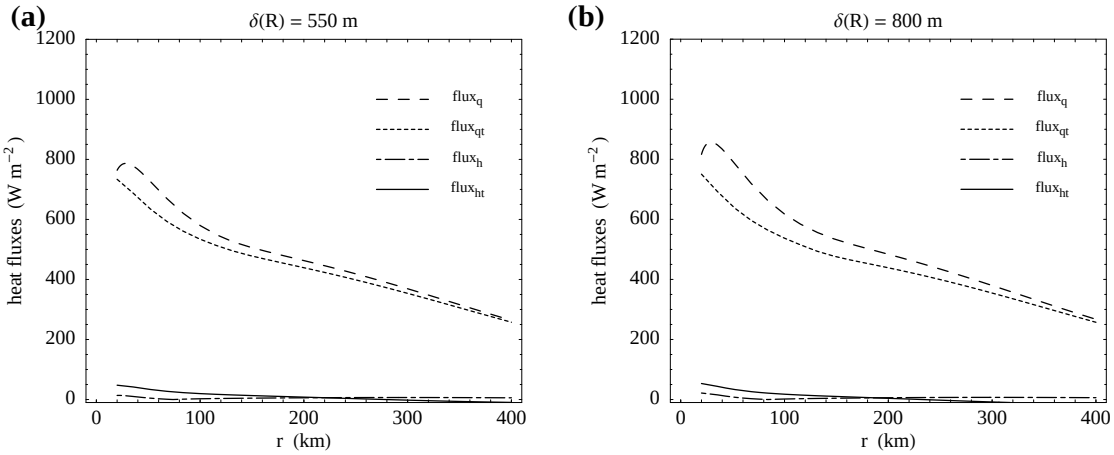

Figure 3.14: Latent and sensible heat fluxes from the sea surface (flux$_q$ and flux$_h$, respectively) and through the top of the boundary layer (flux$_{qt}$ and flux$_{ht}$) for radial varying boundary layer depth $\delta(r)$ where $\delta(R) = 550$ m, panel (a) and $\delta(R) = 800$ m, panel (b). All fluxes are given in W m^{-2}. Note that the sign of flux$_{ht}$ has been reversed for convenience of plotting.

3.3.3 The reversible equivalent potential temperature

A thermodynamic quantity of fundamental theoretical interest is the reversible equivalent potential temperature, θ_e. It has for example been used in developing a theory for the potential intensity of tropical cyclones (Emanuel 1986, 1988, 1995b, Bister and Emanuel 1998). For this reason we show in Fig.(3.16) the radial variation of θ_e for $\delta = \delta(r)$. The variation of $\delta(r)$ is here assumed to be the same as in the calculations discussed above. Now in Fig.(3.16), θ_{e1} and θ_{e2} label the curves for $\delta(R) = 550$ m, and $\delta(R)= 800$ m, respectively. In both calculations, θ_e increases with decreasing radius, while a deeper boundary layer leads to marginally lower values.

Recently Montgomery *et al.* (2006) and Bell and Montgomery (2007) presented observational data from the category five Hurricane "Isabel", (2003), including data on the radial increase of θ_e towards the centre. To be able to compare the predictions of this model with their observations two more calculations for the same boundary-layer depths were carried out, but with a maximum tangential wind speed of 70 m s^{-1}, which is more appropriate for a category five storm like Isabel. The two curves are also shown in Fig.(3.16) and they are labelled by θ_{e3} and θ_{e4}. These curves are for $\delta(R) = 550$ m (θ_{e3}), and $\delta(R) = 800$ m, (θ_{e4}), respectively. As expected θ_e reaches higher values than before but the difference between the calculations for the two values of δ is larger. For $\delta(R) = 550$ m and a maximum tangential wind speed of 70 m s^{-1}, θ_e, the solution

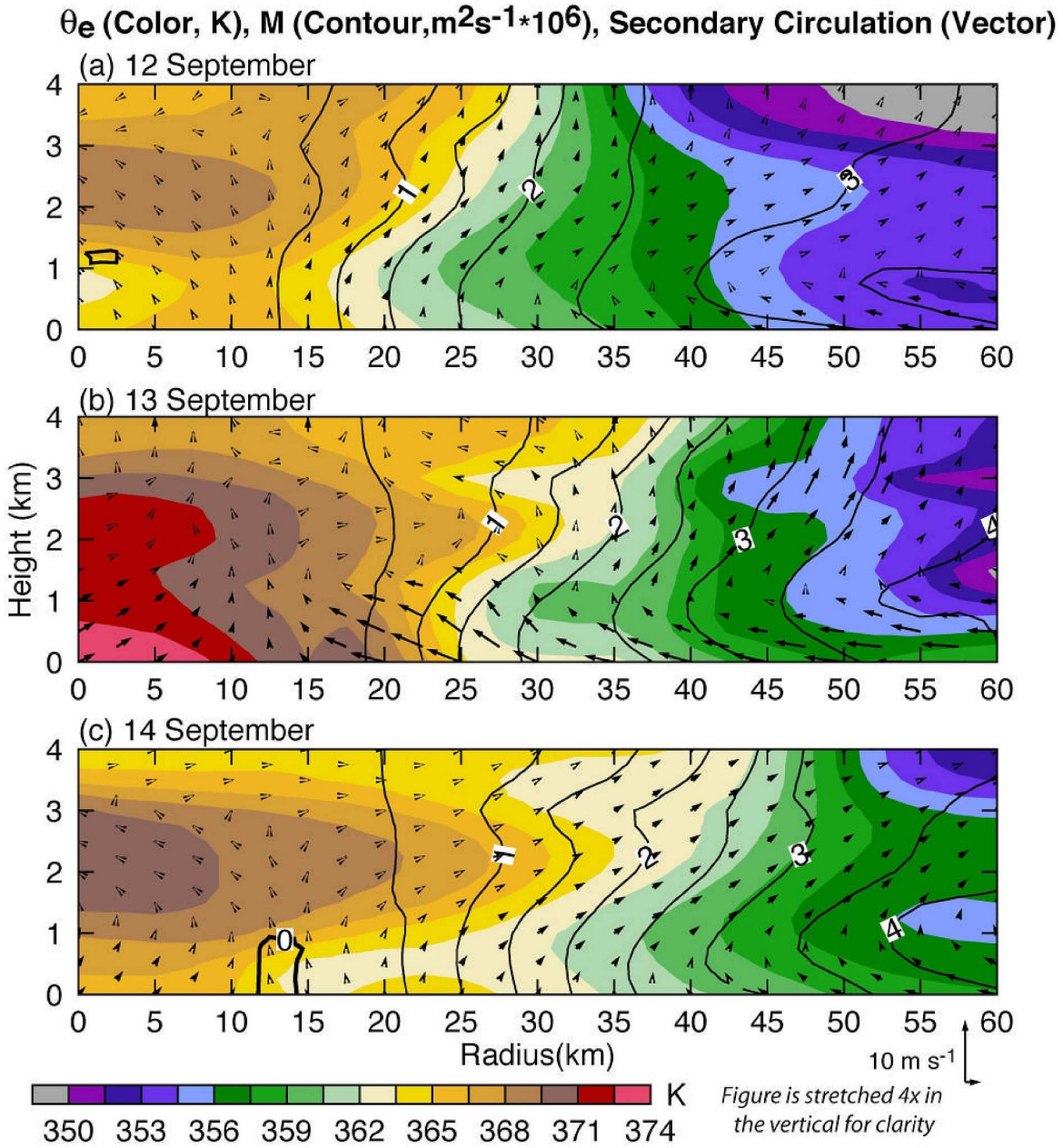

Figure 3.15: Radius-height azimuthal mean storm-relative θ_e (color, in Kelvin); absolute angular momentum (contour, m^2s^{-1} $\times 10^6$); and transverse secondary circulation (vector) from 12 - 14 (a - c) of September, 2003 (from Bell and Montgomery 2007).

breaks down for a radius of about 60 km. The solution up to this radius shows a steady increase in θ_e and it reaches finally a value of about 355 K at the radius, where the solution breaks down. This result is not improper if it is compared to the ones reported by Montgomery *et al.* (2006) in their Fig.(5) which is shown in Fig.(3.15).
When comparing the results it has also to be taken into account that the model presented here fixes the values of w_{sc} and q_{δ_+} and does not allow them to vary with varying radius as it would be realistic. If the concrete values are compared, it is seen that the general trend and range of values is in a quite good agreement. For example, on 12 September 2003 they found values of θ_e of about 353 K at radii between 50 and 60 km in the low-level inflow layer. On 13 September it was a value of up to 360 K (Figure (5) in their paper). It is also nicely seen that their values are rising steadily with decreasing radius. This is the same behavior as it is shown in the calculations with the model presented here until the solutions break down (see Fig.(3.16)). Montgomery *et al.* (2006) calculated their θ_e pseudo-adiabatically. Anyhow, at low levels in the boundary layer there is no liquid water and the pseudo-adiabatically calculated θ_e is essentially the same.

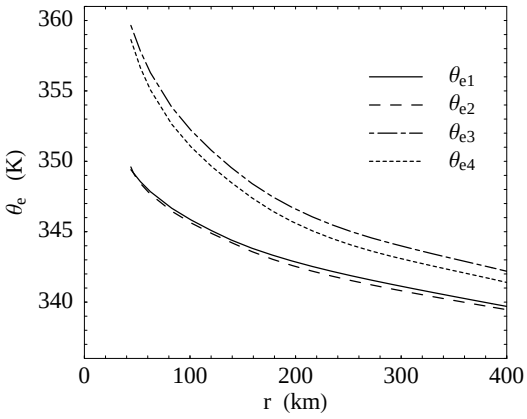

Figure 3.16: Radial profiles of reversible equivalent potential temperature θ_e (K) in the boundary-layer for a maximal wind speed of 40 m s^{-1} with $\delta = 550$ m (θ_{e1}) and $\delta = 800$ m (θ_{e2}) and calculated with a higher maximal wind speed of 70 m s^{-1} (θ_{e3} and θ_{e4}).

3.4 Discussion of the results

Many simple models of hurricanes use just a representation of the boundary layer as one single layer of fixed depth as it is discussed here. So the results presented here for the slab boundary layer model have certainly implications for the modeling of hurricanes in general. Of course one-layer models have their limitations and these should be borne in mind when interpreting the results of this study. Some important limitations are listed below together with certain issues that may be arising from the results.

One assumption in deriving the bulk equations is that the vertical average of terms such as those representing radial advection are equal to the radial advection computed from vertically averaged quantities. This assumption can be expected to be inaccurate if regions of strong outflow overlie regions of inflow. This may happen near the radius of maximum tangential wind speed in the continuous models (see e.g. Kepert and Wang 2001, Montgomery *et al.* 2001). The feature was also discussed in chapter (2), where the simple linear model was investigated in detail. However, here it was considered that the boundary layer is just the inflow layer itself. Therefore the inaccuracy mentioned above should be much less important.

Another important issue is that the prescription of a uniform depth with radius is a further limitation. It was discussed in section (3.2.6) that an elementary scale analysis suggests that the layer depth must decrease as the inertial stability increases. This fact is confirmed by many solutions where the depth is allowed to vary as in the linear model in chapter (2) or various examples in the literature as e.g. Smith (1968), Leslie and Smith (1970), Eliassen and Lystad (1977), Kepert (2001), Kepert and Wang (2001), Montgomery *et al.* (2001). However, it was shown in section (3.2.6) that this weakness of the slab model can be removed by introducing a radially varying boundary layer depth $\delta = \delta(r)$. If the boundary layer depth is calculated by

$$\delta(r) = \delta(R)\sqrt{(C_g/C)},$$

where $\delta(R)$ is the boundary layer depth at the starting radius R, C_g is the value of C at this radius and

$$C = (\zeta_{gr} + f)\left(\frac{2v_{gr}}{r} + f\right)$$

it is made sure that the radial variation of this quantity is in agreement with the results suggested by the scale analysis and is reflecting results from models that alllow the boundary layer depth to be calculated as e.g. the linear model presented before.

However, in reality the processes that are determining the boundary layer depth are much more complex. On the one hand at large radii far from the core region the turbulence which is generated in the boundary layer will act such that the boundary layer may be deepened. On the other hand there is subsidence aloft, a process which is acting to make it shallower. So a very delicate balance between this two processes is determining the final depth of the boundary layer in that region. In the inner core the situation is even more complicated. Here the air parcels are spiralling up and out of the boundary layer, a fact that is seen from the vertical wind profiles. This ascent is responsible for some vertical advection of turbulence which may be quite important. The boundary layer depth in the inner core may be influenced by this process also as e.g. suggested in Stull (1988). However it is not possible to represent those difficil processes in a simple one-layer model. It must be said that that the accuracy of the slab model in the core region may be reduced.

The consequences of prescribing the tangential wind speed, or equivalently the radial pressure gradient, above the boundary layer in the inner-core region, where the flow exits the boundary layer, are unclear. As the discussion of the linear model in chap.(2) showed it is probably just incorrect to prescribe v_{gr} just above the boundary layer in regions, where the air parcels are floating up and out of the layer.

Many previous boundary-layer models have taken this approach (e.g. Smith 1968, Leslie and Smith 1970, Bode and Smith 1975, Shapiro 1983, Kepert 2001, Kepert and Wang 2001, Smith 2003), but the consequences have not been investigated or discussed in detail.

In this region it would seem more reasonable to suppose that boundary-layer air carries its momentum with it as it ascends. This means in regions, where there is ascent the upper boundary must be treated as an outflow boundary and not as an inflow boundary as it is done by prescribing v_{gr}.

This argument is obviously having certain important consequences that have to be discussed more detailed. The fact that in regions of ascent there is an outflow boundary implies of course that the air parcels that are spiralling out of the layer are carrying their momentum $\rho(u_b, v_b)$ with them.

The assumption of an imposed profile of v_{gr} was tacitly made by Emanuel (1986). He formulated a steady state hurricane model with a very simple representation of

the boundary layer which is among others the basis of his well established potential intensity theory. In his model he assumed that the tangential flow just above the boundary layer v_{gr} is the same as that in the boundary layer v_b in regions of ascent and that gradient wind balance is satisfied. In his theory for potential intensity (Bister and Emanuel, 1998 and references therein) he made a very similiar assumption. Of course this implies that even in the boundary layer gradient wind balance must exist. Obviously in that case there would be no net force to drive the inflow. Thus it must be clearly argued that the inconsistency is arising from the assumption of gradient wind balance in the boundary layer. There is no reason to suppose that the tangential flow v_b should be in gradient wind balance as air parcels exit the boundary layer.

However in the slab model (u_b, v_b) are calculated as an average through the depth of the boundary layer and as such they have to interpreted. This implies that some differences between (u_b, v_b) in the boundary layer and the supposed values of the imposed gradient flow, $(0, v_{gr})$, at the top of the boundary layer could be tolerated. In the slab model it may be best to regard the prescribed profile of v_{gr} as nothing else than a prescription of the radial pressure gradient. This reduces the inconsistencies. The only place, where it would be a problem, is the assumption that the momentum fluxes at the top of the boundary layer which are associated with shallow convection or precipitation-driven downdraughts are proportional to $(0, v_{gr}) - (u_b, v_b)$. The consequence is that the slab model is much less constrained than models that allow for vertical structure as for example the linear continuous model presented before. In those models the air parcels that are leaving the boundary layer are subject to a prescribed pressure gradient. It is also the case that the model at the top of the boundary layer forces the radial and the tangential wind speed to the gradient values

$$(u(z), v(z)) \rightarrow (0, v_{gr}).$$

In that case z describes the vertical coordinate. Of course the foregoing discussion points towards some new interpretations of previous studies. For example Montgomery *et al.* (2001) presented full numerical solutions, where the boundary layer and the flow above were solved together. In that calculation they found an outflow jet above the inflow layer. Now the slab model provides a possibility to interpret that result. The mismatch between (u_b, v_b) and $(0, v_{gr})$ which has become obvious by the analysis of the slab model suggests that the outflow jet is just a means by which the flow exciting the boundary layer adjusts to the radial pressure gradient which is associated with

the profile of the vortex above. A consequence of that is, that for a more complete formulation of the steady boundary layer in the inner-core region of a hurricane a simple one-layer slab model is not enough. If a slab-type representation of the boundary layer shall be used it is at least necessary to distinguish two separate layers. The second one is obviously necessary to represent the outflow jet. Here it would be necessary that the radial and the tangential wind fields (u_b, v_b) could adjust to the radial pressure gradient. That pressure gradient would be implied by the mass distribution in the free troposphere.

Another issue is to interprete models that allow the boundary layer to have vertical structure particularly with regard to the findings emerging from the slab model. Especially the following discussion is of importance for the interpretation of the result of the linear model presented in chap.(2). Models that allow for vertical structure set in general (u_b, v_b) to $(0, v_{gr})$ at the top of the layer. However, this does not avoid the problem that the flow that exits the layer is unrealistically over-constrained.

For example, the solutions reported by Kepert and Wang (2001), their Fig.(2) show supergradient flow everywhere *above* the boundary layer. It is defined there by the region, where there are significant turbulence levels. In their model the supergradient flow is even found in regions, where turbulence levels are small and where there is no apparent radial or vertical motion. The reasons for these supergradient winds are hard to interpret in terms of the insights gained from the slab model, which requires strong inflow to achieve supergradient winds. That is not to say that Kepert and Wang's results are wrong, but they need to be understood. The solutions of Montgomery *et al.* (2001) do not need any constraints to be imposed at the top of the boundary layer. These calculations do not show a level above the boundary layer where the radial flow is zero everywhere. Even if the slab model provided new insights that were enlightening, the results of those models the problems mentioned above require further research.

A significant result emerging from the slab model is the ubiquitous tendency to produce supergradient winds. A well-known result from the inviscid axisymmetric balanced theory of vortex intensification is that the latent heat release in eye-wall convection tends to produce a secondary circulation. In that secondary circulation the tangential wind tendency is largest inside the radius of maximum tangential wind speed (Shapiro and Willoughby 1982). This means that the vortex contracts as it intensifies. If the boundary layer tends to generate supergradient tangential winds inside the radius of

maximum tangential wind speed above it and if these winds are advected vertically out of the boundary layer, they would contribute in a similar way to a spin up of the core region.

Such behavior is consistent with some unpublished calculations performed by a colleague, Wolfgang Ulrich. Using an axisymmetric tropical-cyclone model, he found that the ring of air corresponding with the maximum calculated tangential wind speed always originated at large radial distances in the boundary layer (Ulrich and Smith, 2004). The idea is supported also by the simple tropical-cyclone model examined by Emanuel (1997) in which the inner-core spin up appears to be orchestrated by the boundary layer. The veracity of these results would indicate that the boundary layer is a fundamental aspect of the spin-up of the inner-core of a tropical cyclone. This statement hold at least when an axisymmetric setup is investigated. However the major influence of the boundary layer for the intensification process is an important implication of the studies presented above.

Chapter 4

A critique of Potential Intensity theory

4.1 A review of Emanuel's (1986) hurricane model and potential intensity theory

The results obtained with a simple slab boundary layer model as discussed in chapter (3) (see also Smith 2003, Smith and Vogl 2008) led to a new interpretation of the processes in the boundary layer. In the following a critique of Emanuel's steady state hurricane model will be presented (Smith, Montgomery and Vogl 2008). Emanuel's steady state model is a forerunner to his theory for hurricane potential intensity.

It will be shown that a major deficiency of the theory is the tacit assumption of gradient wind balance in the boundary layer, a layer that owes its existence to *gradient wind imbalance* in the radial momentum equation. If a more complete boundary layer formulation is included, using the gradient wind profiles obtained from Emanuel's theory, the tangential wind speed in the boundary layer becomes supergradient, invalidating the assumption of gradient wind balance. It will be shown that the degree to which the tangential wind is supergradient depends on the assumed boundary layer depth. The full boundary-layer solutions require a knowledge of the tangential wind profile above the boundary layer in the outer region, where there is subsidence into the layer and they depend on the breadth of this profile. This effect is not considered in Emanuel's theory. It will be argued that a more complete theory for the steady state hurricane

would require the radial pressure gradient above the boundary layer to be prescribed or determined *independently* of the boundary layer.

The issues raised herein highlight a fundamental problem with Emanuel's theory for potential intensity, since that theory makes the same assumptions as in the steady state hurricane model. The current findings together with recent studies examining intense hurricanes suggest a way forward towards a more consistent theory for hurricane potential intensity.

In the first of what has turned out to be a series of very influential papers, Emanuel (1986, henceforth E86) presented a steady axisymmetric model for a mature hurricane. This paper was an important milestone in tropical cyclone research in that it re-focussed attention on the importance of the radial gradient of sea surface moisture fluxes in the storm-scale energetics. The hurricane model described therein was a prelude to the development of an axisymmetric theory for the potential intensity (PI) of a tropical cyclone, which will be refered to as EPI-Theory in the following discussion (Emanuel 1988, Emanuel 1995, Bister and Emanuel 1998). Since its inception, EPI-theory has been called upon by many researchers as a standard for comparison with the intensity attained in numerical models (e.g., Frank and Ritchie 2001, Persing and Montgomery 2003). It was also used for an assessment of possible changes in the intensity of hurricanes as a result of global warming (e.g., Knutson and Tuleya 2004, Emanuel 2005, Bengtsson *et al.* 2007). At the present time it appears to be the only such theory of merit for these applications (Camp and Montgomery 2001). Even so, there are indications that the theory is deficient. For example, Persing and Montgomery (2003) have shown that high-resolution numerical models have a tendency to produce "superintense" storms, superintense meaning that they significantly exceed the intensity predicted by EPI-theory. Moreover, the calculated potential intensity depends sensitively on the assumed relative humidity at the radius of maximum tangential wind speed, which Emanuel generally takes to be 80%.

In this chapter attention is especially drawn to a fundamental inconsistency of the hurricane model and of EPI-theory. This inonsistency is the assumption of gradient wind balance in the boundary layer, both inside and outside the radius of maximum tangential wind speed. The consequences of this assumption for Emanuel's hurricane model and EPI-theory are discussed below and a way forward is sketched.

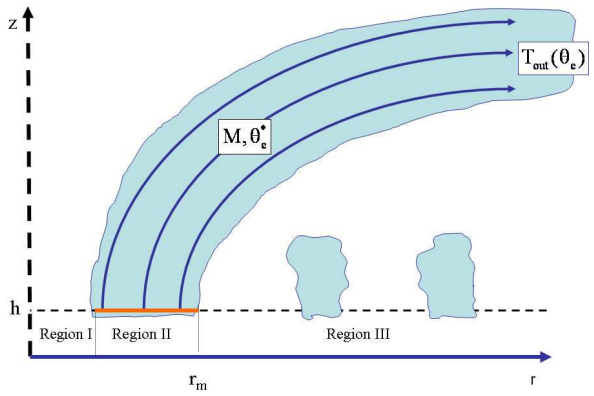

Figure 4.1: Schematic diagram of Emanuel's 1986 model for a mature hurricane. The boundary layer is assumed to have constant depth h and is divided into three regions as shown: the eye (Region I), the eyewall (Region II) and outside the eyewall (Region III), where spiral rainbands and shallow convection emanate into the vortex above. The absolute angular momentum per unit mass, M, and equivalent potential temperature, θ_e of an air parcel are conserved after the parcel leaves the boundary layer and ascends in the eyewall cloud. The precise values of these quantities depend on the radius at which the parcel exits the boundary layer. The model assumes that the radius of maximum tangential wind speed, r_m, is located at the outer edge of the eyewall cloud, whereas recent observations (e.g. Marks *et al.* 2008, Fig.(3)) indicate it is closer to the inner edge.

4.1.1 The E86 model in brief

In the E86 model, the hurricane vortex is assumed to be steady and circularly symmetric about its axis of rotation. The boundary layer is taken to have uniform depth, h, and is divided into three regions as shown in Fig.(4.1). Regions I and II encompass the eye and eyewall, respectively, while Region III refers to that beyond the radius, r_m, of maximum tangential wind speed, v_m, at the top of the boundary layer.

Contrary to Emanuel's assumption in this figure, observations show that r_m is located well inside the outer edge of the eyewall (e.g. Marks *et al.* 2008, Fig.(3)). The significance of this discrepancy will become clearer in section (4.3). E86 takes the outer radius of Region II to be r_m on the basis that precipitation-driven downdrafts can be important outside this radius. The tangential wind field above the boundary layer is assumed to be in thermal wind balance and air parcels flowing upwards and outwards into the upper troposphere are assumed to conserve their absolute angular momentum, M, and saturation moist entropy, s^* (calculated reversibly). These surfaces are assumed to flare out in the upper troposphere. Here, s^* is defined by:

$$s^* = c_p \ln {\theta_e}^*, \tag{4.1}$$

where θ_e^* is the reversible saturation equivalent potential temperature and c_p denotes the specific heat at constant pressure of dry air. Because the saturation vapor pressure of moist air is a unique function of temperature both s^* and θ_e^* are state variables. It is now shown in detail how E86 derives an equation for the tangential wind speed V at $z = h$ in Region II.

In pressure coordinates, the gradient wind equation and hydrostatic equation can be written as:

$$g\left(\frac{\partial z}{\partial r}\right)_p = \frac{M^2}{r^3} - \frac{1}{4}rf^2 \tag{4.2}$$

and

$$g\left(\frac{\partial z}{\partial p}\right)_r = -\alpha, \tag{4.3}$$

where α is the specific volume, p is the pressure, z is the height of a pressure surface and g is the acceleration due to gravity. Eliminating the geopotential height of the pressure surface, gz, gives an alternative form of the thermal wind equation:

$$\frac{1}{r^3}\left(\frac{\partial M^2}{\partial p}\right)_r = -\left(\frac{\partial \alpha}{\partial r}\right)_p. \tag{4.4}$$

Since s^* is a state variable, α can be regarded as a function of p and s^*. Then with a little manipulation Eq.(4.4) becomes the thermal wind equation:

$$\frac{1}{r^3}\left(\frac{\partial M^2}{\partial p}\right)_r = -\left(\frac{\partial \alpha}{\partial s*}\right)_p \left(\frac{\partial s^*}{\partial r}\right)_p. \tag{4.5}$$

E86 invokes one of the Maxwell relations for moist saturated air in the form

$$\left(\frac{\partial \alpha}{\partial s^*}\right)_p = \left(\frac{\partial T}{\partial p}\right)_{s*}, \tag{4.6}$$

so that Eq.(4.5) becomes

$$\frac{1}{r^3}\left(\frac{\partial M^2}{\partial p}\right)_r = -\left(\frac{\partial T}{\partial p}\right)_{s*} \left(\frac{\partial s^*}{\partial r}\right)_p. \tag{4.7}$$

With the assumption that M and s^* surfaces coincide, i.e. $M = M(s^*)$, Eq.(4.7) becomes

$$\frac{2M}{r^3}\left(\frac{\partial M}{\partial p}\right)_r = -\left(\frac{\partial T}{\partial p}\right)_{s*}\frac{ds^*}{dM}\left(\frac{\partial M}{\partial r}\right)_p. \tag{4.8}$$

Note that $(\partial T/\partial p)_{s*}$ is just the temperature lapse rate as a function of pressure along a moist adiabat. Now along a M surface,

$$\left(\frac{\partial M}{\partial r}\right)_p dr + \left(\frac{\partial M}{\partial p}\right)_r dp = 0, \tag{4.9}$$

so that the slope of a M surface in (r, p) space is

$$\left(\frac{dr}{dp}\right)_M = -\left(\frac{\partial M}{\partial p}\right)_r \Big/ \left(\frac{\partial M}{\partial r}\right)_p. \tag{4.10}$$

Combining Eq.(4.8) and (4.10), the thermal wind equation (Eq.(4.7)) becomes

$$\frac{1}{2}\left(\frac{dr^{-2}}{dp}\right)_M = -\frac{1}{2M}\left(\frac{\partial T}{\partial p}\right)_{s*}\frac{ds^*}{dM}, \tag{4.11}$$

which can be integrated upwards along the M (or s^*) surface starting from the top of the boundary layer $z = h$ to an outer radius r_{out} to give

$$\left.\frac{1}{r^2}\right|_M - \left.\frac{1}{r_{out}^2}\right|_M = -\frac{1}{M}\frac{ds^*}{dM}[T - T_{out}(s^*, p_{out})]. \tag{4.12}$$

Assuming that $r_{out} >> r$, and using the chain rule, Eq.(4.12) gives

$$-[T_B - T_{out}(s^*, p_{out})]\frac{\partial s^*}{\partial r} = \frac{1}{2r^2}\frac{\partial M^2}{\partial r}, \text{ at } z = h, \tag{4.13}$$

where T_B is the temperature at the top of the boundary layer and T_{out} is the outflow temperature along the M (or s^*) surface at r_{out}. Using the Exner function, $\pi = (p/p_o)^\kappa$, instead of pressure, the gradient wind equation (4.2) takes the form

$$M^2 = r^3\left[c_p T_B\left(\frac{\partial \ln \pi}{\partial r}\right)_z + \frac{1}{4}rf^2\right]. \tag{4.14}$$

In the expression for π, $\kappa = R/c_p$, where R is the specific gas constant and p_o is a constant pressure, taken by E86 to be 1015 hPa. Substituting Eq.(4.14) into (4.13) results in

$$-\frac{T_B - T_{out}(s^*, p_{out})}{T_B}\frac{\partial \ln \theta_e^*}{\partial r} = \frac{\partial \ln \pi}{\partial r} + \frac{1}{2}\frac{\partial}{\partial r}\left(r\frac{\partial \ln \pi}{\partial r}\right) + \frac{1}{2}\frac{r f^2}{c_p T_B}, \text{ at } z = h, \quad (4.15)$$

where it is assumed that $\theta_e = \theta_e^*$ at $z = h$. This equation is integrated with respect to radius from r to some large radius $r = r_o$, where it is assumed that $\ln(\pi/\pi_o)$ and its radial derivative vanish, π_o being the value of π at $z = h$ and $r = r_o$. Remembering that T_B is assumed to be constant, the result is:

$$-\ln \theta_{eo}^* + \ln \theta_e^* + \frac{1}{T_B}\int_r^{r_o} T_{out}(s^*, p_{out})\frac{\partial \ln \theta_e}{\partial r}dr =$$
$$\ln \pi_o - \ln \pi + \frac{1}{2}\left(r\frac{\partial \ln \pi}{\partial r}\right)_o - \frac{1}{2}\left(r\frac{\partial \ln \pi}{\partial r}\right) + \frac{1}{4}\frac{f^2}{c_p T_B}(r_o^2 - r^2), \text{ at } z = h. \quad (4.16)$$

Emanuel defines

$$\overline{T_{out}} = \frac{1}{\ln(\theta_e^*/\theta_{eo}^*)}\int_{\ln \theta_{eo}}^{\ln \theta_e^*} T_{out} d \ln \theta_e^*, \quad (4.17)$$

which is an average outflow temperature weighted with the saturation moist entropy of the outflow angular momentum surfaces. Remember that θ_e^* along angular momentum surfaces is taken equal to the equivalent potential temperature, θ_e, where the surfaces meet the top of the boundary layer. Then (4.13) gives Eq.(4.22).

It is at this point that boundary layer considerations are invoked. Assuming a slab boundary layer model with uniform depth as it will be described later in detail, E86 derives a further relationship between the specific moist entropy of the boundary layer, s, and M by effectively dividing Eq.(4.30) by Eq.(4.29). It has to be recognized here that the near-surface wind can be different from that at the top of the boundary layer. Thus following E86, but allowing for a reduced surface wind, it is

$$\left.\frac{ds^*}{dM}\right|_{z=h} = \left.\frac{\tau_s}{\tau_M}\right|_{z=0}, \quad (4.18)$$

where $\tau_s = -c_p C_k |\mathbf{V_s}|(\ln \theta_e - \ln \theta_{es}^*)$ and $\tau_M = -C_D |\mathbf{V_s}| r V_s$ are the surface fluxes of enthalpy and momentum expressed by standard aerodynamic formulae, and $|\mathbf{V_s}|$ is the magnitude of the near surface horizontal velocity.

Other quantities are defined in the following section (4.1.1).

In the derivation of Eq.(4.18) it is assumed that the specific entropy, s, and the equivalent potential temperature, θ_e, are uniform across the boundary layer and that the air at the top of the subcloud layer is saturated so that $s_b = s^*$ and $\theta_e = \theta_e^*$. This equation can then be blended with Eq.(4.12) above. Equation (4.13) then gives

$$\ln \theta_e^* = \ln \theta_{es}^* - \mu \frac{C_D}{C_k} \frac{1}{c_p(T_B - T_{out})} \left(V^2 + \frac{1}{2} r f V \right), \quad \text{at } z = h, \tag{4.19}$$

where M has been expressed in terms of the tangential wind speed V at $z = h$. In Region II, $rf << V$ so that the second term in parentheses on the right of Eq.(4.19) can be neglected compared with V^2 and the equation can be written as

$$\mu V^2 = \frac{C_k}{C_D} c_p (T_B - T_{out})(\ln \theta_{es}^* - \ln \theta_e^*), \quad \text{at } z = h, \tag{4.20}$$

where $\mu = V_s/V$. Equation (4.20) is a cornerstone of the current EPI-Theory (Emanuel 1995, Bister and Emanuel 1998).

A further important relationship in Emanuel's theory is that between θ_e^* and the pressure and humidity at the top of the surface layer, which can be written

$$\ln \frac{\theta_e^*}{\theta_{ea}^*} = -\ln \frac{\pi_s}{\pi_a} \left(1 + \frac{L q_a^* R H_s}{R T_s} \right) + \frac{L q_a^*}{R T_s} (RH - RH_a)_s, \quad \text{at } z = h, \tag{4.21}$$

where L is the latent heat of vaporization, q is the water vapor mixing ratio, RH is the relative humidity, and T is the absolute temperature. As above, a subscript 's' denotes a value at the top of the surface layer and a superscript '*' denotes a saturation value. This equation is the same as Eq.(25) in E86 if one assumes that the reference pressure in the definition of the Exner function is p_a rather than 1000 hPa as is usual.

So in brief E86 assumes the tangential wind field above the boundary layer to be in thermal wind balance. The air parcels are assumed to conserve their absolute angular momentum and their saturation moist entropy when they are spiralling up and outwards into the troposphere.

E86 then integrates the thermal wind equation upwards along these surfaces from radius r to some large radius r_{out} ($>> r$) to obtain a relationship between the radial rates of change of M and s^* at the top of the boundary layer, $z = h$ (see Eq.(4.13) above).

This equation can be further integrated with respect to radius to obtain a relationship between θ_e^* and the logarithm of the Exner function at the top of the boundary layer. If it is assumed that gradient wind balance holds it is at this height:

$$\frac{T_B - \bar{T}_{out}}{T_B} \ln\left(\frac{\theta_e^*}{\theta_{eo}^*}\right) = \ln\left(\frac{\pi_o}{\pi}\right) - \frac{1}{2}\left(r\frac{\partial \ln \pi}{\partial r}\right) + \frac{1}{4}\frac{f^2}{c_p T_B}(r_o^2 - r^2), \quad \text{at } z = h, \tag{4.22}$$

where T_B is the temperature at $z = h$, T_{out} is the temperature on the s^* surface at r_{out} and $\bar{T}_{out}$ is an average of this temperature weighted with the saturation moist entropy of the outflow angular momentum surfaces (see Eq.(4.17)). Moreover π is the Exner function, f is the Coriolis parameter and the subscript '$_o$' denotes a value at some large radius $r = r_o$.

The flow in Regions I and II is fully determined by a simple slab formulation for the boundary layer from which a second functional relationship is obtained between M and s^* (see Eq.(4.18)). The two relationships, Eqs.(4.13) and (4.18), lead *inter alia* to an expression for the tangential wind speed, V, at $z = h$ in Region II. In this region the Rossby number is large compared to unity and the Coriolis term can be neglected, giving

$$\mu V^2 = \frac{C_k}{C_D} c_p (T_B - T_{out})(\ln \theta_{es}^* - \ln \theta_e^*), \quad \text{at } z = h, \tag{4.23}$$

where θ_{es}^* is the saturation equivalent potential temperature at the sea surface temperature, C_k and C_D are sea surface exchange coefficients for enthalpy and momentum, and $\mu = V_s/V$, where V_s is the magnitude of the near surface wind. Equation (4.23) states that in Region II, V is determined locally by the thermodynamic disequilibrium between the air in the boundary layer and the sea surface and the temperature difference between the top of the boundary layer and the outflow temperature.

E86's boundary layer formulation in Regions I and II expresses a balance between radial advection and surface gain or loss of azimuthal momentum and specific entropy. In the derivation of (4.23), the radial velocity is eliminated so that the formula for V^2 is not explicitly dependent on the radial component of velocity in the boundary layer.

Equations (4.22) and (4.23) lead essentially to an expression for the pressure as a function of radius (actually the logarithm of the Exner function) at the top of the boundary layer in Regions I and II (see E86, Eqs.(41) and (45)).

On the basis that precipitation-driven downdrafts tend to offset the moistening of inflowing boundary layer parcels in Region III, Emanuel assumes that the relative humidity at the top of the surface layer has a constant value of 80% all the way inwards to r_m, an assumption that is not borne out by observations (see e.g. Fig.(4d) of Montgomery *et al.* 2006).

These assumptions lead to a second equation relating the equivalent potential temperature to the logarithm of the Exner function and the relative humidity at the top of the surface layer (see Eq.(4.21)). This equation, when combined with Eq.(4.22) gives an expression for the logarithm of the Exner function at $z = h$ in Region III (E86, Eq.(39)). With the assumption of gradient wind balance at $z = h$, the resulting two equations for pressure and $\theta_e^*(z = h)$ completely determine the tangential wind speed at the top of the boundary layer at all radii.

Note that the tangential wind speed at the top of Region III is obtained only from thermodynamic considerations in the boundary layer: the dynamics of the boundary layer are completely ignored. It will be argued below that the tacit assumption of gradient wind balance in the boundary layer in Regions I and II and the neglect of boundary-layer dynamics in Region III represent a fundamental limitation of Emanuel's theory and leads to an inconsistency with important ramifications.

4.1.2 The slab boundary layer model

To put E86's assumptions regarding the boundary layer in perspective the slab boundary layer model which is discussed in detail in chapter (3) can be used. It is a more complete model of the boundary layer of a steady axisymmetric hurricane-like vortex on an f-plane as the one used by Emanuel (1986). With that model the consequences of assuming gradient wind balance in the boundary layer can be discussed in detail.

The boundary layer is assumed to have uniform depth, h, and constant density, following Chapter (3). In fact in Chapter (3) also the variable depth case was considered, but for simplicity the focus now is on the constant depth boundary layer assumed by E86.

In a cylindrical coordinate system (r, ϕ, z), the vertically-integrated equations expressing the local budgets of radial momentum, azimuthal momentum, heat or moisture, and mass continuity can be written in the following form:

$$u_b\frac{du_b}{dr} = \frac{w_{h-}+w_{sc}}{h}u_b - \frac{(v_{gr}^2-v_b^2)}{r} - f(v_{gr}-v_b) - \frac{C_D}{h}(u_b^2+v_b^2)^{\frac{1}{2}}u_b, \quad (4.24)$$

$$u_b\frac{dv_b}{dr} = \frac{w_{h-}+w_{sc}}{h}(v_b-v_{gr}) - (\frac{v_b}{r}+f)u_b - \frac{C_D}{h}(u_b^2+v_b^2)^{\frac{1}{2}}v_b, \quad (4.25)$$

$$u_b\frac{d\chi_b}{dr} = \frac{w_{h-}+w_{sc}}{h}(\chi_b-\chi_{h+}) + \frac{C_\chi}{h}(u_b^2+v_b^2)^{\frac{1}{2}}(\chi_s-\chi_b) - \dot{\chi}_b, \quad (4.26)$$

$$\frac{du_b}{dr} = -\frac{u_b}{r} - \frac{w_h}{h}, \quad (4.27)$$

where u_b and v_b are the radial and azimuthal components of wind speed in the boundary layer, $v_{gr}(r)$ and w_h are the tangential wind speed and vertical velocity at the top of the boundary layer, $w_{h-} = \frac{1}{2}(w_h - |w_h|)$. Furthermore χ_b is a scalar quantity, which could be the dry static energy, the specific humidity, or the specific entropy, f is the Coriolis parameter, C_D is the surface drag coefficient, C_χ is the surface transfer coefficient for χ_b, χ_{h+} is the value of χ just above the boundary layer, and χ_s is the value of χ at the sea surface.

The terms involving w_{sc} represent turbulent fluxes at the top of the boundary layer. These could come from rainbands, shallow convection, or smaller-scale turbulent structures. The term $\dot{\chi}_b$ represents the effects of radiative cooling and dissipative heating when χ_b is taken to be the dry static energy. Consistent with the slab boundary layer formulation, the quantities u_b, v_b and χ_b are assumed to be independent of depth as they are averaged over the deth of the layer by integration.

Note that w_{h-} is nonzero only when $w_h < 0$, in which case it is equal to w_h. Thus the terms involving w_{h-} represent the transport of properties from above the boundary layer that can be different from those inside the boundary layer. For the calculations presented in sections (4.2.1) and (4.2.2) C_D is taken to be a constant. This constant is chosen equal to 2.0×10^{-3} which is the value that was used by E86.

For those in section (4.2.2), chapter (3) is the reference. There it was chosen $C_D = C_{D0} + C_{D1}|\mathbf{u_b}|$, where $C_{D0} = 0.7 \times 10^{-3}$ and $C_{D1} = 6.5 \times 10^{-5}$ for wind speeds less than 20 $\mathrm{m\,s^{-1}}$ and $C_D = 2.0 \times 10^{-3}$, a constant, for larger wind speeds. As already mentioned before, these values are based on the interpretation of Fig.(5) from Black *et al.* (2007). In the calculations described in Section (4.2), only dynamical effects are considered. This implies that a value for C_χ is not required.

As detailed in chapter (3) substitution of Eq.(4.27) into Eq.(4.24) gives an expression

for w_h:

$$w_h = \frac{h}{1+\alpha}\left[\frac{1}{u_b}\left(\frac{(v_{gr}^2 - v_b^2)}{r} + f(v_{gr} - v_b) + \frac{C_D}{h}(u_b^2 + v_b^2)^{\frac{1}{2}}u_b\right) - \frac{u_b}{r}\right]. \tag{4.28}$$

Note that α is zero if the expression in square brackets is positive and unity if it is negative. With this expression for w_h, Eqs.(4.24) - (4.28) form a system of ordinary differential equations that can be integrated radially inwards from some large radius R to find u_b, v_b and χ_b as functions of r, if values of these quantities at $r = R$ as well as the radial profile $v_{gr}(r)$ are given. The detailed description of the calculations and the complete results are presented in chapter (3).

4.1.3 E86's approximations for the boundary-layer

Emanuel writes Eq.(4.25) in terms of the absolute angular momentum in the boundary layer, $M_b = rv_b + \frac{1}{2}fr^2$, and approximates this equation in Region II, where $w_h > 0$, as

$$u_b\frac{dM_b}{dr} = -\frac{C_D}{h}rv_b^2. \tag{4.29}$$

In Eq.(4.29) the boundary layer depth $\delta = h$ and it is assumed that $w_{sc} = 0$ and that $u_b << v_b$ in the drag term. Note that in general, *knowledge of u_b is required for the determination of M_b*. However, Emanuel does not use the radial momentum equation to determine u_b, as his main focus is to obtain an expression relating the specific entropy, s_b, to M_b (see Eq.(4.18)). In fact, E86 uses Eq.(4.29) to determine u_b having obtained the radial pressure distribution through his Eqs.(39) and (41) and having assumed gradient wind balance to obtain v_b.

In the region, where $w_h > 0$ the equation for the specific entropy is:

$$u_b\frac{ds_b}{dr} = \frac{C_k}{h}v_b(s_s^* - s_b), \tag{4.30}$$

where s_s^* is the saturation specific humidity at the sea surface and again it is assumed that $w_{sc} = 0$. Furthermore the total wind speed has been approximated by the tangential wind speed.

E86's assumption that air leaving the boundary layer conserves its absolute angular momentum implies that $v_{gr} = v_b$, where $w_h > 0$. The assumption that v_{gr} is in gradient wind balance also implies that v_b is in gradient wind balance. This is a rather strong

assumption for the boundary layer in the inner core of a rapidly-rotating vortex and although it has been made by previous authors (e.g. Ooyama 1969), it is not known that there would be any rigorous justification for it. In fact it is not supported by a scale analysis of the boundary-layer equations (see chap.(2)). Ooyama was certainly aware of the limitations of the assumption and wrote in an unpublished manuscript in 1968

" ... it appears that the weakest hypothesis in [his] original model is the use of the balance approximation in the boundary layer".

In this manuscript, Ooyama went on to show that the solutions in a calculation with a more complete boundary layer formulation were more realistic than those with a balanced boundary-layer formulation. Indeed it is precisely the lack of gradient wind balance in the boundary layer that gives rise to the "frictionally-driven" inflow in the layer.

While inflow is theoretically possible in a boundary layer that is in approximate gradient wind balance, the balance assumption can be justified only if the radial acceleration and radial friction terms are small compared with the radial pressure gradient and the sum of the centrifugal and Coriolis forces. In such a "balanced" formulation, the radial flow is determined by the (*sic*) tangential momentum equation. With Emanuel's assumption that the total wind speed in the friction term in Eq.(4.25) can be reasonably approximated by v_{gr}, the equation predicts that

$$u_b = -cv_{gr}, \tag{4.31}$$

where $c = C_d v_{gr}/(h\zeta_a)$, and $\zeta_a = \zeta + f$ and ζ are the absolute vorticity and relative vorticity of the gradient wind, v_{gr}, respectively. Other processes could contribute also to radial motion in a boundary layer that is closely in gradient wind balance. One example is a radial buoyancy gradient above the boundary layer associated with moist convective processes (see e.g. Smith 2000, Smith *et al.* 2005).

In the next section solutions of the dynamical component of the full boundary layer equations as shown in section (4.1.2) are examined. The solutions are obtained with the gradient wind speed v_{gr} which was used by E86. It will be shown that these solutions are incompatible with the assumption in the E86 model that $v_{gr} = v_b$ where $w_h > 0$. Further it will be shown that the lack of any dynamical constraint in the boundary layer in Region III other than the tacit assumption of gradient wind balance is another

major deficiency of the theory.

4.2 Calculations

4.2.1 The E86 gradient wind profile

Figure (4.2) shows calculations of the full boundary layer equations of section (4.1.2), taking the gradient wind speed profile $v_{gr}(r)$ and other parameters the same as those obtained by E86. In particular $f = 6.83 \times 10^{-5}$ s^{-1}, corresponding with a latitude of $28^o N$, $h = 1000$ m, $C_D = 2.0 \times 10^{-3}$, $T_s = 27^o$ C, $T_B = 27^o$ C and $\bar{T}_{out} = -67^o$ C.

The radial profile of v_{gr} is obtained by solving the gradient wind equation with the pressure profile derived from the coupled expressions for $\ln \pi$ and ${\theta_e}^*$ in E86, namely Eqs.(39) and (41), using the parameter values detailed in that paper.

The integration in the full boundary layer calculation starts at a radius of 375 km, where the gradient wind speed (only 1.73 m s^{-1}) is small enough to justify the neglect of the nonlinear acceleration terms in the equations (see Smith 2003, Section 4). Note that beyond a radius of 400 km, the tangential wind in Emanuel's calculation is anticyclonic and just inside this radius, at about 396 km, the profile is inertially-unstable.

Figure (4.2), panel(a), compares the full solution for the tangential wind speed in the boundary layer, v_b, with the imposed gradient wind speed v_{gr}. It compares also the full solution for the radial wind speed, u_b, with that obtained from Eq.(4.31) based on the balance assumption that $v_{gr} = v_b$ as made by E86, and assuming that $w_{sc} = 0$. The balanced solution for u_b is marked as u_E and that for the corresponding vertical motion at the top of the boundary layer as w_E. The latter is calculated numerically from the continuity equation (4.27). The profiles of vertical velocity at the top of the boundary layer in the full solution, w_h, is compared with that in the balanced solution in Fig.(4.2), panel(b). It is worth noting at this point that this balanced solution agrees closely with that shown by E86 in his Fig.(12).

In the full and balanced calculations, the radial wind component increases inwards to a certain radius and then decreases. However, there are significant quantitative differences in the profiles. In the balanced solution, the maximum inflow of about 12 m s^{-1} occurs at a comparatively large radius (130 km), while in the full solution it

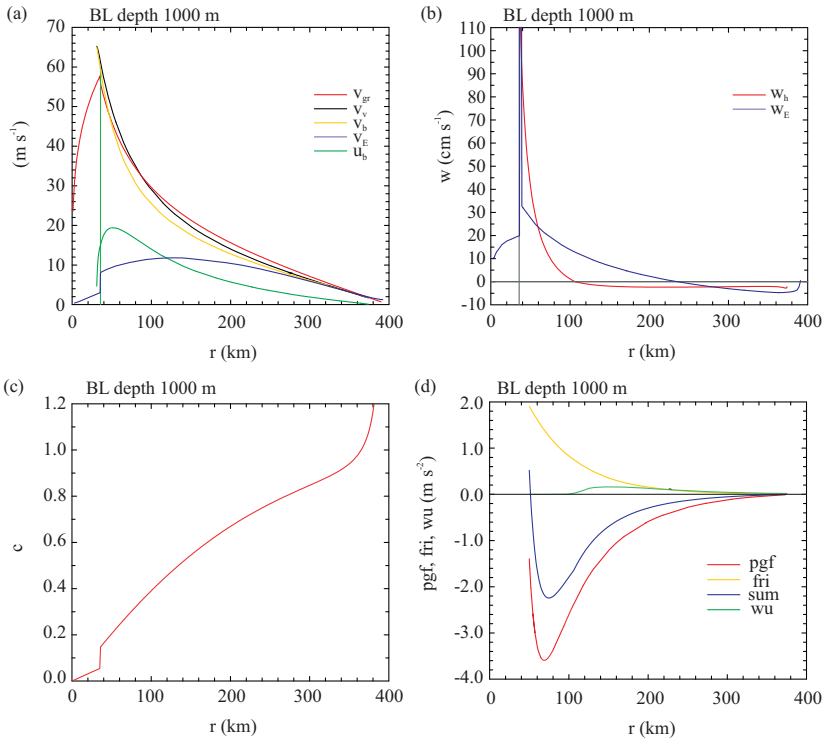

Figure 4.2: (a) Radial profiles of boundary layer radial (u_b) and tangential (v_b) wind components and the total wind speed $\sqrt{({u_b}^2 + {v_b}^2)}$ (denoted vv) from the full boundary layer solution, and the tangential wind speed above the boundary layer (v_{gr}) as obtained by E86 (solid curve). Shown also is the radial flow obtained from the balanced solution determined from Eq.(4.31) and denoted by u_E. For plotting convenience the signs of u_b and u_E have been reversed. (b) Corresponding radial profiles of vertical velocity at the top of the boundary layer (w_h) and that in the balanced solution (w_E). The thin vertical line in (a) and (b) marks the radius of maximum v_{gr}, the boundary between Regions II and III in Fig.(4.1). (c) Radial profiles of the coefficient c in Eq.(4.31). (d) Radial profiles of the three terms on the right-hand-side of the radial momentum equation, Eq.(4.24), and their sum (the solid line) for the full solution. The designation "wu", "nif" and "fri" refer to the first, second and third terms in the equation representing the downward advection of radial momentum, the net inward force and the frictional force, respectively.

occurs at 52 km, a little outside the radius of maximum gradient wind speed (35.8 km). These differences occur despite the fact that beyond 100 km in radius, v_b is at most 18% smaller than v_{gr}. This shows impressively that the degree of gradient wind imbalance is important. The decline in u_E from such a large radius is a result of the decline in the parameter c with decreasing radius (Fig.(4.2), panel(c)), which is larger than the rate at which v_{gr} increases. The discontinuity in u_E at $r = r_m$ is a result of the discontinuity of the relative vorticity ζ at this radius, which leads to a discontinuity in c. As expected there are correspondingly large differences in the profiles of vertical velocity at the top of the boundary layer (panel (b)). In particular, the change from descent at large radii to ascent at small radii occurs at a much smaller radius in the full calculation: 107 km compared with 230 km.

Of particular significance is the difference between v_b and v_{gr} in the inner core region, near the radius of maximum gradient wind speed. Here the tangential wind in the boundary layer becomes supergradient (i.e. v_b exceeds v_{gr}), which is incompatible with Emanuel's assumption that v_{gr} is equal to v_b at radii where $w_h > 0$. In other words, *Emanuel's calculated potential intensity* (i.e. v_m) *is exceeded when a more complete boundary layer formulation is used*. The occurrence of supergradient winds is a reflection of the strong radial inflow which advects absolute angular momentum at a rate larger than it can be removed locally by the frictional torque (Smith and Vogl 2008). As soon as the tangential wind speed becomes supergradient, all forces in the radial momentum equation act outwards and lead to a rapid deceleration of the inflow. In the full boundary-layer solution, the radial flow becomes zero at some finite radius and the boundary-layer model becomes singular at this radius. In reality one would expect the inflow to be expelled upwards before this radius, carrying its horizontal momentum with it. If the upflow remains out of balance one would expect it to flow outwards immediately above the inflow layer, a behaviour which is shown by full numerical solutions (e.g. Montgomery *et al.* 2001, Figs.(3c), (6c), Persing and Montgomery, Fig.(1b)).

Panel (d) of Fig.(4.2) shows the radial variation of the force terms in the radial momentum equation, Eq.(4.24). The term representing the downward transport of radial momentum, that proportional to w_{h-}, is non-zero only in the outer region and is small compared with the other terms. At larger radii, the net *inward* force (the difference between the inward pressure gradient and outward centrifugal and Coriolis forces) is

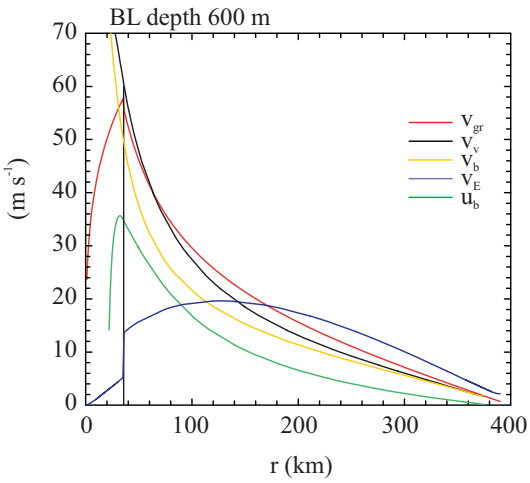

Figure 4.3: Legend as for Fig.(4.2)a, but for a boundary layer depth of 600 m.

larger in magnitude than the outward frictional force. Moreover, the inward radial acceleration, which is equal to the net *total* radially-inward force, is particularly large at radii less than 150 km.

4.2.2 Dependence on boundary layer depth

The boundary-layer constraint in Emanuel's theory is independent of the assumed boundary-layer depth. Note that the depth cancels in applying E86's boundary layer formulation to derive Eq.(4.18). However, this depth has a significant influence on the full boundary-layer solution because the effective drag in the boundary later is inversely proportional to the depth (Smith and Vogl 2008). For this reason the foregoing boundary-layer calculations were repeated for a boundary-layer depth of 600 m. The results of these calculations are shown in Fig.(4.3).

The increased effective friction leads to a larger reduction of the tangential wind speed in the boundary layer than in the earlier calculation and therefore to a larger net inward force and a larger inward acceleration. Consequently the maximum inflow is considerably larger than before (36 $\mathrm{m\,s^{-1}}$ instead of 19 $\mathrm{m\,s^{-1}}$) and occurs at a smaller radius (32 km instead of 52 km). On the other hand, the balanced solution changes only in magnitude and not in shape, whereupon the maximum occurs at 130 km as before. This result follows directly from Eq.(4.31) because the decreased depth simply increases the coefficient c by a constant factor at all radii and the gradient wind profile is the same. The fact that the maximum tangential wind speed in the boundary layer

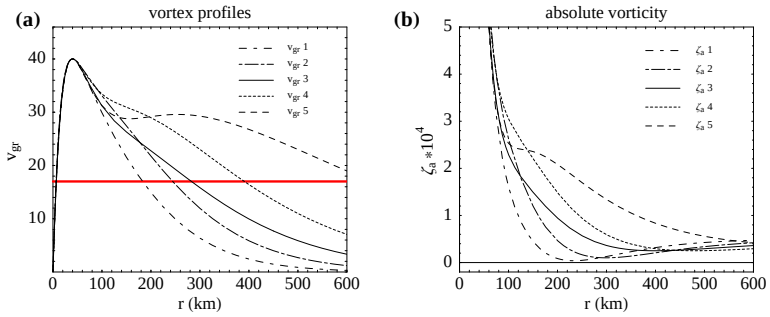

Figure 4.4: Radial profiles of tangential wind speed, $v_{gr}(r)$, at the top of the boundary layer used for the calculations shown in Fig.(4.5), panel(a), and their absolute vorticity ζ_a, panel (b). The red horizontal line in panel (a) indicates the radius of gale force winds (17 $\mathrm{m\,s^{-1}}$).

in this calculation is considerably higher than in the previous one implies that the potential intensity of the steady vortex is sensitive to the boundary layer depth, an important point not emphasized in E86 and his subsequent papers. Whereas the E86 model and the more complete boundary layer model furnish nonnegligible but modest differences in the maximum tangential wind (∼10-20%), it should be remembered that the boundary layer model used here precludes any thermodynamic and dynamic feedbacks between the boundary layer and interior flow. For several reasons, this feedback is thought to be quantitatively significant. The topic will be discussed in detail later.

Dependence on vortex size

As it was shown above the radial acceleration in the boundary layer is of major importance. Keeping that in mind, the inclusion of boundary-layer dynamics in Region III of Emanuel's model can be expected to have important consequences for the tangential wind maximum also. These consequences are demonstrated by a third set of calculations to emphasize the dependence of the maximum boundary-layer wind speed on the vortex size. The calculations presented below are based on solutions of the full boundary layer equations with the different profiles of gradient wind speed shown in Fig.(4.4).

These profiles are described in detail in the Appendix and are inertially stable. The solutions for the five vortex profiles are shown in Fig.(4.5) for a boundary layer depth of 800 m, a radially-varying drag coeffcient C_D and with $w_{sc} = -5.7$ $\mathrm{cm\,s^{-1}}$, the value used in chapter (3).

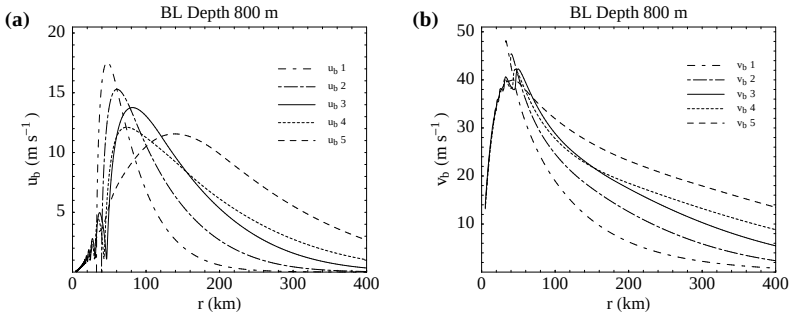

Figure 4.5: Radial profiles of the (a) *radially-inward* and (b) the tangential components of wind speed in the boundary layer for the four vortex profiles shown in Fig. 4.4 for a boundary layer depth of 800 m.

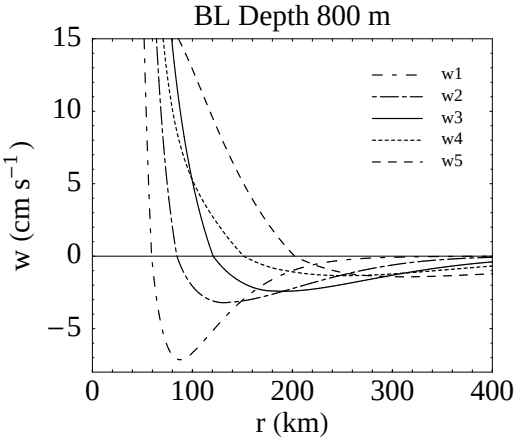

Figure 4.6: Vertical velocity w in cm s^{-1} for the five different wind profiles.

Note that there is a clear dependence of the solution on storm size, as might be characterized, for example, by the radius of gale-force winds (17 m s^{-1}) above the boundary layer. As the storm size decreases, the radius of maximum inflow is moving inwards and the maximum inflow is becoming larger. Moreover, the radius at which the vertical velocity changes sign decreases. This is highlighted in Fig.(4.6).

While for vortex profile 1 the area, where the air parcels are swirling up and out of the boundary layer, covers only a region inside a radius about 60 km, this changes dramatically for profile 5, where w is positive for all radii larger that 200 km.

To the extent that the intensity is controlled by boundary-layer dynamics, these solutions show a clear dependence on the size of the outer circulation so that the potential intensity of midget storms can be expected to be different from that of broad storms. These solutions highlight the dependence of the flow at all radii in the boundary layer

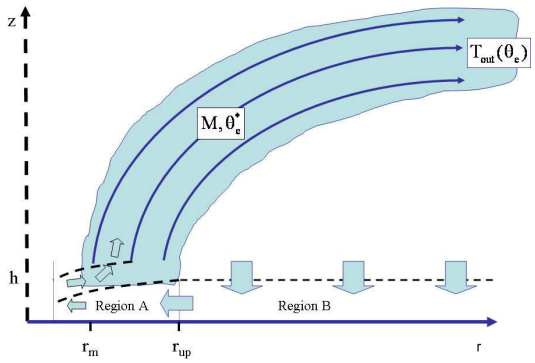

Figure 4.7: Modified conceptual model of the hurricane inner-core region motivated by the findings herein together with recent observational and modeling studies. Air subsides into the boundary layer for $r > r_{up}$ and ascends out of the boundary layer for $r < r_{up}$. The frictionally-induced net pressure gradient in the outer region produces a radially inward jet at $r = r_{up}$. The subsequent evolution of this jet depends on the bulk radial pressure gradient that can be sustained by the mass distribution at the top of the boundary layer. The jet eventually generates supergradient tangential winds whereafter the radial flow rapidly decelerates and turns upwards and outwards. When the outflow has adjusted to the radial pressure gradient that is sustained by the mass field, the flow turns upwards into the eyewall clouds.

on the size of the vortex above.

4.3 Discussion

Using the gradient wind profile predicted by Emanuel's steady state hurricane model in conjunction with a more complete formulation of the boundary layer generally leads to the occurrence of supergradient winds in the boundary layer in the high wind region of the vortex. These are incompatible with a key assumption in Emanuel's derivation of the gradient wind profile that requires it to be equal to that in the boundary layer, where the flow is upwards out of the boundary layer. Moreover, the degree to which the boundary layer winds are supergradient increases as the boundary layer depth decreases. In reality, the vertical advection of the supergradient winds out of the boundary layer would lead to outflow until a radius is achieved at which the pressure gradient is matched to that which can be sustained by the mass distribution. Of course, this effect cannot be captured by a one layer model, but, it is significant that calculations in which the boundary layer is allowed to adjust to an outer flow do show such behaviour (e.g. Montgomery *et al.* 2001, Figs.(3)c, (6)c, Persing and Montgomery 2003, Fig.(1)b).

The dependence of the radius at which subsidence at large radii changes to ascent, r_{up}, as well as the predicted radial profiles of u_b, v_b and w_h on the tangential wind profile above the boundary layer, where there is subsidence into it, shows that the dynamics of the boundary layer in Region III of Fig.(4.1) cannot be ignored.

The foregoing considerations suggest an alternative subdivision of the boundary layer to that in Fig.(4.1). This alternative is sketched in Fig.(4.7) and is based on whether the top of the boundary layer is an inflow boundary (Region B, $r > r_{up}$) or an outflow boundary (Region A, $r < r_{up}$).

In Region B the boundary layer is directly influenced by the vortex above through the radial pressure gradient at the top of the layer and through the downward advection of free vortex properties such as moisture, heat and momentum. Except possibly through the occurrence of moist convection, there is no essential feedback to the free vortex.

An important exception arises with the occurence of spiral rainbands and the corresponding formation of one or more secondary eyewalls (Houze *et al.* 2007, Terwey and Montgomery 2008). These asymmetric processes, their coupling to the boundary layer and the free axisymmetric vortex are not yet well understood and consequently lie beyond the scope of the present model.

However, in Region A, boundary layer properties are advected into the free vortex and have a profound influence on its structure. One can think of the boundary layer flow in Region B as producing an inward radial jet at $r = r_{up}$. The strength of this jet depends on the gradient wind profile at larger radii as well as the boundary-layer depth. The boundary layer dynamics in Region A determine the fate of this jet, but the details depend *inter alia* on the radial pressure gradient at the top of the boundary layer. This means that there is a substantial two-way feedback between the boundary layer and the free vortex in this region. These details depend also on the boundary layer depth. The radial pressure gradient in the boundary layer is probably still determined in large measure by the mass distribution in the free vortex, with possible exceptions in localized regions near, where inflow turns to upflow and possibly outflow (see below). However the free vortex can be expected to be strongly influenced by the radial distribution of mass, momentum and moisture that leave the boundary layer.

The foregoing calculations described here, supported by those of chapter (3), show that the tangential winds tend to become supergradient in the inner core.

As a result, the radial flow rapidly decelerates until the tangential component becomes subgradient again, or the radial wind becomes zero. This is of course a point at which the boundary layer equations in a one layer model become singular and a more sophisticated technique beyond the scope of this study is required for matching the solutions inside and outside this radius. In either case the flow out of the boundary layer increases markedly. If the winds carried upwards retain their supergradient character they will surely flow with a significant component outwards until they have come into gradient wind adjustment with the mass field aloft. At this point they would be expected to turn upwards into the eyewall. While parts of this scenario are speculative at this stage, the foregoing ideas would explain the observations of a skirt of moderate to high radar reflectivity adjacent to the main eyewall (e.g. Aberson *et al.* 2006, Figs. (5)-(7); Marks *et al.* 2008, Fig.(3)) but still within the 'visible' eye defined by the upper-tropospheric boundary of clear and cloudy air seen in high resolution satellite images (e.g. Bell and Montgomery 2008, Fig.(2)) and they are consistent with the calculations of Montgomery *et al.* (2001), (Fig.(3)c, (6)c) and Persing and Montgomery (2003), Fig.(1)b.

Within the context of the axisymmetric model the thermodynamic consequences of the overshoot/adjustment region have been demonstrated to be nontrivial as moist air near the surface and interior to the maximum tangential wind (including the outer part of the 'eye') can be drawn into the main eyewall above the shallow inflow layer. This low-level air generally possesses higher equivalent potential temperature than air found at the radius of maximum wind due to a lower surface pressure and nonzero surface winds and contributes additional heat and local buoyancy to the eyewall (Persing and Montgomery 2003, Cram *et al.* 2007). The net result is an enhancement of the radial gradient of equivalent potential temperature above the inflow layer that supports strong tangential winds in accordance with axisymmetric thermal wind balance above the boundary layer (Montgomery *et al.* 2006). In the light of these findings, together with the recognition that shear instability and coherent vortex sub-structures bordering the eye and eyewall will contribute to the aforementioned adjustment process (Schubert *et al.* 1999, Montgomery *et al.* 2002, Braun *et al.* 2006), it can be concluded that both the initial vortex structure and interactions between the eye and eyewall region are important elements of intense storms and should be accounted for in hurricane intensity theory.

Conclusions

In this work, different models of the hurricane boundary layer were investigated.

The adequacy of the well-known Ekman equations for describing the boundary layer flow in a hurricane was examined. Typical features of the flow in a hurricane are known to be:

- the turning of the wind vector with height as visualized by hodographs;
- there is a secondary circulation, which means in this case that there is a low-level jet towards the storm center and in a layer aloft, there is outflow;
- close to the ground a maximum in the tangential flow is found. This means that the winds inside the boundary layer are actually spinning faster than the winds in the free atmosphere, assuming that the flow above the boundary layer is in gradient wind balance.

Although the Ekman eqations were shown to be appropriate only in regions with a small Rossby number, as the regions far from the storm center, it was demonstrated that they describe qualitatively the main features of the boundary layer of a tropical cyclone. The solutions for the radial flow showed the effect of inflow close to the ground level and also the region of outflow above. Together with the downwards motion at large radii and the upwards motion at small radii the secondary circulation in the tropical cyclone was reproduced. In the tangential wind field supergradient winds (i.e. $v > v_{gr}$) were obtained.
The boundary layer equations for a hurricane were derived from the Navier-Stokes' equations, assuming that the turbulent transfer of momentum can be characterized by a constant eddy diffusivity in conjunction with a bulk representation of surface drag. The derivation was based on a detailed scale analysis of the Navier-Stokes' equations.

It was shown how a linear form of the boundary layer equations that has been studied by several previous authors (e.g. Kepert 2001) can be obtained as a weak friction limit of the full equations. The weak friction limit formally assumes that the radial and perturbation tangential velocity components are small compared with the gradient wind speed above the boundary layer and that the local Rossby number based on the absolute vorticity of the gradient wind is of order unity or less.
Height-radius plots of the three velocity components derived from an analytic solution of the linear boundary layer equations were shown and discussed. The calculations were similiar to those carried out by Kepert (2001) but in contrast to these a symmetric vortex was assumed. Interesting features of the solutions are the presence of supergradient winds at all radii and a vertical velocity that has a weak local maximum just at the top of the inflow layer near the radius of maximum gradient wind speed. The radial profile of vertical velocity at the top of the boundary layer for different tangential wind profiles is similar in shape to those in a slab version of the linear model.

The dependence of the solutions on different values of eddy diffusivity and drag coefficient was studied. It was shown, inter alia, that a more sophisticated representation of drag, where the drag coefficient is assumed to increase with increasing wind speed, does not change the solutions significantly.

It also followed that the linear solution is not selfconsistent over a considerable range of radii because the magnitude of the nonlinear terms calculated from this solution is not much smaller than the linear terms themselves. Therefore it is most likely not of much interest to carry out calculations with a more sophisticated parameter setup such as radially varying drag or eddy diffusivity. This conclusion is supported also by considering the relative magnitude of terms in the scale analysis. These remarks apply presumably to non-axisymmetric extensions of the linear theory also.

In chapter (3) a slab boundary layer model was examined. The model was similiar to the one presented by Smith (2003), but included some new features such as a new derivation of the initial values for the wind speeds and the mass flux of shallow convection at large radii. The development of supergradient winds in the boundary layer was found to be an ubiquitous feature. The solutions exhibit two types of behavior in the inner core of the vortex depending on the boundary layer depth and the maximum tangential wind speed above the layer. For small depths, or equivalently for large maximum tangential wind speeds, the winds are strongly supergradient and lead to a rapid

deceleration of the inflow. As a result, the inflow becomes zero at some finite radius inside the radius of maximum tangential wind speed above the boundary layer. At this radius the equations are singular. At this point and near it, boundary-layer theory is no longer applicable. The reason is, that the radial gradients of the quantities are exceeding their vertical gradients near that point. This is in contrast to the assumption of boundary-layer theory that the radial gradients have to be small compared to the vertical gradients.

At a particular depth, which may be called a bifurcation depth, there is an abrupt transition in behavior. The so-called bifurcation depth increases with the maximum tangential wind speed above the boundary layer and for depths larger than this value, the solutions remain non-singular until within a few km of the rotation axis. Inside the radius of maximum tangential wind speed above the boundary layer, the tangential wind speed in the boundary layer oscillates about that above the layer, becoming alternately supergradient and subgradient. These oscillations are accompanied by oscillations in the radial wind speed in the layer and in the vertical flow at the top of the boundary layer. The reasons for these oscillations were discussed in detail and it was argued that they may not be realistic. They were interpreted as an artifact of the prescribed radial pressure gradient at the top of the layer in regions, where there is ascent. It was shown also that the bifurcation depth increases not only with the maximum tangential wind at the top of the boundary layer, but also with a decreasing mass flux of shallow convection (the mass flux which is connected to thermally-driven turbulent mixing of the atmosphere, where vertical lifting processes are confined to low levels).

In general the downward mixing of radial momentum by shallow convection reduces the inflow. Together with the downward mixing of tangential momentum the effects of shallow convection reduce the supergradient winds found in the boundary layer. It was shown that an increase of the surface drag has the same effects on the solutions as a decrease in the boundary layer depth.

The assumption was investigated, that the mean vertical velocity at the top of the boundary layer is set to zero in the momentum equations and is simply diagnosed by use of the continuity equation. It was found that this simplification of the dynamical equations is reasonably accurate.

A scale analysis of the full equations as well as the results of the linear boundary layer model studied in chapter (2) suggested, that the prescribed boundary layer depth should not be hold constant but vary with radius. From chapter (2) it emerged that the boundary layer depth δ should vary inversely with the square root of the inertial parameter. Consequently two different radially varying profiles for the boundary layer depth δ, fulfilling this requirement, were used in the calculation with the slab model. While the results for the radial, tangential and vertical wind speeds changed significantly when a radially varying δ was used, the thermodynamic parameters were found to be much less sensitive.

The results for the thermodynamical fields were found to be very similiar to those presented by Smith (2003), although the calculations carried out in this work used an improved algorithm for the calculation of the radiative-convective equilibrium state of the boundary layer at some large radius R where the inwards integration begins. To assess the results from the slab model, the values predicted for the potential temperature were compared to the observations made in category-five hurricane "Isabel" (2003). For that comparison a strong vortex comparable to a category-five hurricane was used to initialize the model calculation. It turned out that the results of the slab model were not improper if they were compared to the ones measured in "Isabel" that were reported by Montgomery *et al.* (2006). In general the solutions for the thermodynamic quantities suggest that the heat and moisture fluxes at the top of the boundary layer are of the same magnitude as those at the sea surface under the assumption of local radiative-convective equilibrium. The calculations discussed here showed that the knowledge of the thermodynamic parameters is really a key issue and they highlighted the urgent need of representative field measurements of the fluxes at the top of the boundary layer.
The results obtained with the linear model as well as those of the slab model lead to the conclusion that there is a potential inconsistency in vortex boundary layer models that assume a prescribed tangential wind speed, or equivalently the radial pressure gradient, above the boundary layer in regions, where the the flow exits the boundary layer. This limitation applies to many previous studies of the boundary layer that are found in the literature.

It was argued that this limitation is less severe for slab models than it is for models that

allow for vertical variations of the variables as the linear model prescribed in chapter (2). Moreover the implications of the above issues for the potential intensity theory are of special interest.

In chapter (4) first Emanuel's simple steady-state hurricane model (see Emanuel 1986) was reviewed, which was the basis for his potential intensity theory, where he developed a theoretical approach to assess the question how intense a hurricane may become during its life-cycle.

Using the results from the investigations of a linear and a slab hurricane boundary layer model from chapters (2) and (3) it was possible to show in the course of chapter (4) that the tacit assumption of gradient wind balance in the boundary layer is a major deficiency of Emanuel's steady-state hurricane model. Also, by implication, his theory for the potential intensity of hurricanes must be seen in the light of the recent findings. Although the vertically-integrated tangential wind in the boundary layer is usually no more than fifteen to twenty percent less than its gradient wind counterpart, a fact that makes gradient wind balance a seemingly defensible zero-order approximation locally, it was shown that the global consequences of this simplification on the inner-core structure of intense storms are nontrivial.

Indeed, the processes observed in the boundary layer, as for example the low-level convergence, result from gradient wind imbalance that originates from a reduction of the tangential wind speed by friction. When such imbalance is allowed for by the inclusion of a nontrivial radial momentum equation in the theory, the boundary layer flow depends on the tangential wind structure above the boundary layer. This feature must be taken into account in an improved theory for hurricane potential intensity.

It is concluded that it is not permissible to make the gradient balance assumption in the inner region and that in a realistic model of a hurricane, the radial pressure gradient above the boundary layer must be prescribed or determined independently of the boundary layer. Nevertheless, even in this case, the solutions show a mismatch between the predicted mean winds in the boundary layer and those prescribed above, where the flow is out of the layer. This mismatch suggests that the outflow jet found above the inflow layer in full numerical solutions for the boundary layer together with the flow above it is a means by which the flow exiting the boundary layer adjusts to the radial pressure gradient associated with the vortex above the boundary layer. The implication would be that a more complete formulation of the (steady) boundary layer in the inner core region of a tropical cyclone using a slab-type formulation would

require at least two layers including one to represent the outflow jet. This layer is required to allow the radial and tangential wind fields to adjust to the radial pressure gradient implied by the mass distribution in the free troposphere. Such a formulation would appear to be a necessary component of a more consistent and accurate theory for hurricane potential intensity and such a theory must take into account the vortex size and the boundary layer depth.

In the course of this work a comprehensive study of the hurricane boundary layer was carried out. Although this part of the hurricane was subject to research before, substantial progress in the understanding of hurricane boundary layer models was achieved with this study. The symmetric linear model, which was developed in chapter (2), is a perfect tool to study the main dynamical processes in the storm. A scale analysis of the complete equations of motions has never been carried out before and it was the first time that an appraisal of the linear theory was performed.
The slab model was improved fundamentally for example by introducing a radially varying boundary layer depth and a new scheme to calculate the initial values. However, even if these results are already quite satisfactory, the main benefit from this work lies in the fact that two different types of models were used. It was possible for the first time to present a comprehensive study and compare the weaknesses and the strengths of the two models directly. Only this comparison allowed to spot the main deficiencies of this two common model types. The results of this work also stimulated the study about balanced boundary layers by Smith and Montgomery (2008). Finally, the question turned up if the results of this work have consequences for other fields of hurricane research. The problem that was picked up was the question about hurricane intensity, as this is one of the most actual topics in hurricane research. Consequently, the famous E(manuel) P(otential) I(ntensity) theory was reassessed in the light of the results obtained in chapters (2) and (3). Indeed, it turned out that the limitations of the representation of the boundary layer used in EPI-theory is the major deficiency of this theory. This is an actual breakthrough as before it was not possible to pin down the reasons why EPI-theory fails in certain cases. This work even could present a new conceptual model for the inner core region that does not suffer from the former limitations. Altogether the results of this work, that are partly published (see Smith and Vogl 2008, Smith, Montgomery and Vogl 2008 and Vogl and Smith 2009) contribute not only to the research in the field of the tropical cyclone boundary layer itself but will also be of

merit for an urgently needed, improved PI theory.

Appendix

Windprofiles used in hurricane boundary layer models

The different models for the hurricane boundary layer which are discussed in this work have several different features and differences in their setup. However one thing they have in common: the need of a prescribed profile for the tangential wind at the top of the boundary layer. In general it would be best to introduce a profile which is supported by measurements of the wind speed in the region which is of interest. However it turns out that on the one hand wind measurements in the hurricane boundary layer are not easy to accomplish, on the other hand can it be of advantage to have an analytic function representing the wind profile. There are many possibilities to obtain such a vortex profile which is appropriate for the extreme winds in a hurricane.

Well known are the representations developed by Holland (1980) or Willoughby *et al.* (2006). Some other profiles were developed by Smith (1968) or Smith (2003).

The wind profile from Smith (1968)

Smith (1968) represented the main vortex by a steady, axisymmetric, potential vortex which is stationary in a fluid at rest and has a tangential velocity V_{gr}. This tangential velocity is determined by the gradient wind equation:

$$V_{gr}(R) = -\frac{1}{2}Rf + \sqrt{\frac{1}{4}R^2f^2 + \frac{R}{\rho}\frac{dP}{dR}}, \tag{4.32}$$

where f is the Coriolis parameter, ρ is the density of air, R the radial distance and

$P(R)$ the pressure. This vortex is a solution to the Euler equation of motion in a rotating frame of reference in which there is no radial motion ($U = 0$). With a wind profile defined like that, the flow is completely specified by the choice of an arbitrary pressure profile $P(R)$. This is a major advantage of that method. Measurements of the pressure profiles of tropical cyclones are much easier to obtain than such of the velocity. If a radial pressure profile is given, the shape of V_{gr} directly results for physical reasons. A possible choice for the radial pressure profile which is in good agreement with measurements is

$$P(R) = P_c + (P_g - P_c) \cdot e^{x\left(b - \frac{R_m}{R}\right)}, \tag{4.33}$$

where P_c is the pressure at the center, P_g the pressure at the geostrophic radius R_g, $b := \frac{R_m}{R_g}$ is a constant and x is chosen to make the azimuthal velocity above the boundary layer a maximum at $R = R_m$. From the equation of the pressure profile Eq.(4.33) it follows

$$\frac{dP}{dR} = \frac{(P_g - P_c)R_m x}{R^2} \cdot e^{x\left(b - \frac{R_m}{R}\right)}.$$

To obtain the constant x it is of advantage to nondimensionalize Eq.(4.32). The appropriate scales are:

$$U = V_g u, \quad V = V_g v, \quad V_{gr} = V_g v_{gr}, \quad W = \frac{V_g Z_g}{R_g} w, \quad Z = Z_g z, \quad R = R_g r,$$

where the subscript "g" denotes the value of the variable at the geostrophic radius R_g and $R_0 = \frac{V_g}{R_g f}$ is a local Rossby number. The Eddy diffusivity K_M is scaled by its value K_M^* at the geostrophic radius and can be written as $K_M = K_M^* k$ where k may be a constant or a function $k(r, z)$. Now $Z_g = \sqrt{\frac{K_M^*}{f}}$.

With the scalings $V_{gr} = V_g v_{gr}$, $R = R_g r$ and $b := \frac{R_m}{R_g}$ it follows from Eq.(4.32)

$$V_g v_{gr} = -\frac{1}{2}(R_g f)r + \left[(R_g f)^2 \frac{1}{4} r^2 + \frac{(P_g - P_c)}{\rho} \cdot \frac{1}{(R_g f)^2} \cdot (R_g f)^2 \cdot \frac{R_m}{R_g} \frac{x}{r} \cdot e^{x\left(b - \frac{b}{r}\right)}\right]^{\frac{1}{2}}.$$

Now let $m := \frac{(P_g - P_c)}{\rho} \cdot \frac{1}{(R_g f)^2}$, then

$$\frac{V_g}{R_g f} \cdot v_{gr} = -\frac{1}{2} r + \left(\frac{1}{4} r^2 + \frac{mxb}{r} \cdot e^{xb\left(1 - \frac{1}{r}\right)}\right)^{\frac{1}{2}}$$

and finally with $R_0 = \frac{V_g}{R_g f}$ the equation for the nondimensional wind profile at the top of the boundary layer is of the form

$$\tilde{v} = R_0 \cdot v_{gr} = -\frac{1}{2}r + \left(\frac{1}{4}r^2 + \frac{mxb}{r} \cdot e^{xb\left(1-\frac{1}{r}\right)}\right)^{\frac{1}{2}}. \tag{4.34}$$

From the fact that $V_{gr} = V_g$ at the geostrophic radius $R = R_g$ (that is $r = 1$) it follows that $v_{gr} = 1$ at $r = 1$. Now from Eq.(4.34) an expression for the Rossby radius Ro may be obtained:

$$Ro = -\frac{1}{2} + \left[\frac{1}{4} + mxb\right]^{\frac{1}{2}}. \tag{4.35}$$

It is now possible to derive an equation for x so that finally an expression for the windprofile v_{gr} is obtained. The maximum value of $v_g r$ is reached at $R = R_m = R_g \cdot \frac{R_m}{R_g}$, which means that v_{gr} is maximal at $r = \frac{R_m}{R_g} = b$, so $\frac{dv_{gr}}{dr} = 0$ at $r = b$. It is

$$\frac{dv_{gr}}{dr} = \frac{1}{Ro}\frac{d\tilde{v}}{dr} =$$

$$= \frac{1}{Ro} \cdot \left[-\frac{1}{2} + \frac{\frac{r}{2} - \frac{mxb}{r^2} \cdot e^{xb\left(1-\frac{1}{r}\right)} + \frac{b^2mx^2}{r^3} \cdot e^{xb\left(1-\frac{1}{r}\right)}}{2\sqrt{\frac{r^2}{4} + \frac{bmx}{r} \cdot e^{xb\left(1-\frac{1}{r}\right)}}}\right].$$

So for $r = b$ it follows:

$$-\frac{1}{2} + \frac{\frac{b}{2} - e^{x(b-1)} \cdot \frac{mx}{b} + e^{x(b-1)} \cdot \frac{mx^2}{b}}{2\sqrt{\frac{1}{4}b^2 + e^{x(b-1)} \cdot mx}} = 0$$

or

$$\frac{b}{2} - e^{x(b-1)}\left(\frac{mx}{b} - \frac{mx^2}{b}\right) = \sqrt{\left(\frac{1}{2}b\right)^2 + e^{x(b-1)} \cdot mx}.$$

Squaring the left and the right hand-side of the equation finally yields an equation for x

$$b^2(x-2) + mx(x-1)^2 \cdot e^{x(b-1)} = 0. \tag{4.36}$$

For a vortex of hurricane strength it is realistic to choose the constants $P_c = 940$ mb, $P_g = 1000$ mb, $R_g = 1000$ km, $R_m = 40$ km, $f = 5 \cdot 10^{-5}$ and $\rho = 0.0012\mathrm{g\,cm^{-3}}$. The obtained pressure profile is shown in Fig.(4.8).

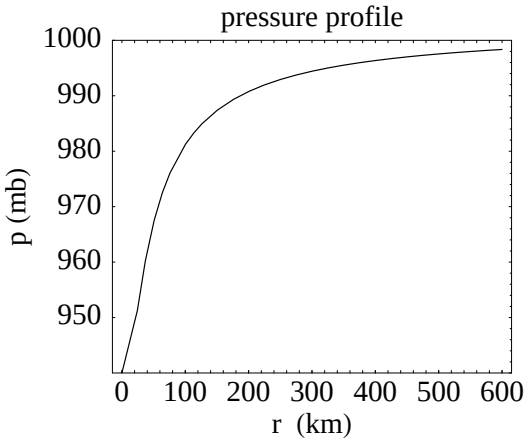

Figure 4.8: Pressure profile $P(R)$ obtained from Eq.(4.33).

It shows a steep increase from its value of 940 hPa at $r = 0$ to about 990 hPa at 200 km. Then an asymptotical increase towards 1000 hPa in the region far out from the core is found. This kind of radial profile is typical for the boundarylayer of a tropical cyclone where there is a strong low in the center of the storm found.

Finally a typical profile for the tangential wind at the top of the hurricane boundary layer can be calculated. The resulting vortex is shown in Fig.(4.9).

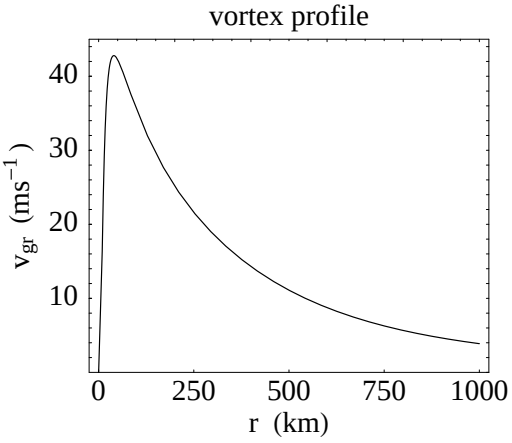

Figure 4.9: Profile for the tangential wind speed v_{gr} at the top of the boundary layer.

The profile shows all characteristics of the tangential wind speed in a hurricane. For regions far from the storm center the tangential wind speed is close to zero which means that there is almost no rotation. Towards the center the tangential wind speed is increasing rapidly. This means that the air parcels are spinning much faster when

they approach the eye wall. The maximum wind speed is attained at a radius of $R_m = 40$ km as it was constructed. The maximum tangential wind speed v_m is 42.78 $\mathrm{m\,s^{-1}}$. This reproduces the fact that the highest wind speeds in the hurricane are usually measured in the clouds of the eyewall. For radii smaller than R_m the wind speed is dropping down until it reaches the zero value right in the storm center as it does in a real storm. Thus it is to say that a sufficiently reasonable pressure profile ensures the resulting wind profile to be close to reality. If

$$\zeta_{a_{gr}} = \frac{\partial v_{gr}(r)}{\partial r} + \frac{v_{gr}(r)}{r} + f$$

is the absolute vorticity and ξ_{gr} is defined as

$$\xi_{gr} = \frac{2v_{gr}(r)}{r} + f,$$

then a parameter for the inertial stability of the profile may be introduced which is $c = \zeta_a \xi$. The profile is inertially stable if $c > 0$.

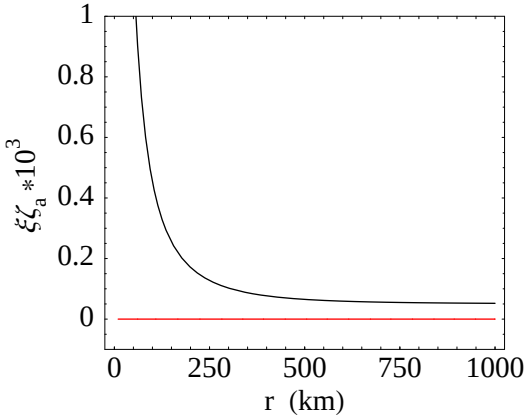

Figure 4.10: Parameter for the inertial stability $c = \xi_{gr}\zeta_{a_{gr}}$; the zero value is marked by the horizontal red line.

Figure (4.10) shows the inertial stability parameter c and the horizontal red line marks the value $c = 0$. Clearly it follows from Fig.(4.10) that the profile is inertially stable as $c > 0$ for all radii.

Moreover it is indicated by a scale analysis that the depth of the boundary layer is decreasing with increasing wind speeds. A boundary layer scale depth

$$\delta = \sqrt{\frac{2K_M}{\sqrt{\zeta_{a_{gr}}\xi_{gr}}}}$$

was introduced in Chapter (2) which shows the variation of the boundary layer depth with varying wind speed. If K_M=10 m^2 s^{-1} and the Coriolis parameter is $f = 5 \times 10^{-5}$ the boundary layer depth scale may be plotted for the vortex profile shown in Fig.(4.9).

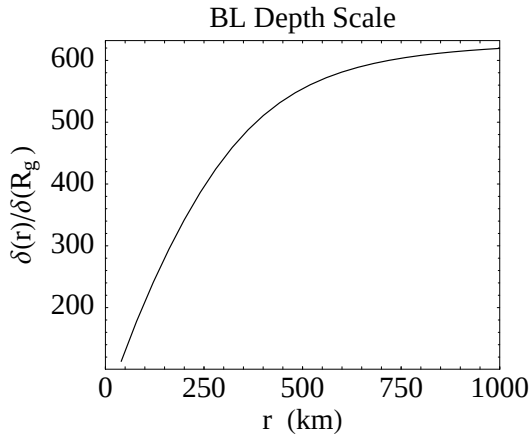

Figure 4.11: Boundary layer depth scale $\delta(r)$ evaluated with the vortex profile shown in Fig.(4.9).

Figure (4.11) shows the boundary layer depth scale δ. The depth scale δ is decreasing towards the center of the storm.

The wind profiles from Smith (2003)

In the calculations carried out by Smith (2003) and in this work a set of profiles was examined for the gradient wind which were of the form

$$V(r) = V_1 s e^{-\alpha_1 s} + V_2 s e^{-\alpha_2 s}, \quad \text{where} \quad s = \frac{r}{r_m},$$

and V_1, V_2, α_1 and α_2 are constants. This constants were chosen so that the maximum wind speed V_m is 40 m s^{-1} and occurs at a radius of r_m = 40 km. In terms of the parameters $\mu = V_2/v_m$ and α_2 it is possible to calculate α_1 and V_1 using:

$$\alpha_1 = (1 - \mu\alpha_2 e^{-\alpha_2})/(1 - \mu e^{-\alpha_2}), \tag{4.37}$$

$$V_1 = v_m e^{\alpha_1}(1 - \mu e^{-\alpha_2}). \tag{4.38}$$

Five different wind profiles are investigated which were specified by the values for (μ, α): (0.9,0.5), (0.8,0.4), (0.5,0.3), (0.5,0.25) and (0.3,0.15). These profiles are shown in Fig.(4.12), panel (a).

All these profiles are inertially stable ($\xi_{gr}\zeta_{a_{gr}} > 0$) for the values of the Coriolis parameter used: $f = 5.0 \times 10^{-5}$ s^{-1}.

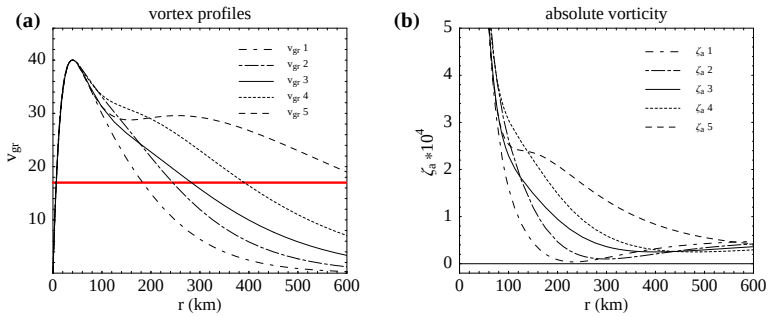

Figure 4.12: Tangential wind profiles as a function of radius (the red line marks the radius of gale force winds), panel (a) and the absolute vorticity for each of the vortex profiles, panel (b).

Panel (b) of Fig.(4.12) shows the absolute vorticity of the five different vortex profiles. A typical vortex profile which is in the middle of the range of the shown functions of v_{gr} is vortex 3, which was calculated with the parameters $(\mu, \alpha) = (0.5, 0.3)$. This profile is used for the control calculations for all the models which were investigated in this work.

A comparison of vortex 3 with the profile from Smith (1968) shows, that the kind of ansatz described above leeds to very similiar results than a physical derivation of a possible profile, starting from a given pressure profile. Figure (4.13) shows tangential wind profiles vortex 3 (black) and the one calculated from Smith (1968) (red) in panel (a). The corrsponding boundary layer depth scale δ for these two profiles is shown in panel (b).

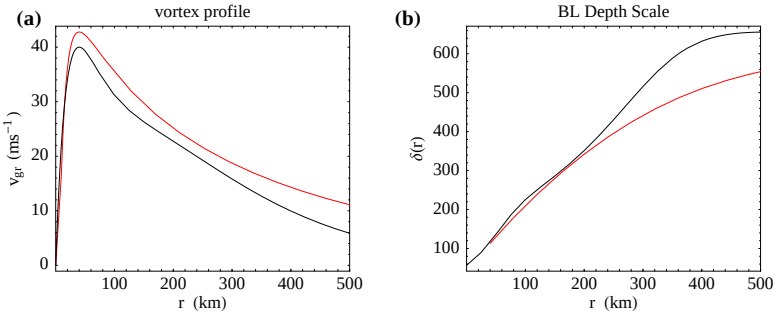

Figure 4.13: Tangential wind profiles vortex 3 (black) and from Smith (1968) (red), panel (a) and the boundary layer depth scale δ for these two profiles, panel (b).

It is seen that the profile from Smith (1968) is in general lying slightly higher than vortex 3. This may be easily modified by changing the given pressure profile or the given value for the wind maximum v_m. The general characteristic shape of the profile is the same for both cases.

Another possibility to specify wind profiles in a simple way but with physical background is the one described by Nolan (2005). The radial variation of his wind field is defined by:

$$V(r) = \frac{(1+a)V_{max}\left(\frac{r}{r_{max}}\right)}{a + \left(\frac{r}{r_{max}}\right)^{(1+a)}}, \tag{4.39}$$

where V_{max} defines the maximum azimuthal wind speed, r_{max} is the radius of the maximum wind, and a is parameter which may be varied to modify the shape of the profile.
Eq.(4.39) defines a wind profile that decays as $\frac{1}{r^a}$ in the far field and, as for the profile from Smith (2003), both the maximum V_{max} and the radius where it occurs, r_{max}, may easily be specified. Another advantage is that there are measurements available for the decay rate. Observations (Shea and Gray 1973, Samsury and Zipser 1995, Mallen *et al.* 2005) show that for tropical cyclones, the parameter a varies between values of $\frac{1}{3}$ and $\frac{2}{3}$.

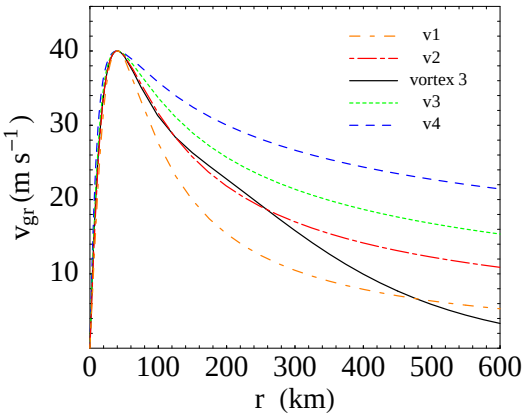

Figure 4.14: Tangential wind profiles vortex 3 (black) and four profiles calculated with Eq.(4.39) labelled $v1$-$v4$.

Figure (4.14) shows four profiles calculated with Eq.(4.39) labelled $v1$-$v4$ and for com-

parison the profile vortex 3 as described above. To calculate $v1$-$v4$ the maximum V_{max} was set to 40 $\mathrm{m\,s^{-1}}$ at $r_{max} = 40$ km. The parameters a_1 - a_2 were chosen to be 1/3, 1/2, 2/3 and 1. It is seen that the profiles have a wide range of values. The profile vortex 3 coincides best with $v2$. For radii smaller than 300 km the two profiles are almost identical. For large radii vortex 3 decays much faster than $v2$. However, the values of vortex 3 are still in the range of the results obtained with Eq.(4.39).

Bibliography

[1] Aberson, S. D., Montgomery, M. T., Bell M. M. and M. L. Black 2006: Hurricane Isabel (2003): New insights into the physics of intense storms. Part II - Extreme localized wind. *Bull. Amer. Meteorol. Soc.,* **87,** 1349-1357

[2] Anthes, A. R. 1982: Tropical Cyclones: Their Evolution, Structure and Effects. *American Meteorological Society*, Boston

[3] Bister, M. and K. A. Emanuel 1998: Dissipative heating and hurricane intensity. *Meteor. Atmos. Phys.*, **65,** 233-240

[4] Bell, M. M. and M. T. Montgomery 2008: Observed Structure, Evolution, and Potential Intensity of Category 5 Hurricane Isabel (2003) from 12 to 14 September. *Mon. Wea. Rev.,* **136,** 2023-2046

[5] Bengtsson, L., Hodges, K. I., Esch, M., Keenlyside, N., Komblush, L., Luo, J. J. and T. Yamagata 2007: How may tropical cyclones change in a warmer climate. *Tellus*, **59A,** 539-561

[6] Black, P. G. and G. J. Holland 1995: The Boundary Layer of tropical cyclone Kerry (1979). *Mon. Wea. Rev.*, **123**, 2007-2028

[7] Black, P. G., D'Asaro, E. A., Drennan, W. M., French, J. R., Niiler, P. P., Sanford, T. B., Terrill, E. J., Walsh, E. J. and J. A. Zhang 2006: Air-sea exchange in hurricanes: Synthesis of observations from the coupled boundary layer air-sea transfer experiment. *Bull. Amer. Meteor. Soc.*, **88**, 357-374

[8] Blake, E. S., Rappaport, E. N. and C. W. Landsea 2007: The Deadliest, Costliest, and Most Intense United States Tropical Cyclones from 1851 to 2006 (and other

frequently requested hurricane facts). *NOAA Technical Memorandum,* **NWS TPC-5,**

[9] Bode, L. and R. K. Smith 1975: A parameterization of the boundary layer of a tropical cyclone. *Bound. Layer Met.*, **8**, 3-19

[10] Braun, S. A., Montgomery, M. T. and A. Pu 2006: High-resolution simulation of Hurricane Bonnie (1998). Part I: The organization of eyewall vertical motion. *J. Atmos. Sci., NASA/CAMEX special issue*, **63,** 19-42

[11] Camp, J. P., and M. T. Montgomery 2001: Hurricane maximum intensity: past and present. *Mon. Wea. Rev.*, **129,** 1704-1717

[12] Carrier G. F. 1971: Swirling flow boundary layers. *J. Fluid Mech.*, **49**, 133-144

[13] Cram, T. A., Persing, J,. Montgomery, M. T. and S. A. Braun 2007: A Lagrangian trajectory view on transport and mixing processes between the eye, eyewall, and environment using a high resolution simulation of Hurricane Bonnie (1998). *J. Atmos. Sci.*, **64,** 1835-1856

[14] Ekman, V. W. 1905: On the the influence of the Earth's rotation on ocean currents. *Arkiv.Mat. Astron. Fysik.*, **2**, (11), 1-53

[15] Eliassen, A. 1971: On the Ekman layer in a circular vortex. *J. Meteor. Soc. Japan*, **49**, (special issue), 784-789

[16] Eliassen, A. and M. Lystadt 1977: The Ekman layer of a circular vortex: A numerical and theoretical study. *Geophysica Norvegica*, **31,** 1-16

[17] Emanuel, K. A. 1986: An air-sea interaction theory for tropical cyclones. Part I: Steady-state maintenance. *J. Atmos. Sci.*, **43,** 585-604

[18] Emanuel, K. A. 1988: The maximum intensity of hurricanes. *J. Atmos. Sci.*, **45,** 1143-1155

[19] Emanuel, K. A. 1989: The finite-amplitude nature of tropical cyclogenesis. *J. Atmos. Sci.*, **46,** 3431-3456

[20] Emanuel, K. A. 1995a: The behaviour of a simple hurricane model using a convective scheme based on subcloud-layer entropy equilibrium. *J. Atmos. Sci.*, **52,** 3960-3968

[21] Emanuel, K. A. 1995b: Sensitivity of tropical cyclones to surface exchange coefficients and a revised steady state model incorporating eye dynamics. *J. Atmos. Sci.*, **52,** 3969-3976

[22] Emanuel, K. A. 1997: Some aspects of hurricane inner-core dynamics and energetics. *J. Atmos. Sci.*, **54,** 1014-1026

[23] Emanuel, K. A. 2005a: Increasing destructiveness of tropical cyclones over the past 30 years. *Nature*, **436,** 686-688

[24] Emanuel, K. A. 2005b: Divine Wind: The History and Science of Hurricanes. *Oxford University Press*, New York

[25] Etling, D. 2002: Theoretische Meteorologie - Eine Einführung (2. Aufl.). *Springer-Verlag*, Berlin

[26] Frank, W. M. and E. A. Ritchie 1999: Effects of vertical wind shear on the intensity and structure of numerically simulated hurricanes. *Mon. Wea. Rev.*, **129**, 2249-2269

[27] Franklin, J. L., Black, M. L. and K. Valde 2003: GPS dropwinsonde wind profiles in hurricanes and their operational implications. *Weather Forecast*, **18**, 32-44

[28] Gall, R., Tuttle, J. and P. Hildebrand 1998: Small-scale spiral bands observed in hurricanes Andrew, Hugo, and Erin. *Mon. Weather Rev.*, **126**, 1749-1766

[29] Garratt, J. R. 1977: Review of drag coefficients over oceans and continents. *Mon. Wea. Rev.*, **105**, 915-929

[30] Garratt, J. R. 1992: The atmospheric boundary layer. *Cambridge University Press*, Cambridge

[31] Holton, J. R. 2004: An Introduction to Dynamic Meteorology (4th Ed.). *Academic Press*, London

[32] Houze, R. A., Chen, S. S., Smull, B. F., Lee, W. C. and M. M. Bell 2007: Hurricane intensity and eyewall replacement. *Science,* **315**, 1235-1239

[33] Kepert, J. D. 2001: The dynamics of boundary layer jets within the tropical cyclone core. Part I: Linear Theory. *J. Atmos. Sci.*, **58,** 2469-2484

[34] Kepert, J. D. and Y. Wang 2001: The dynamics of boundary layer jets within the tropical cyclone core. Part II: Nonlinear enhancement. *J. Atmos. Sci.*, **58,** 2485-2501

[35] Knutson, T. K. and R. E. Tuleya 2004: Impact of CO2-induced warming on simulated hurricane intensity and precipitation: Sensitivity to the choice of climate model and convective parameterization. *J. Clim.*, **17,** 3477-3495

[36] Leslie, L. M. and R. K. Smith 1970: The surface boundary layer of a hurricane - Part II. *Tellus*, **22,** 288-297

[37] Lilly, D. K. 1966: On the instability of Ekman boundary layer flow. *J. Atmos. Sci.*, **23**, 481-494

[38] Mallen, K. J., Montgomery, M. T. and B. Wang 2005: Re-examining tropical cyclone near-core radial structure using aircraft observations: implications for vortex resiliency. *J. Atmos. Sci.*, **62**, 408-425

[39] Marks, F. D., Jr., Houze, R. A. Jr., and J. F. Gamache 1992: Dualaircraft investigation of the inner core of Hurricane Norbert. Part I: Kinematic structure. *J. Atmos. Sci.*, **49**, 919-942

[40] Marks, F. D., Black, P. G., Montgomery, M. T. and R. W. Burpee 2008: Structure of the Eye and Eyewall of Hurricane Hugo (1989). *Mon. Wea. Rev.*, in press.

[41] Montgomery, M. T., Snell, H. D. and Z. Yang 2001: Axisymmetric spindown dynamics of hurricane-like vortices. *J. Atmos. Sci.*, **58,** 421-435

[42] Montgomery, M. T., Vladimirov, V. A. and P. V. Denissenko 2002: An experimental study on hurricane mesovortices. *J. Fluid Mech.,* **471,** 1-32

[43] Montgomery, M. T., Bell, M. M., Aberson, S. D. and M. L. Black 2006: Hurricane Isabel (2003): New insights into the physics of intense storms. Part I Mean vortex structure and maximum intensity estimates. *Bull. Amer. Meteor. Soc.*, **87,** 1335-1347

[44] Nguyen, S. V., Smith, R. K. and M. T. Montgomery 2008: Tropical-cyclone intensification and predictability in three dimensions. *Quart. J. Roy. Meteor. Soc.*, **134**, in press.

[45] Nolan, D. S. 2005: Instabilities in hurricane-like boundary layers. *Dyn. Atmos. Oceans*, **40**, 209-236

[46] Ooyama, K. V. 1969: Numerical simulation of the life cycle of tropical cyclones. *J. Atmos. Sci.*, **26**, 3-40

[47] Ooyama, K. V. 1982: Conceptual evolution of the theory and modeling of the tropical cyclone. *J. Meteor. Soc. Japan*, **60**, 369-380

[48] Pedlosky, J. 1987: Geophysical Fluid Dynamics (2nd Ed.). *Springer-Verlag* , New York

[49] Persing, J. and M. T. Montgomery 2003: Hurricane superintensity. *J. Atmos. Sci.*, **60**, 2349-2371

[50] Pielke, R. A. J., and C. W. Landsea 1998: Normalized U.S. Hurricane damage, 1925-1995. *Weath. Forecast.*, **13**, 621-631

[51] Powell, M. D., Vickery, P. J. and T. A. Reinhold 2003: Reduced drag coefficient for high wind speed in tropical cyclones. *Science* **422**, 279-283

[52] Rappaport, E. N. and J.Fernandez-Partagas 1995: The Deadliest Atlantic Tropical Cyclones, 1492-1996. *NOAA Technical Memorandum,* **NWS NHC 47,** updated 1997 by J. Beven

[53] Rosenthal, S. L. 1962: A theoretical analysis of the field motion in the hurricane boundary layer. *National Hurricane Research Project Report No 56*, US Dept of Commerce, 12pp

[54] Rotunno, R. and K. A. Emanuel 1987: An air-sea interaction theory for tropical cyclones. Part II: Evolutionary study using a nonhydrostatic axisymmetric numerical model. *J. Atmos. Sci.*, **44**, 542-561

[55] Samsury, C. E. and E. J. Zipser 1995: Secondary wind maxima in hurricanes: airflow and relationship to rainbands. *Mon. Wea. Rev.* **123**, 3502-3517

[56] Schubert, W. H., Montgomery, M. T., Taft, R. T., Guinn, T. A., Fulton, S. R., Kossin, J. P. and J. P. Edwards 1999: Polygonal eyewalls, asymmetric eye contraction and potential vorticity mixing in hurricanes. *J. Atmos. Sci.*, **56,** 1197-1223

[57] Shapiro, L. J. 1983: The asymmetric boundary layer under a translating hurricane. *J. Atmos. Sci.*, **40**, 1984-1998

[58] Shapiro, L. J. and H. Willoughby 1982: The response of balanced hurricanes to local sources of heat and momentum. *J. Atmos. Sci.*, **39**, 378-394

[59] Shea, D. J. and W. M. Gray 1973. The hurricane's inner core region. Part I: Symmetric and asymmetric structure. *J. Atmos. Sci.* **30**, 1544-1564

[60] Smith, R. K. 1968: The surface boundary layer of a hurricane. *Tellus*, **20**, 473-483

[61] Smith, R. K. 2000: The role of cumulus convection in hurricanes and its representation in hurricane models. *Rev. Geophys.*, **38**, 465-489

[62] Smith, R. K. 2003: A simple model of the hurricane boundary layer. *Quart. J. Roy. Meteor. Soc.*, **129**, 1007-1027

[63] Smith, R. K., Montgomery, M. T. and H. Zhu 2005: Buoyancy in tropical cyclones and other rapidly rotating vortices. *Dyn. Atmos. Oceans,* **40**, 189-208

[64] Smith, R. K. 2006: Accurate determination of a balanced axisymmetric vortex in a compressible atmosphere. *Tellus*, **58A**, 98-103

[65] Smith, R. K. 2007: Corrigendum and addendum: A balanced axisymmetric vortex in a compressible atmosphere. *Tellus*, **59A**, in press

[66] Smith, R. K., Montgomery, M. T. and S. Vogl 2008: A critique of Emanuel's hurricane model and potential intensity theory. *Quart. J. Roy. Meteor. Soc.,* **134**, 551-561

[67] Smith, R. K. and M. T. Montgomery 2008: Balanced boundary layers used in hurricane models. *Quart. J. Roy. Meteor. Soc.*, **134**, 1385-1395

[68] Smith, R. K. and S. Vogl 2008: A simple model of the hurricane boundary layer revisited. *Quart. J. Roy. Meteor. Soc.*, **134**, 337-351

[69] Smith, R. K., Montgomery, M. T. and S. V. Nguyen 2008: Axisymmetric dynamics of tropical-cyclone intensification in a three-dimensional model. *Quart. J. Roy. Meteor. Soc.,* submitted

[70] Smith, R. K. and M. T. Montgomery 2009: The fundamental role of buoyancy in tropical-cyclone intensification. *Quart. J. Roy. Meteor. Soc.,* submitted

[71] Stull, R. B. 1988: An Introduction to Boundary Layer Meteorology. *Kluwer Academic Publishers*, Dordrecht

[72] Taylor, G. I. 1916: Skin friction of the wind on the earth's surface. *Proc. Roy. Soc. A.*, XCII, 196

[73] Terwey, W. D. and M. T. Montgomery 2008: Secondary eyewall formation in two idealized, full-physics modeled hurricanes. *J. Geophys. Res.*, **113**, D12112

[74] Vogl S. and R. K. Smith 2009: Limitations of a linear model for the hurricane boundary layer. *Quart. J. Roy. Meteor. Soc.*, in press

Acknowledgements

This work was partially funded by a doctoral stipendium of the Munich Reinsurance Group, for which I am very grateful.